TRANSFER OF SNOW INFORMATION ACROSS THE MACRO-TO-HILLSLOPE-

SCALE GAP USING A PHYSIOGRAPHIC DOWNSCALING APPROACH:

IMPLICATIONS FOR HYDROLOGIC MODELING IN SEMIARID, SEASONALLY

SNOW-DOMINATED WATERSHEDS

by

Reggie D. Walters

A thesis

submitted in partial fulfillment

of the requirements for the degree of

Master of Science in Hydrologic Sciences

Boise State University

May 2013

BOISE STATE UNIVERSITY GRADUATE COLLEGE

DEFENSE COMMITTEE AND FINAL READING APPROVALS

of the thesis submitted by

Reggie D. Walters

Thesis Title: Transfer of Snow Information across the Macro-to-Hillslope-Scale Gap Using a Physiographic Downscaling Approach: Implications for Hydrologic Modeling in Semiarid, Seasonally Snow-Dominated Watersheds

Date of Final Oral Examination: 6 March 2013

The following individuals read and discussed the thesis submitted by student Reggie Walters, and they evaluated his presentation and response to questions during the final oral examination. They found that the student passed the final oral examination.

Alejandro N. Flores, Ph.D.   Chair, Supervisory Committee

James P. McNamara, Ph.D.   Member, Supervisory Committee

Hans-Peter Marshall, Ph.D.   Member, Supervisory Committee

The final reading approval of the thesis was granted by Alejandro N. Flores, Ph.D., Chair of the Supervisory Committee. The thesis was approved for the Graduate College by John R. Pelton, Ph.D., Dean of the Graduate College.

DEDICATION

This thesis is dedicated to my parents, Clint and Renita Walters, for teaching me diligence and for always encouraging me to pursue an education. I certainly would not be where I am today without their love and support.

ACKNOWLEDGEMENTS

ABSTRACT

Snow and ice are substantial components of the global energy balance and

hydrologic cycle. Seasonal snow covers an area of 47 million km^2 at its average

maximum extent, 98% of which occurs across the Northern Hemisphere. The earth's

radiation budget is largely controlled by the fraction of absorbed solar energy, a

parameter that is dependent upon snow surface albedo. Mountain snowpacks act as

natural reservoirs, storing large quantities of water throughout the winter until eventual

release during the melting phase. Accurate characterization of snow-covered area (SCA)

and snow water equivalent (SWE) in such terrain could substantially improve the

estimation of timing and volume of melt water runoff. However, knowledge of these

hydrologic states is limited in part by scarcely populated *in situ* observation networks and

logistical constraints in field survey sampling. Thus, satellite remote sensing observations

are often employed in conjunction with simulation models to improve the estimation of

snowpack states and resultant fluxes. This study attempts to merge complementary

datasets in order to predict spatially variable snow processes at high resolution in basins

exhibiting complex terrain. Specifically, the goal is to provide a means to downscale

existing remote sensing and snow modeling datasets using computationally efficient

methods that utilize physiographic information regarding terrain and land cover.

A linear combination model is proposed for downscaling fractional SCA from the

Moderate Resolution Imaging Spectroradiometer (MODIS) instrument from its native

resolution (500 m) to a hillslope-scale resolution (e.g., 10-30 m), preserving the predicted

snow cover fraction at the basin scale. The model is calibrated to 30 m Landsat

observations using elevation and incoming solar radiation indices for a study area in

southwestern Idaho. Validation is performed with data not used during calibration.

Results depict favorable model performance when comparing downscaled MODIS snow

cover to Landsat binary observations. An "ideal" validation test is performed in which

Landsat aggregate 500 m snow fraction informs the model with similarly positive results.

The use of such an algorithm might benefit applications from flood forecasting to SWE

reconstruction.

In a snowmelt modeling application, the satellite-derived snow cover downscaling

algorithm is applied as a binary mask to constrain spatial melt runoff data from the

SNOw Data Assimilation System (SNODAS). Differential solar radiation, forest canopy,

and snow albedo estimates are also used to further downscale the modeled melt.

Comparison with available field lysimeter data show proper spatial disaggregation of

modeled melt onto opposing hillslopes, though timing and magnitude issues exist.

Implications for resolving snowmelt at hillslope scales are briefly discussed.

TABLE OF CONTENTS

LIST OF TABLES

LIST OF FIGURES

LIST OF ABBREVIATIONS

DCEW	Dry Creek Experimental Watershed
ETM+	Enhanced Thematic Mapper (Landsat)
f_{SCA}	Fractional Snow-Covered Area
HDF	Hierarchical Data Format
LAI	Leaf Area Index
LDP	Lower Deer Point
LP-DAAC	Land Processes Distributed Active Archive Center
MODIS	Moderate-Resolution Imaging Spectroradiometer
MODSCAG	MODIS Snow-Covered Area and Grain size
MRLC	Multi-Resolution Land Characteristics Consortium
MRT	MODIS Reprojection Tool
NaN	Not a Number
NASA	National Aeronautics and Space Administration
NDSI	Normalized Difference Snow Index
NetCDF	Network Common Data Form
NLCD	National Land Cover Dataset

NOHRSC	National Operational Hydrologic Remote Sensing Center
NRCS	National Resources Conservation Service
NSIDC	National Snow and Ice Data Center
NSM	NOHRSC Snow Model
NWP	Numerical Weather Prediction
NWS	National Weather Service
RAP	Rapid Refresh
RCEW	Reynolds Creek Experimental Watershed
RUC	Rapid Update Cycle
SCA	Snow-Covered Area
SNODAS	SNOw Data Assimilation System
SNOTEL	Snowpack Telemetry
SWE	Snow Water Equivalent
TL	Treeline
TM	Thematic Mapper (Landsat)

CHAPTER ONE: PROJECT MOTIVATION AND OVERVIEW

Snow and ice are substantial components of the global energy balance and hydrologic cycle. Globally, snow covers an area of 47 million km^2 at its average maximum extent, 98% of which occurs across the Northern Hemisphere (Armstrong and Brun, 2008). The earth's radiation budget is largely controlled by the fraction of absorbed solar energy, a parameter that is dependent upon the surface albedo of snow (Stroeve et al., 2006). Hydrologically, melt from glaciers and seasonally snow-covered regions is of critical importance, delivering water to more than one-sixth of the world's population (Barnett et al., 2005). In the western United States, high-elevation snowpacks act as natural reservoirs, storing water in the mountains for later release when spring melt begins (Pavelsky et al., 2012). This snowmelt delivers an estimated 75% of annual runoff to streams and rivers in this region (Palmer, 1988). Warming trends in many western US regions have led to an earlier onset of snowmelt and stream runoff, presumably due to anthropogenic increases in atmospheric greenhouse gases (Cayan et al., 2001; Barnett et al., 2008). Moreover, climatic changes have brought about a gradual breakdown in the relevance of statistical relationships that have historically been used to forecast catchment response and water supply (Milly et al., 2008). Therefore, it is becoming increasingly essential to accurately estimate the explicit spatial and temporal distribution of snow water equivalent (SWE) and snow-covered area (SCA) in order to make sound hydrologic predictions. However, the ability to predict these variable snow states is limited in part by scarcely populated *in situ* observation networks (Martinec and Rango,

1981; Bales et al., 2006) and logistical constraints in field survey sampling (Elder et al., 1991). Thus, satellite remote sensing observations are often employed in conjunction with simulation models to improve the estimation of snowpack states and resultant fluxes.

This study addresses a notion that existing, publically-available datasets can be merged in order to predict spatially variable processes of snowmelt at increased resolution in areas of complex terrain. Specifically, the goal is to provide a means to downscale modeled and remotely-sensed snow data using simple, computationally efficient methods that utilize physiographic information regarding terrain and land cover.

In Chapter 2, a method is proposed for downscaling 500 m fractional SCA from the Moderate Resolution Imaging Spectroradiometer (MODIS) instrument. An algorithm is used by which the MODIS snow fraction informs a linear model to generate binary snow cover estimates of increased spatial resolution. The model is calibrated to Landsat observations for a semi-arid, mid-latitude region in southwestern Idaho using two indices that are presumed to strongly influence the spatial distribution of snow cover: 1) elevation and 2) incoming solar radiation. The model is tested against data not used in calibration and shown to perform favorably in some areas while failing in others. Difficulties exist in identifying specific reasons for failure, though it is suspected that forest canopy and wind re-distribution play a crucial role in snow cover, variables not implemented in this model. It is suggested that the addition of canopy and wind parameters would possibly be a way forward.

Chapter 3 proposes a method seeking to downscale Snow Data Assimilation System (SNODAS) snowmelt output from 1-km to hillslope (e.g., 10-30 m) scales. This

method makes use of the snow cover downscaling framework outlined in Chapter 2 as a binary mask, updating the coarse snowmelt data with higher resolution, spatially explicit snowmelt estimates. Additional variables used to further disaggregate the modeled melt include: 1) differential incoming solar radiation, 2) snow surface albedo, and 3) forest canopy fraction. Timing of solar radiation is used to downscale the temporal pattern of snowmelt at the pixel scale under a sinusoidal framework. Albedo is prescribed according to a simple time-decay function that uses time since snowfall as its input. An ensemble method is explored, generating a range of possible modeled albedos and constraining them to satellite-observed albedo estimates. Forest canopy fraction is used simply to attenuate solar radiation with a variation of Beer's Law. No adjustments for long-wave radiation are assumed. The model is compared with paired snowmelt lysimeters ($n = 4$) on opposing hillslopes in Dry Creek Experimental Watershed (DCEW) in southwestern Idaho, the same domain in which the calibration methodology is performed for Chapter 2. Results depict relatively successful disaggregation of SNODAS melt for differential hillslopes. However, temporal and magnitude differences in the initial model's pulses of snowmelt limit the ability of the downscaling procedure to come to notable agreement with the observations. Overall, the downscaled melt estimates, and the original estimates, tend to underestimate the magnitude of melt observed at the lysimeters.

Chapter 4 concludes the document, providing a synopsis of the work described in the document. Implications of the proposed methods for use in hydrologic modeling are briefly discussed.

CHAPTER TWO: A PHYSIOGRAPHIC APPROACH TO DOWNSCALING

FRACTIONAL SNOW COVER DATA IN MOUNTAINOUS REGIONS

2.1   Introduction

2.1.1   Background

Accurate characterization of snow-covered area (SCA) and snow water equivalent

(SWE) in complex terrain could substantially improve estimation of streamflow timing

and volume. Since more than one-sixth of the world's population depends on glacial and

seasonal snowmelt for water resource supply (Barnett et al., 2005), predicting the

spatiotemporal evolution of snow processes is of great importance for conveying reliable

hydrologic information to those who demand it. Accumulation and melting of snow occur

variably, producing heterogeneity in snowpack disappearance, which must be modeled

with accuracy in order to estimate melt runoff for a catchment (Clark et al., 2011).

However, the ability to predict these variable snow processes is limited in part by

scarcely populated *in situ* observation networks (Martinec and Rango, 1981; Bales et al.,

2006) and logistical constraints in field survey sampling (Elder et al., 1991). Thus,

satellite remote sensing observations are often employed in conjunction with simulation

models to improve the estimation of snowpack states and resultant fluxes. For example,

studies assimilating satellite-derived areal snow cover information into hydrologic

models have demonstrated improvements to simulated streamflow and SWE (Rodell and

Houser, 2004; Clark et al., 2005; Thirel et al., 2011). In other studies, snowmelt depletion

curves have been accurately constructed using similar SCA information in combination

with energy balance melt modeling (Homan et al., 2011). Retrospective analysis of SCA

data combined with distributed temperature-index and energy balance snowmelt

modeling has also been used to reconstruct basin-wide SWE at the time of maximum

accumulation, comparing favorably with results of intensive field campaigns (Martinec

and Rango, 1981; Cline et al., 1998; Durand et al., 2008; Molotch, 2009).

The space-borne Landsat remote sensing system is capable of retrieving areal

snow cover data for hydrologic studies at the catchment scale (Dozier and Marks, 1987;

Dozier, 1989; Rosenthal and Dozier, 1996). Similarly, the Moderate Resolution Imaging

Spectroradiometer (MODIS) instrument, aboard NASA Aqua and Terra satellites, can be

used to map SCA (Hall et al., 1995; Justice et al., 1998; Painter et al., 2009; Salomonson

and Appel, 2004, 2006). These products are highly valuable for their utility in updating

and constraining distributed snow models (e.g., Luce et al., 1998, 1999; Clark et al.,

2005; Thirel et al., 2011). However, each of these snow cover products has spatial or

temporal limitations. For instance, Landsat has an ideal (i.e., cloud-free) return interval of

16 days with a spatial resolution of 30 m. Conversely, estimates from MODIS can be

derived daily at a 500 m spatial resolution. Fractional snow cover products derived from

MODIS (Hall et al., 2006; Salomonson and Appel, 2004, 2006) provide a sub-grid

approximation by estimating the percentage of each pixel that is snow-covered, but do

not explicitly resolve SCA at sub-pixel scales. Since snow cover varies within these

spatiotemporal boundaries, it is desirable in many applications to have higher spatial *and*

temporal resolution.

2.1.2 Objective

The objective of this work is to develop and describe an efficient model to downscale melt-season fractional snow-covered area (f_{SCA}) data from MODIS (spatial resolution 500 m) to a higher resolution (spatial resolution 30 m), yielding a spatially explicit binary snow cover grid. The derived high-resolution snow cover product is meant to be used to constrain snow cover in future simulation modeling. The proposed model is based on the hypothesis that the distribution of SWE and snow-covered areas in a partially snow-covered region is non-random and can be predicted using terrain physiographic features like elevation, slope, and aspect (or combinations thereof). Further, it relies on the notion that snow distribution patterns tend to occur in similar patterns from year to year (Sturm and Wagner, 2010). The developed algorithm is based on physiographic characteristics that can be derived from ancillary data products, principally digital elevation models (DEMs). The algorithm assigns binary snow cover to a grid that is coincident with a 30 m DEM that is used to derive normalized potential incoming solar radiation (insolation) and normalized relief within each 500 m MODIS pixel. The method preserves the predicted snow cover fraction at the 500 m scale. We calibrate and test the model against a number of available Landsat images for a region in southwestern Idaho.

2.1.3 Relevant Theory and Outline

A melting snowpack can be conceptualized as the net effect of energy input and output to the system. The rate of internal energy change, $\frac{dU}{dt}$, within the system is typically modeled as the sum of all energy terms in the overall balancing equation

$$\frac{dU}{dt} = Q_{sn} + Q_{ln} + Q_p + Q_g + Q_h + Q_e - Q_m \tag{1}$$

where Q_{sn} is net short-wave radiation, Q_{ln} is net long-wave radiation, Q_p is heat energy advected by precipitation, Q_g is ground heat flux, Q_h is sensible heat flux, Q_e is latent heat flux, and Q_m is heat energy advection from meltwater removal (Gray and Male, 1981; Tarboton and Luce, 1996; Dingman, 2002). The relative importance of each of these terms varies depending on latitude, topography, synoptic weather, and season (Male and Gray, 1981). Anderson (2011) showed that differential solar radiation (as a result of complex topography) played a large role in spatially varying SWE on the ground in a catchment in Southwestern Idaho, which is the regime over which this work is employed (further described in the next section). Furthermore, elevation is also identified as having a significant effect on snow distribution due to orographic controls on temperature and precipitation (Gray and Male, 1981; Anderson, 2011). In the aforementioned Idaho catchment, precipitation lapse rates ranged from 0.5042 to 0.4807 mm/m for the 2009 and 2010 water years, respectively. Also, temperature lapse rates ranged from -4.3 to -5.2 °C/km for the 2009 and 2010 water years, respectively (Anderson, 2011). These lapse rates are assumed to act in a balanced manner in terms of snow accumulation and ablation across elevation gradients. Accordingly, the proposed approach assumes that potential insolation and elevation are locally dominant controls on the spatial distribution of snow cover. The approach clearly neglects other terms from the energy budget. But we suggest in the discussion that a similar approach (or one of increased complexity) could be developed for other regions, based on terrain or energy indices reflecting other factors controlling the distribution of snow cover in these regions.

In Section 2, we describe the satellite and terrain datasets used in this study. Section 3 outlines algorithm design, development, and procedures used for calibration and validation. Model results are presented in Section 4 and we provide a brief synopsis of the results, implications, and model limitations in Section 5.

2.2   Datasets

The goal of this work is to develop a downscaling algorithm for fractional snow-covered area data derived from MODIS multispectral observations. The method is driven by operational, accessible soft datasets from remote sensing platforms. This section provides a brief outline of the data used in this study.

2.2.1   Remotely Sensed Snow Cover: Hillslope Scale

As of this writing, the Landsat Program is celebrating 40 years of high-resolution, global data observation, offering a unique retrospective and near real-time data record for many applications. Multispectral band information from the Landsat Thematic Mapper (TM) and Enhanced Thematic Mapper (ETM+) instruments is often used for automated mapping of snow cover. The Normalized Difference Snow Index (NDSI) has been used in efforts to distinguish snow-covered pixels from other land surfaces, leveraging the high and low reflectance of snow in the visible and short-wave infrared portions of the electromagnetic spectrum, respectively (Dozier, 1989). This ratio is described as

$$NDSI = \frac{R_{vis} - R_{swir}}{R_{vis} + R_{swir}} \tag{2}$$

where R_{vis} represents reflectance in a visible band and R_{swir} is reflectance in a short-wave infrared band. The NDSI is an analog to the previously defined (Tucker, 1979) and ubiquitously used Normalized Difference Vegetation Index (NDVI), which utilizes

similar principles to estimate vegetation properties. Other studies have exploited spectral mixture analyses to classify snow-covered and snow-free pixels, utilizing spectral libraries for pure end-member reflectance values and solving a set of linear combinations of their relative fractions for the observed reflectance in each pixel (e.g., Nolin et al., 1993; Rosenthal and Dozier, 1996; Painter et al., 2003).

In this study, a series of Landsat scenes over a mid-latitude, semi-arid region in southwestern Idaho (path/row 41/30) are compiled over a range of winter and spring season dates between 2000 and 2011. We employ the NDSI to estimate binary snow coverage. These scenes serve as high-resolution calibration and validation data for the development of the downscaling routine. A combination of Landsat TM and ETM+ scenes are chosen in which cloud cover is minimal (i.e., < 20% for whole scene) and qualitatively inspected such that any incident cloud cover does not occur over the mountainous regions of interest (Table 1). Within the Landsat scenes, we choose subsets known to retain seasonal snow cover for calibration and validation regions and that are of interest for modeling exercises (Figure 1). Subset (*a*) in Figure 1 contains the Dry Creek Experimental Watershed (DCEW), a 27 km^2 watershed north of Boise (Stieglitz et al., 2003; McNamara et al., 2005; Tyler et al., 2008; Kelleners et al., 2010; Kunkel et al., 2011; Graham et al., 2012), while subset (*b*) contains Reynolds Creek Experimental Watershed (RCEW), a 239 km^2 watershed in the Owyhee mountains that is maintained by the USDA Agricultural Research Service (Johnson and Hanson, 1995; Marks et al., 2001; Winstral and Marks, 2002; Flerchinger et al., 2010; Reba et al., 2011). Figure 2 shows Landsat-derived snow cover across subset *b*. Methods for classification of Landsat snow-covered pixels are described in further detail in Section 3.

2.2.2   Remotely Sensed Snow Cover: Macro-Scale

MODIS MOD10A1 Level 3 Version 5 (Hall et al., 2006) data are obtained in hierarchical data format (HDF) for downscaling. This product is a daily retrieval of f_{SCA} based on data in visible and short-wave infrared bands from the MODIS sensor onboard the NASA Terra satellite. The MOD10A1 product produces f_{SCA} estimates based on an empirical linear relationship between MODIS NDSI and pixel snow fraction, inferred from Landsat data using an NDSI threshold approach. Figure 3 illustrates MOD10A1 f_{SCA} over subset *b*. The Aqua satellite MODIS sensor is used to derive a similar product (MYD10A1), but we choose to use the Terra version in this study. In validation, Terra fractional snow cover estimates performed better than Aqua in terms of root-mean-squared error, largely due to a pixel misregistration issue between NDSI bands in the Aqua MODIS instrument (Salomonson and Appel, 2006). Recent work suggests that the MOD10A1 fractional snow cover potentially overestimates snow cover fraction in some regions, particularly in North America (Rittger et al., 2012). A more recent f_{SCA} product, the MODIS Snow-Covered Area and Grain size (MODSCAG) model, utilizes spectral mixture analysis with MODIS reflectance data to estimate f_{SCA} and has demonstrated promising results in validation (Painter et al., 2009; Rittger et al., 2012). However, since the purpose of this study is not to evaluate the skill of a particular remote sensing product, and since the MODSCAG products are not readily available at present, we use Terra MOD10A1 data for simplicity. Future work will explore the utilitiy of the downscaling approach with other snow remote sensing products.
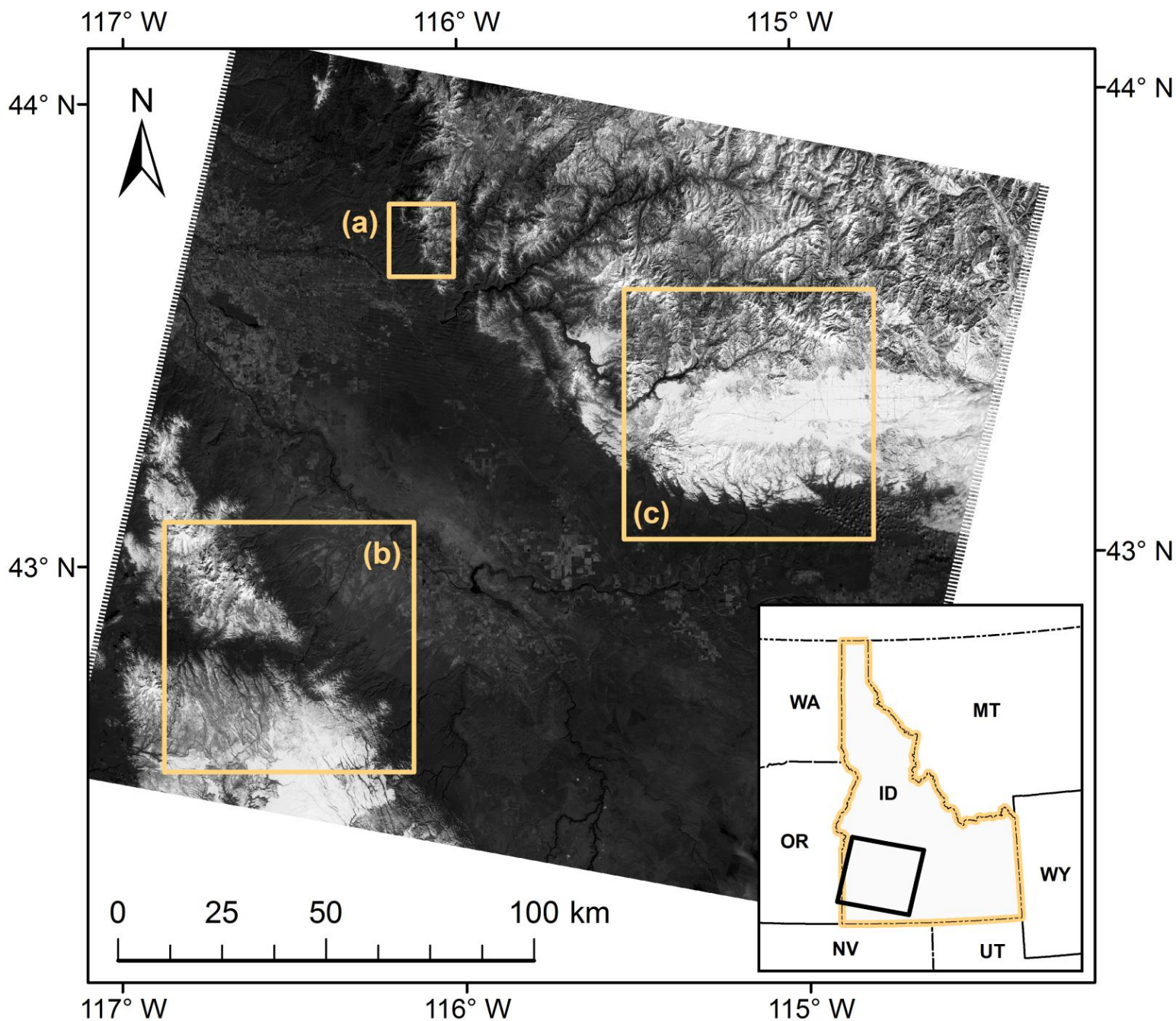
Figure 1. Landsat band 2 image (path/row: 41/30) for 18 March 2010 with SW Idaho location inset. The model is calibrated over subset *a* and validated over subsets *b* and *c*.
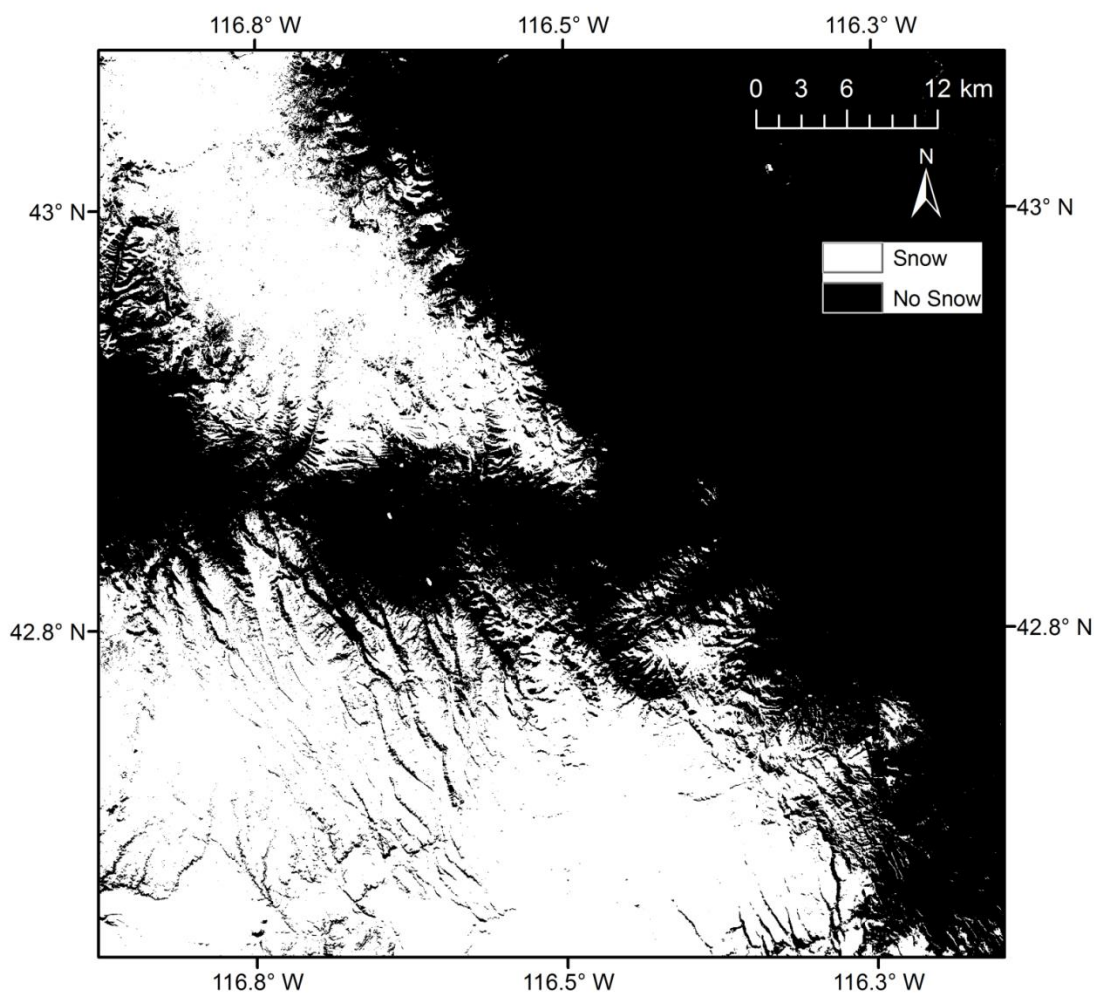
Figure 2. **Binary snow cover at 30 m resolution from Landsat across subset _b_ on 18 March 2010. Snow cover is assigned using the normalized difference snow index.**

Table 1. **Image calibration dates and sensors utilized with corresponding cloud coverage for the Landsat scenes used in this study. All scenes are path 41, row 30.**

Scene #	Date	TM 5	ETM+ 7	Cloud Cover %
1	02/03/2000	x		0
2	02/19/2000		x	0
3	03/01/2001		x	0
4	04/18/2001		x	4
5	05/04/2001		x	0
6	02/16/2002		x	2
7	03/04/2002		x	2
8	04/08/2003		x	6
9	05/10/2006	x		0
10	04/27/2007	x		0
11	03/12/2008	x		20
12	05/15/2008	x		13
13	02/01/2011	x		6

2.2.3   Terrain Data

      We use Shuttle Radar Topography Mission (SRTM) elevation data acquired from the Global Land Cover Facility. This dataset was acquired by the Space Shuttle Endeavour on mission STS-99 during February 2000 and provides nearly global high-resolution coverage. The WRS-2 tile edition of the 30 m DEM, which is coincident with the Landsat scene of interest was obtained, substantially easing comparisons between modeled and observed Landsat snow covered/snow free pixels during the calibration and validation phases of the study. This DEM grid is subset into the same regions as described for the Landsat scenes. Fig ures 4, 5, and 6 show the elevation across subsets *a*, *b*, and *c*, respectively, with the 500 m MODIS grid mesh overlain. Local topographic slope

(gradient in direction of steepest descent) and aspect (cardinal direction of steepest descent) are extracted using the topographic modeling tools in ENVI. A mountain slope solar radiation algorithm (Swift, 1976) is applied to these terrain data in MATLAB to produce indices for daily, integrated potential incoming solar radiation (insolation). Details concerning the radiation computation and treatment are discussed in the methodology section of this paper.
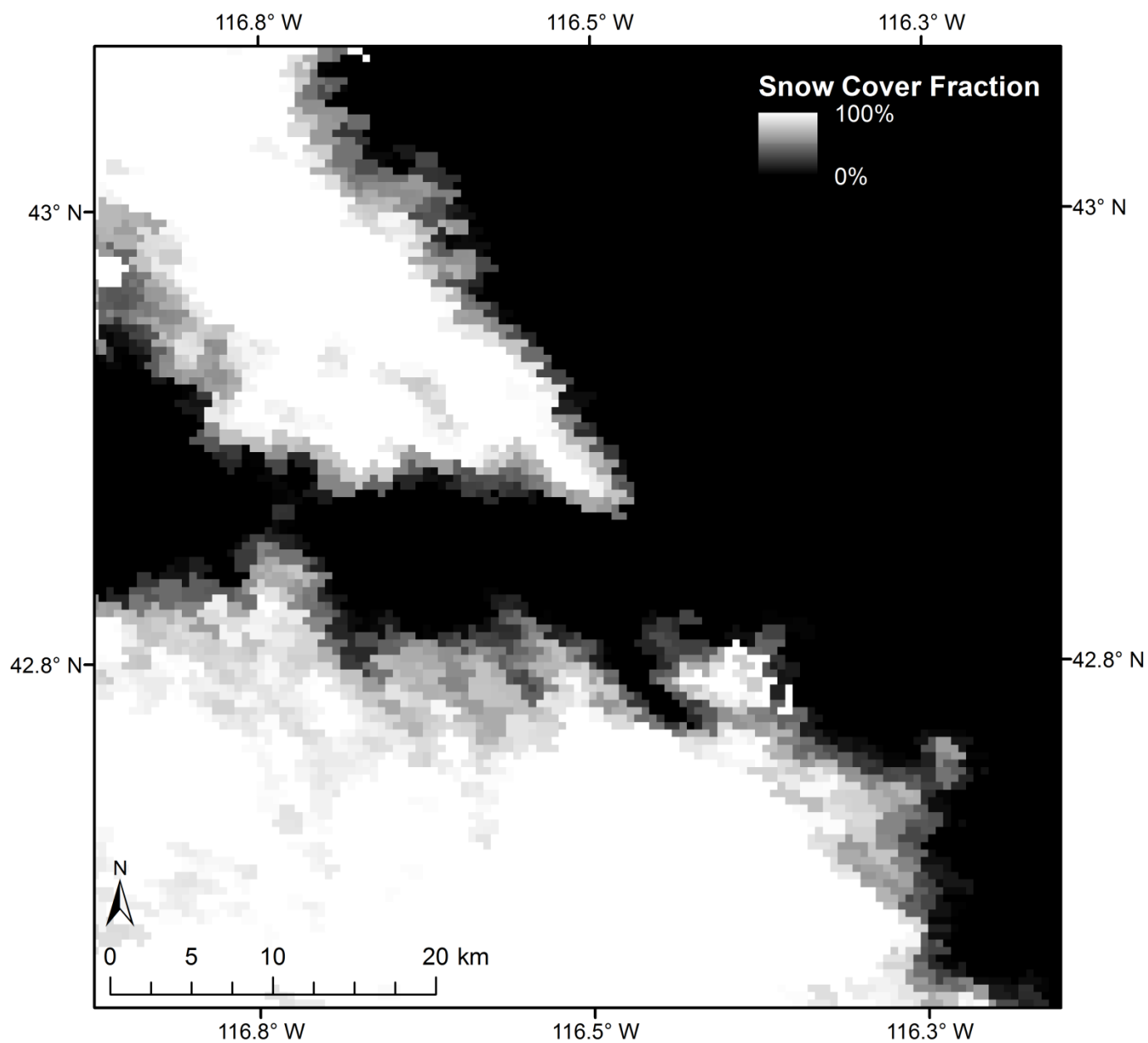
Figure 3. **Fractional Snow-Covered Area at 500 m resolution from MOD10A1 across subset *b* on 18 March 2010.**
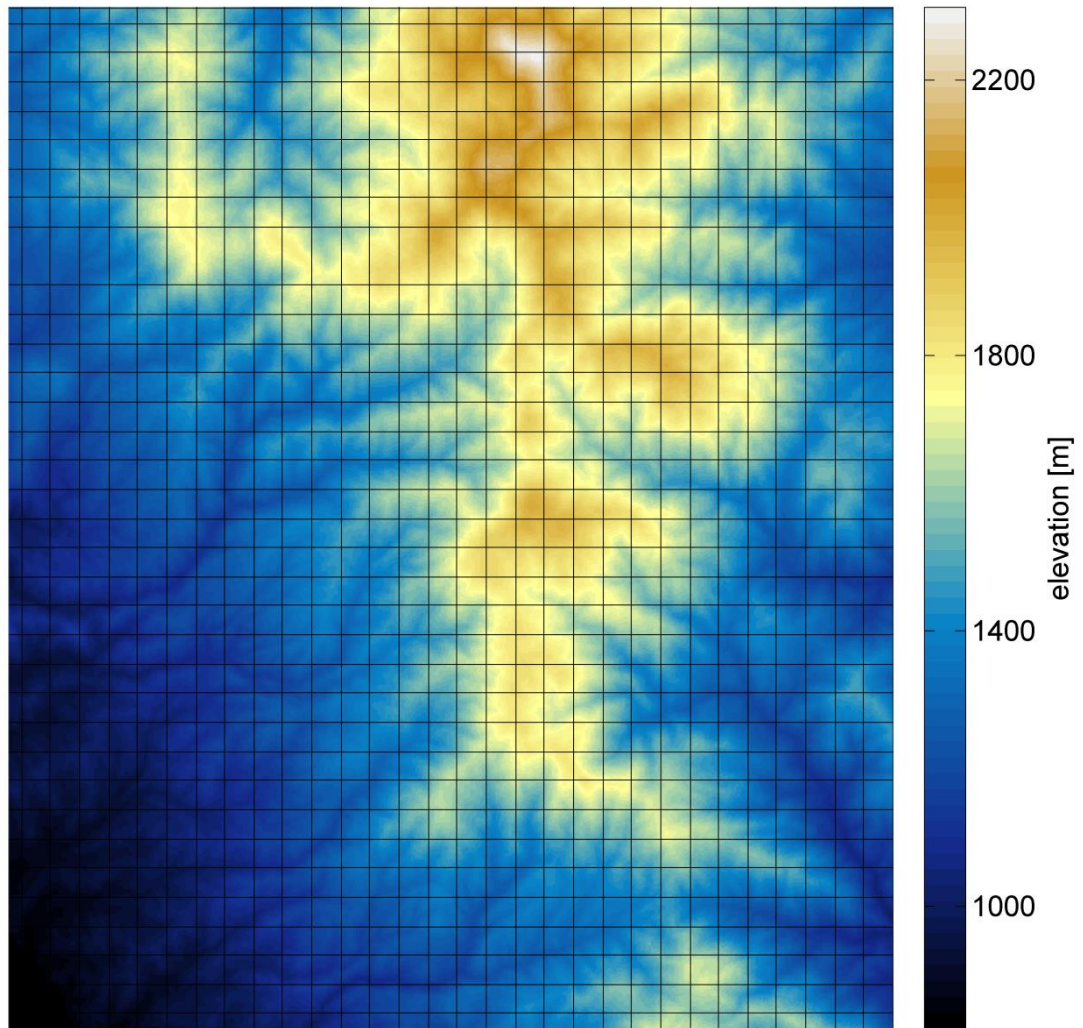
Figure 4. **SRTM digital elevation model at 30 m resolution across subset *a* with MODIS 500 m grid mesh overlay. See Figure 1 for context.**
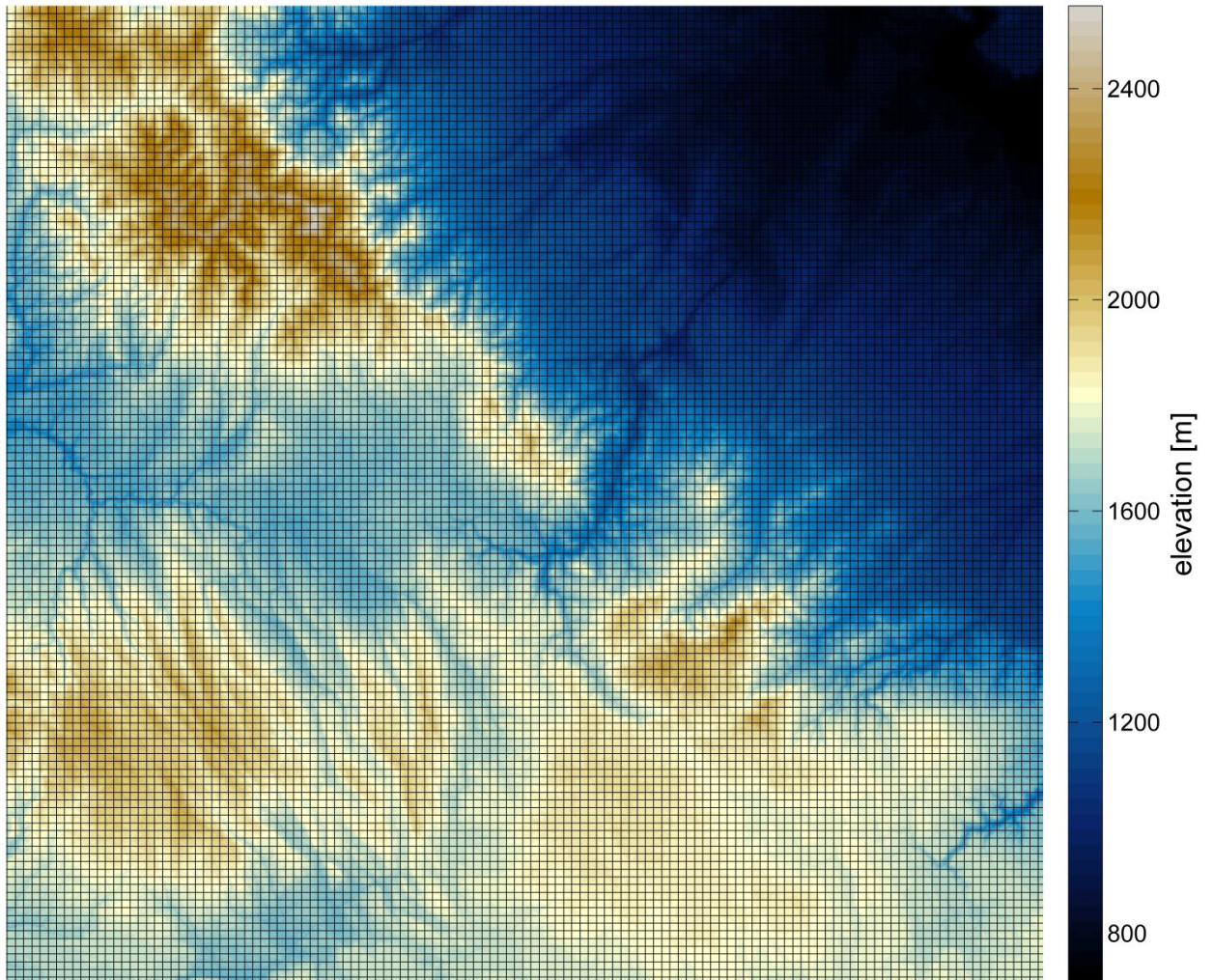
Figure 5.   **SRTM digital elevation model at 30 m resolution across subset *b* with MODIS 500 m grid mesh overlay.**
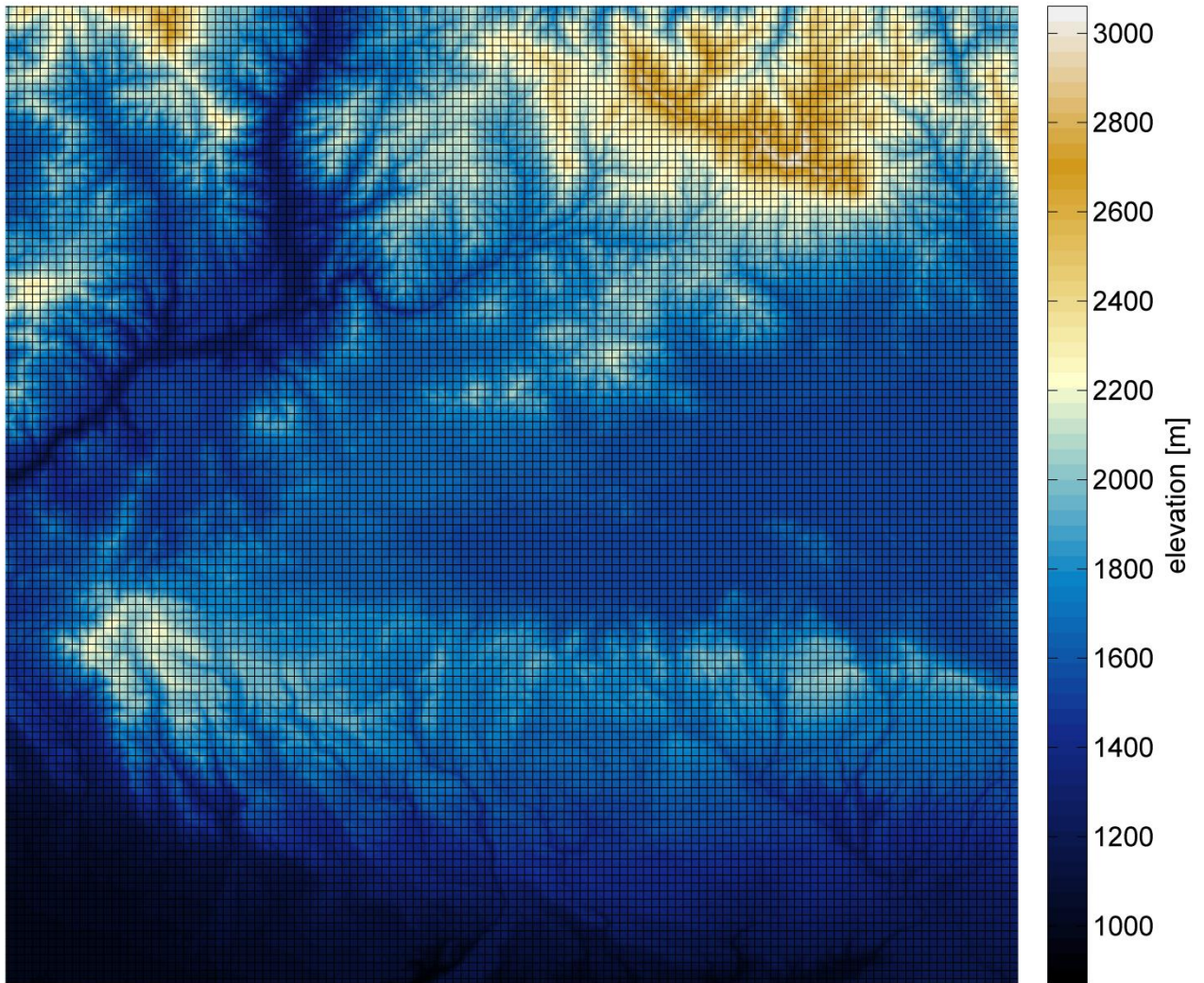
Figure 6. **SRTM digital elevation model at 30 m resolution across subset *c* with MODIS 500 m grid mesh overlay.**

2.3   Methods

Described in this section is the downscaling model used to derive 30 m binary snow cover maps using 500 m f_{SCA} estimates from MODIS. The developed algorithm makes several important assumptions about drivers of variable snow cover in the study region, which are enumerated here:

- (1) Two variables, potential insolation and elevation, dominantly control the differential ablation of snow cover throughout spring melt at the 30m to 500 m scales investigated here (Anderson, 2011),

- (2) Snow will disappear from pixels prone to increased solar radiation exposure before those that are more obscured,

- (3) Higher elevation pixels will retain a deeper snow pack due to orographic effects during initial accumulation and temperature lapse rates during melt onset. This effect should be preserved during ablation, as lower elevation pixels melt before higher ones.

The degree to which these predictor variables affect the snow cover distribution is a question that is addressed by this study and is likely a function of the spatial resolution at which the f_{SCA} observation occurs (e.g., 500 m in the case of individual MOD10A1 grid cells). Figure 7 provides qualitative insight into the importance of the aforementioned predictor variables within 500 m MODIS cells of varying snow cover fractions.

This section is organized as follows. First, the calculation of solar radiation indices is described. Next, the derivation of the 30 m binary snow covered maps from the Landsat scenes shown in Table 1 is discussed. Reprojection and subsetting of the MODIS data for the region is presented. The downscaling routine is then described, followed by the parameter calibration and validation methods.
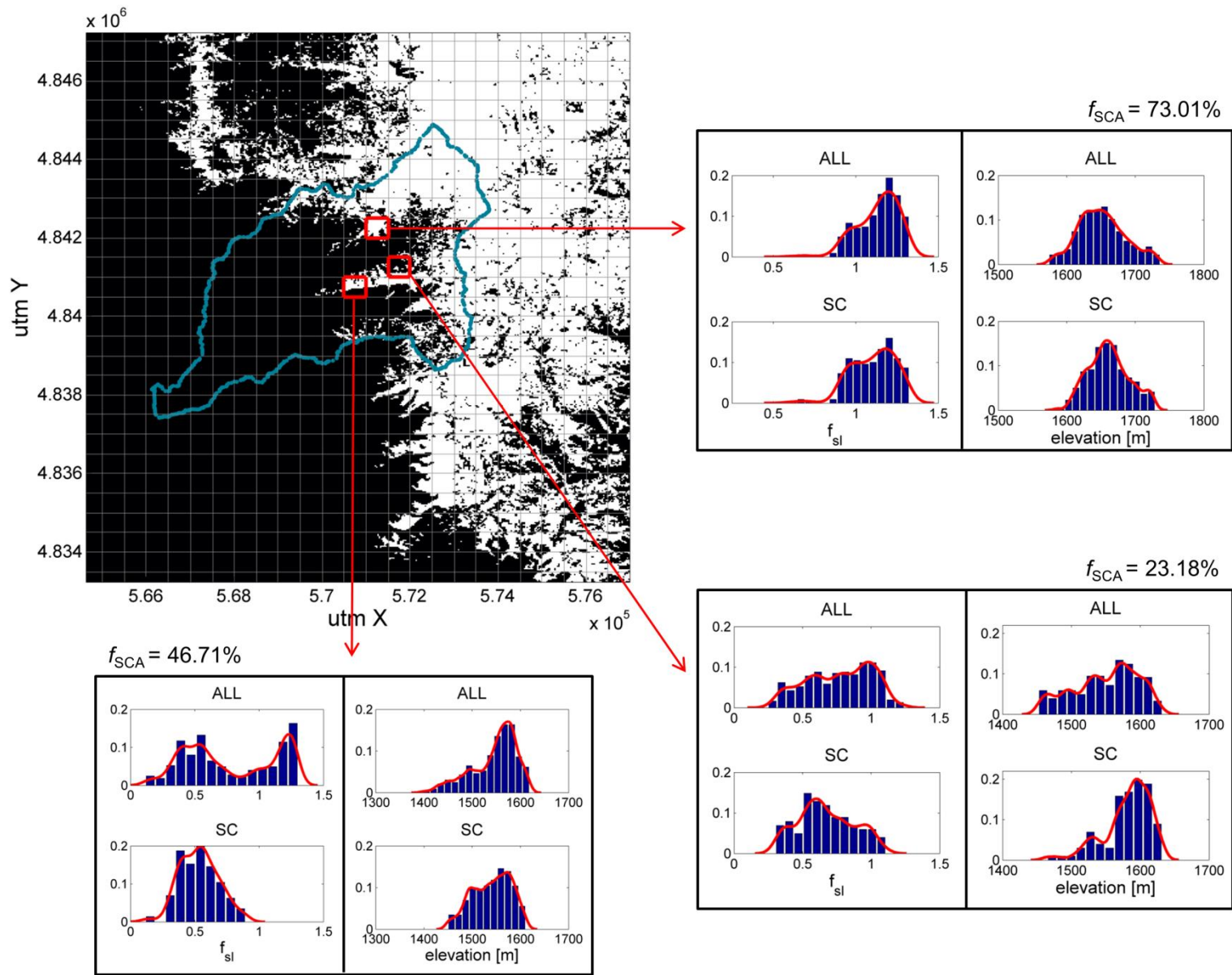
Figure 7. Landsat snow cover across DCEW with MODIS grid mesh overlay (upper left). Radiation slope factor and elevation index histograms within three subset MODIS cells of varying f_{SCA}. For each cell, the histogram for all slope factor and elevation (ALL) are shown juxtaposed with those only with snow cover (SC).

2.3.1   Solar Radiation Index

To calculate solar radiation, an algorithm is employed requiring Julian date,

latitude, slope inclination,   and aspect as inputs to estimate daily potential integrated

irradiation at each model pixel (Swift, 1976). Terrain slope and aspect data are extracted

from a 30 m DEM as presented in Section 2. The radiation model does not account for

atmospheric attenuation due to changes in optical depth or aerosol presence, making only

a series of trigonometric adjustments to the extraterrestrial solar constant. Nor does the

model account for shading from adjacent blocking ridges. See Appendix A.1 for details

concerning the radiation calculations. We are interested in the relative comparison of

insolation values over complex terrain within MODIS grid pixels and thus do not attempt

to adjust for attenuation effects, assuming constant atmospheric conditions across the cell

at any given time. In order to achieve a relative value for solar radiation, each pixel's

potential value is normalized to that of a horizontal plane in the same location. That is

$$f_{sl} = \frac{R_{slope}}{R_{horiz}} \tag{3}$$

where R_{slope} and R_{horiz} are pixel-scale potential insolation on the local slope and

horizontal plane, respectively, and f_{sl} is the normalized term referred to as the slope

factor. We compute the slope factor for every day over each subset domain depicted in

Figure 1. For the computed time-series of f_{sl} over each subset region, there occur

domain-wide minimum and maximum values calculated value throughout the snowmelt

season. This is due to the dynamic range of solar declination angles throughout the year

and the distribution of slopes and aspects in a given region of complex terrain. These

extreme values are stored, denoted by $f_{sl}{}^{max}$ and $f_{sl}{}^{min}$ representing the maximum and

minimum observed slope factors, respectively, for each subset's seasonal time-series.

These values are used in a normalization process during the downscaling routine

described in Section 2.3.5.

2.3.2   Landsat Binary Grid Processing

An empirical method is used to identify snow-covered pixels within Landsat

subset grids. We employ the NDSI with a threshold criteria test similar to the SNOMAP

algorithm (Hall et al., 1995). NDSI is computed via Eqn. 2 with R_{vis} and R_{swir}

corresponding to Landsat bands 2 and 5, respectively. Pixels are classified in binary

manner according to the following criteria:

$$s_o = \begin{cases} \text{snow,} & \text{NDSI} \geq 0.4 \\ \text{no snow,} & otherwise \end{cases} \tag{4}$$

where s_o represents the classified state of the observed pixel. Dozier (1989) suggests

other criteria for shadowed areas and cloud discrimination, but these are neglected here,

relying on (1) the NDSI to reduce effects of viewing geometry over complex terrain and

(2) our qualitative cloud cover selection criteria.

2.3.3   MODIS Grid Processing

MODIS MOD10A1 data are acquired in hierarchical data format (HDF). We

subset the data over the study region and re-project from its native Sinusoidal grid into a

UTM coordinate system using the MODIS Reprojection Tool (MRT) from the NASA

Land Processes Distributed Active Archive Center (LP-DAAC). Although a snow cover

grid exists for each day, regions and days are frequently corrupted by cloud cover and

poor sensor viewing geometry. To combat this issue, temporal smoothing splines can be

employed to estimate snow cover fraction during data gap periods (e.g., Dozier and Frew,

2009). In this study, we execute preliminary downscaling on a MODIS f_{SCA} image that temporally coincides with 30 m data from a clear Landsat overpass (18 March, 2010), which is used for preliminary validation. Since Landsat and MODIS obtained cloud-free observations on this date, no temporal smoothing is necessary.

For simplicity, we remap the 500 m MODIS f_{SCA} product onto a 30 m resolution grid that is coincident with the SRTM DEM. It is on this geospatial template that the binary snow-covered classification is assigned. A two-dimensional nearest-neighbor interpolation is used to register the MODIS f_{SCA} grid to the resolution and position of the DEM. The 30 m resolution grids, which include the remapped MODIS f_{SCA}, Landsat binary snow cover, slope factor, and elevation, are cropped to the MODIS grid boundaries, eliminating a small number of pixels at the grid margins. Because the boundaries of the reprojected MODIS grid do not perfectly align with the boundaries of the SRTM DEM and Landsat multispectral images, there is an approximate geolocation offset of 9.96 m between the grids. It should be noted that this offset is well below the MODIS geo-location uncertainty of approximately 50 m at nadir (Wolfe et al., 2002). Results depicting differences between MODIS f_{SCA} and the f_{SCA} at 500 m computed from Landsat binary snow cover show approximately zero mean and normally distributed disparities, suggesting that the grid offset does not produce systematic errors that would influence the calibration of the downscaling routine.

2.3.4   Downscaling Routine

Downscaling is performed over the MODIS grid on a pixel-by-pixel basis. Within each 500 m pixel, the corresponding 30 m elevations (z) and insolation slope factors (f_{sl}) are selected. This subset of z and f_{sl} is standardized within the entire MODIS. Elevation

at each 30 m pixel is normalized to the extreme values observed in a given 500 m

MODIS pixel in a reverse fashion such that the highest pixels within each MODIS pixel

have the lowest normalized elevation,

$$z_{norm} = \frac{z - z_{max}}{z_{min} - z_{max}} \qquad (5)$$

where z_{norm} is the variable name assigned to the normalized elevation grid,

z_{max} represents the maximum elevation, and z_{min} represents the minimum. By

definition, values of z_{norm} within each MODIS pixel will vary on the interval [0,1].

A normalized f_{sl} is also computed within each MODIS pixel. Rather than

normalizing to the extreme values within each MODIS pixel, we normalize to the

maximum and minimum calculated slope factors across the domain for the entire season,

$$f_{norm} = \frac{f_{sl}}{f_{sl}^{max} - f_{sl}^{min}} \qquad (6)$$

where f_{sl}^{max} is the maximum slope factor for the whole season, and f_{sl}^{min} is the

respective minimum. Since there exists a 30 m pixel in every domain that is sufficiently

steep and North-facing to yield zero potential direct irradiance on at least one day of the

year, the minimum observed slope factor, f_{sl}^{min}, for each domain is zero. Thus, Eqn. 6

reduces to

$$f_{norm} = \frac{f_{sl}}{f_{sl}^{max}}. \qquad (7)$$

Since slope factor is normalized to domain-wide seasonal maximum, the values of f_{norm}

will vary by Julian day. This serves to capture the intra-seasonal variations in solar

declination and, therefore, in insolation as a driver of ablation. The distribution of slope

factor tends to become more narrow throughout the spring season as the sun transitions to

a higher position in the sky. The range of values of f_{norm} within each MODIS pixel will thus be narrower than [0,1] on any given date except for the time and location(s) containing the maximum seasonal slope factor, $f_{sl}{}^{max}$.

We achieve a standardized grid at each MODIS pixel by combining the normalized insolation and elevation. If we treat the grid of f_{norm} and z_{norm} values within each MODIS pixel as matrices X_1 and X_2, respectively, we can construct a convex combination matrix T_s of the form:

$$\sum_{i=1}^{m} w_i \cdot X_i \tag{8}$$

where m is a positive integer (equal to 2 in the case of this model), X_i are the normalized matrices of insolation and elevation (as above) belonging to T_s, and w_i are non-negative scalars, which sum to one (Bertsekas et al., 2003). In the presented case of two explanatory physiographic variables, Eqn. 8 becomes:

$$T_s = w \cdot X_1 + (1 - w) \cdot X_2 \tag{9}$$

where the matrix T_s represents a standardized grid representing a 'terrain score' for which the scalar weights w and $1 - w$ represent the respective contributions from insolation and elevation to the snow cover distribution. Within each MODIS pixel, the empirical cumulative distribution function (CDF) of the terrain score can be constructed. We then use the retrieved MODIS f_{SCA} value, which varies from zero to one, to invert the empirical CDF of T_s to determine a critical value in T_s that we take as the threshold for the occurrence of snow cover within the MODIS pixel. This critical value is designated as variable T_k. Specifically, snow cover is assigned to pixels with values of T_s below T_k. The remaining pixels, representing a fraction $1 - f_{SCA}$ within each MODIS pixel, are

assumed to be snow-free. This approach preserves the original snow fraction observed by the individual MODIS pixel and thus preserves SCA at the basin-scale. The snow-mapping model is of the form:

$$
s_\mathrm{m} = \begin{cases} \text{snow}, & \int_0^{T_k} \mathrm{F}(\boldsymbol{T_s}) \\ \text{no snow}, & \int_{T_k}^{T_m} \mathrm{F}(\boldsymbol{T_s}) \end{cases} \tag{10}
$$

where s_m is the classified state of the modeled pixel and T_m is the maximum value occurring in $\boldsymbol{T_s}$. Numerically, this algorithm is straightforward and computationally inexpensive since the only variable requiring solution is w. This approach reflects our assumptions about the drivers of ablation in a couple of important ways. First, by normalizing the elevation pixels in reverse order, we assign greater values to pixels of lower elevation. Within each MODIS pixel boundary, the pixels with the lowest elevations will tend to be associated with higher values of $\boldsymbol{T_s}$, and will therefore tend to be assigned a snow-free status before those pixels with higher elevations. In contrast to the reverse-normalizing process used with elevation, slope factors are normalized such that those pixels with the highest values of f_{sl} within a MODIS pixel also have the highest values of f_{norm}. Thus, those pixels with the highest values of f_{sl} (prone to relatively more solar radiation) will correspondingly have higher values of f_{norm}, which will tend to increase $\boldsymbol{T_s}$. All else being equal, these pixels will tend to be classified as snow-free more frequently. Finally, by combining z_{norm} and f_{norm} in an efficient, linear combination model, the approach requires only one parameter (w) to fit. This parameter is informed by Landsat data and represents the relative contributions of potential solar radiation and elevation within each MODIS pixel to the persistence of snow cover. The iterative calibration and validation methods are outlined in the next section.

2.3.5   Parameter Calibration

As described, the downscaling model requires only an input value for the scalar

weight w in Eqn. 9 in addition to the z_{norm} and f_{norm} maps. We use an iterative

approach to calibrate this parameter that optimizes the downscaled binary snow cover

maps relative to the Landsat binary snow cover predictions. To test the transferability of

parameters, we use only region a in Figure 1 to calibrate w.

During the calibration phase, the 500 m resolution f_{SCA} is computed directly from

Landsat binary snow cover maps using an iterative, moving-window approach. This

eliminates the impact of potential errors in the MODIS retrieval of f_{SCA} from influencing

the calibration of the algorithm. The calibration approach iteratively moves a 500 m

square window over three different co-registered 30 m resolution grids for region a: (1)

Landsat binary snow cover, (2) elevation, and (3) potential insolation. For robustness, we

move the window across every possible 500 m window over the subset domain, rather

than just those windows falling on the MODIS grid footprint. Within each window, the

fractional snow cover is derived as the simple fraction of snow-covered pixels predicted

with the critical NDSI threshold,

$$f_{SCA}^{Landsat} = \frac{n_s}{N} \tag{11}$$

where $f_{SCA}^{Landsat}$ is the fractional snow cover inferred from the Landsat scene within the

500 m window, n_s represents the number of pixels where snow cover is observed, and N

represents the total number of pixels in the window. By default, the downscaling model

performs perfectly when f_{SCA} equals zero or one, regardless of the value of w. Therefore,

we only analyze those windows with fractional snow cover within the range $0.1 \leq f_{\text{SCA}}^{Landsat} \leq 0.9$. This prevents misleading statistical analysis of the model results.

For windows satisfying the given range, we iterate through candidate values, w, on [0,1] in increments of 0.01. This leads to 101 potential 30 m resolution binary snow cover maps per 500 m window, each with a fixed value of f_{SCA} and associated with a unique value of w. For each iteration, binary classification performance metrics are used to construct a confusion matrix. True positive (TP), false positive (FP), true negative (TN), and false negative (FN) occurrences are obtained by comparing the Landsat derived 30 m binary snow cover map to each of the 101 realizations on a pixel-by-pixel basis. Where the model predicts snow when Landsat NDSI suggests no snow, a false positive (i.e., type I error) occurs. Conversely, false negatives (type II errors) occur where Landsat NDSI suggests snow cover but where the model predicts snow-free conditions. The occurrence of these four possible outcomes allows us to calculate precision (p) and recall (r). Precision equals the proportion of modeled snow-covered pixels that are correctly identified as snow,

$$p = \frac{\text{TP}}{\text{TP+FP}} . \tag{12}$$

Recall equals the proportion of observed snow-covered pixels that are correctly modeled (Powers, 2011),

$$r = \frac{\text{TP}}{\text{TP+FN}} . \tag{13}$$

This analysis closely follows the approach of Rittger et al. (2012) in which the accuracy of MODIS products is evaluated. Accordingly, the harmonic mean of p and r is the so-called F-measure,

$$F = 2 \cdot \frac{p \cdot r}{p+r} \tag{14}$$

which provides a robust statistical balance for such a binary test. We store the F-measure

for each candidate w for every analyzed window. Taking the mean of all windows for

each value of w produces a vector of F-measure as a function of w, from which the

maximum F-measure and associated w can be retrieved. We are thus calibrating the value

of w to maximize the spatially averaged F-measure. This analysis is repeated for all

available Landsat scenes used in calibration .

2.3.6   Evaluation of Statistical Analysis

Since we are driving the downscaling routine with f_{SCA} information, the outcome

of the performance metrics are subject to particular constraints. For instance, when f_{SCA}

input to the downscaling model is constrained to the value of f_{SCA} inferred from Landsat,

$f_{SCA}^{Landsat}$, the confusion matrix between observation and model is symmetric, meaning

the number of false positives and false negatives are equal. This occurs because every

time a false positive arises, we miss an opportunity to correctly classify a snow-covered

pixel, thus generating a false negative elsewhere in the grid. This leads to equality in

precision and recall and it can be demonstrated that the F-measure simplifies to p or r

when the f_{SCA} value input to the model and the f_{SCA} value to which the model is being

calibrated are identical. Thus, the y-axis in Figure 9 could also be labeled as precision or

recall since, during calibration, our model always receives as input the value of $f_{SCA}^{Landsat}$.

Calibration could, therefore, be simplified by simply maximizing precision. However,

during validation, the map of f_{SCA} values input to the downscaling model comes from the

MOD10A1 product and is not necessarily equal to the map of f_{SCA} that would have been

derived from Landsat at the same spatial scale. In validation, therefore, it is necessary to perform assessment via the *F*-measure since p and r will often not be equal.

It is also important to determine a minimum acceptable value of the *F*-measure that indicates the model is outperforming a random assignment of binary snow cover for a given MOD10A1 f_{SCA}. For any given Landsat-derived binary snow cover map, a corresponding map of randomly assigned snow cover with identical f_{SCA} will produce an *F*-measure that is on the order of the f_{SCA} value. Therefore, for a given f_{SCA} value, an *F*-measure for the downscaling model that is outside the range of variability of the corresponding *F*-measures of an ensemble of randomly produced binary snow cover maps would indicate that the model is moving snow toward the correct locations. We estimate the range of variability through a Monte Carlo simulation for a range of f_{SCA} possibilities from 0.1 to 0.9. For each possible f_{SCA}, we randomly produce a synthetic true binary snow cover map. For each synthetic true map, we generate an ensemble of 10,000 random binary snow cover maps having an f_{SCA} value that is within a fixed percentage, δ, of the snow cover fraction of the synthetic truth. This approach allows for discrepancies between the retrieved f_{SCA} (i.e., that which would be input to the downscaling model) and the true binary snow cover (i.e., that which would be inferred from Landsat). We calculate the *F*-measure for all random snow cover maps and every f_{SCA} value. For a given f_{SCA}, we compute the expected value of *F* and its variance, denoted μF_{random} and σF_{random}, respectively. Figure 8 shows the relationship between *F*-measure and f_{SCA} and illustrates the variability in *F* due to randomness for $\delta = 0.1$. The variability in F-measure tends to decrease as f_{SCA} approaches 0.9 because pixels randomly assigned as

snow cover are more likely to be correct than at lower values of f_{SCA}. *F*-measure

ensembles tend to be distributed normally across each value of f_{SCA}.
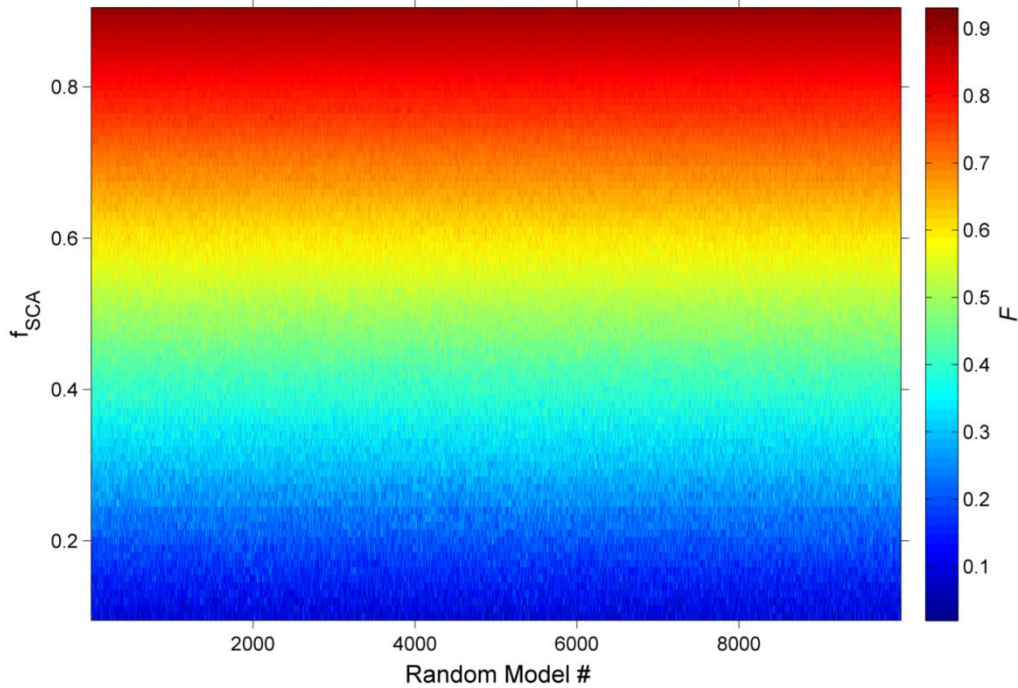
Figure 8. *F*-measures for randomly applied snow cover models plotted with changes in observed snow cover fraction. Random model snow cover fractions are constrained to within *δ*=10% of the observation grid in this simulation.

2.4 Results

In this section, we present the results of downscaling model analysis. Presented

first are the weight parameter calibration results, which provide a single constant to input

to the model during a validation study. The results from this validation are given next.

We downscale MOD10A1 fractional snow cover data to the resolution of the SRTM

DEM and insolation grid. The results are conveyed as a function of differing snow

fraction throughout the domains. Finally, a downscaling analysis is performed using a

synthetic "ideal" observation of f_{SCA}, which is simply a 500 m aggregate of the Landsat

validation snow cover observation allowing us to fix the snow fraction to the observation,

giving the model maximum opportunity to perform without any discrepancy between

MODIS and Landsat.

2.4.1   Calibration Results

To obtain a calibrated parameter value, w, used in the downscaling model, we

examine the performance of the F-measure across snow cover grids for 13 Landsat

scenes in the manner described above. A vector of F-measure statistics is generated for

each candidate w and 500 m window. The mean F-measure across all 500 m windows

and for each candidate w is computed as depicted in Figure 9.
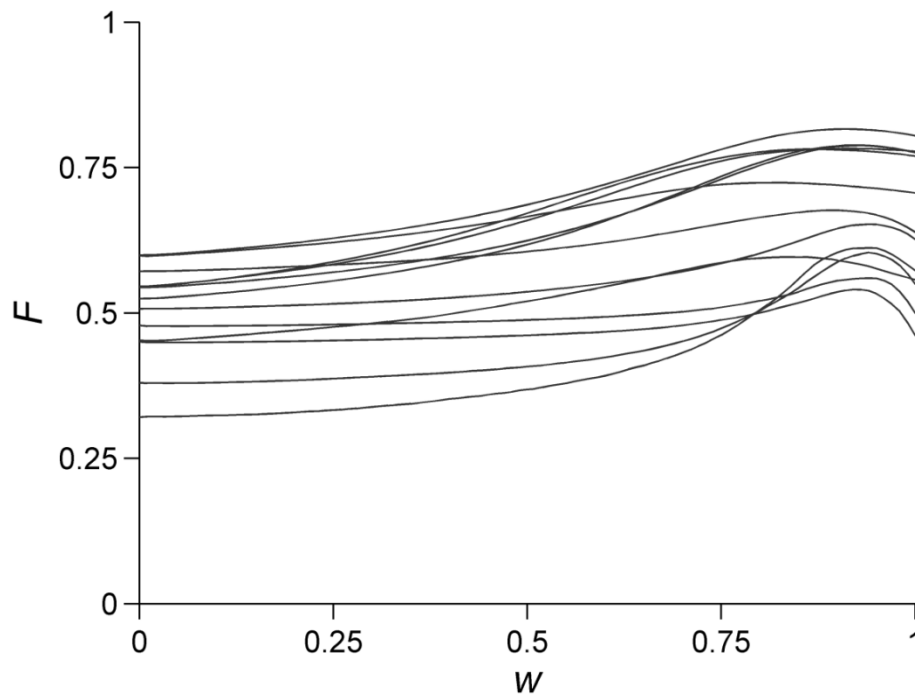
Figure 9.   Mean F-measure by parameter w for subset a for 13 temporally separated Landsat scenes. For each date, a calibration optimum is chosen which corresponds to the maximum value taken on by F.

Note that, as described in Section 3.6, the *F*-measure is identical to precision and recall in this characteristic case. The *w* value that maximizes the magnitude of F (p or r) is chosen as the optimum weight parameter for each Landsat scene (Figure 10).
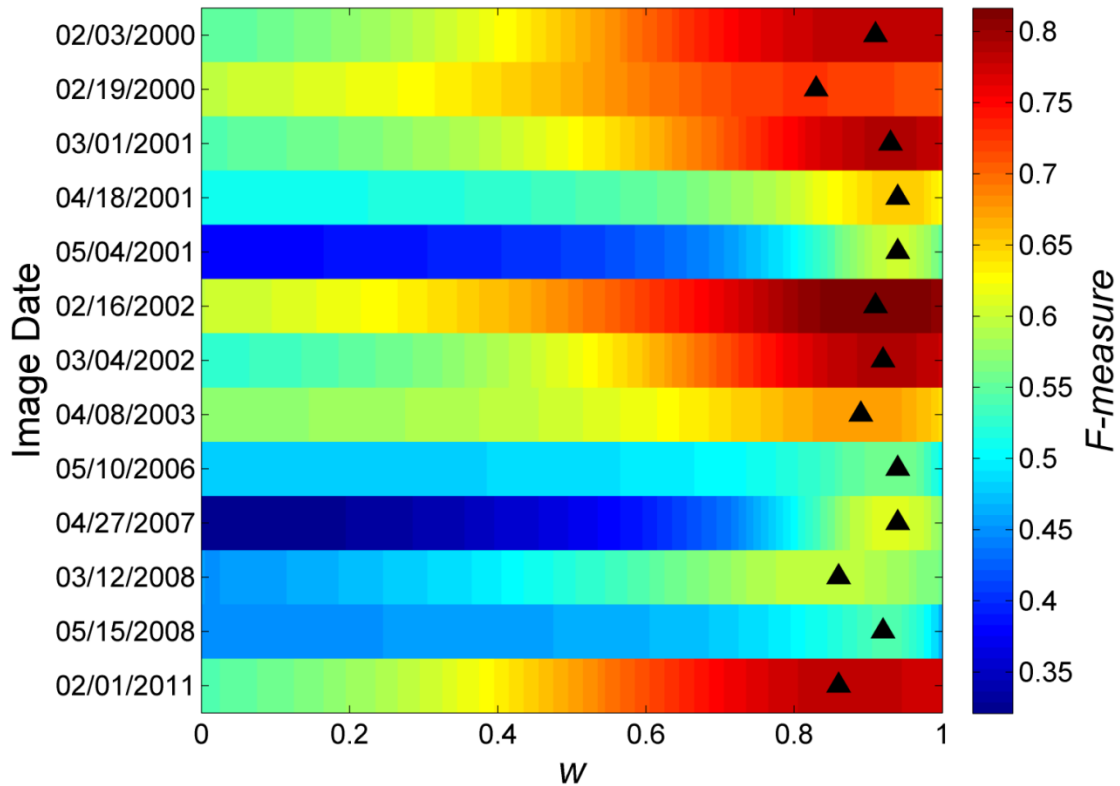
Figure 10. **Mean *F*-measure by weight parameter *w* for 13 Landsat acquisition dates. For each date, the optimum value of *w* is plotted as a black triangle.**

For 13 different dates of Landsat acquisition, the calibrated parameter *w* varies within a relatively narrow range from 0.83 to 0.94. The distribution of optimal *w* values has a mean, w_μ, of 0.9069 and standard deviation, w_σ, of 0.0364. The maximum, domain-averaged *F*-measure for all calibrated Landsat scenes ranges from 0.5403 on 15 May 2008 to 0.8163 on 16 February 2002. The f_{SCA} across the whole calibration domain within

the calibration scenes ranges from less than 1% on 27 April 2007 to approximately 77% on 16 February 2002. Figure 11 depicts these resulting parameter optima by date, along with their corresponding values of F and domain-wide f_{SCA} values. Note that the F-measure maxima tend to be highest when domain snow cover fraction is also relatively high. Also note that the date with the highest F-measure in calibration (16 February 2002) is also the date with highest snow cover fraction for the whole domain (Figure 12).
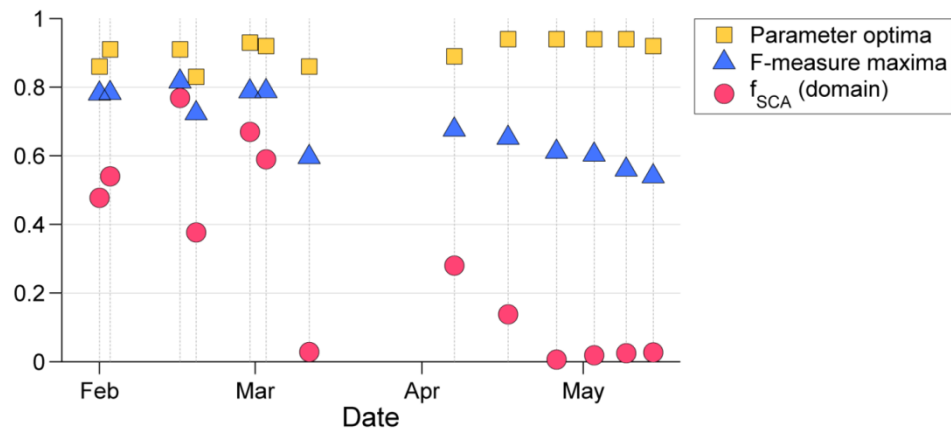
Figure 11.   Results from calibration phase. Parameter optima (yellow squares) are chosen as the corresponding weight which maximizes the average F-measure for each date. The F maxima are shown as blue triangles. Snow cover fractions for the whole domain are plotted as red circles. Note that the x-axis dates are relative, meaning they are not all from the same snow season. Also note that the y-axis is intentionally un-labeled as all three plotted datasets are unitless and fall on the same interval [0,1].

Parameter w represents the weight assigned to the normalized slope factor f_{norm} while its complement, (1-w), is that assigned to normalized elevation z_{norm}. Thus, the calibration seems to suggest that spatial variability in insolation is the dominant of the predictor variables used because the weights appear to be relatively consistent over time (Figure 12). It should be reiterated, however, that values for f_{norm} vary with Julian date and are normalized to seasonal maxima whereas z_{norm} values are static and normalized to

each grid window. As a result, insolation (as captured by f_{norm}) exhibits a larger

dynamic range in the winter and early spring, and dominates where snow-covered pixels

are assigned in the downscaling routine. However, as the season progresses, elevation (as

captured by z_{norm}) becomes increasingly important in predicting snow cover.

2.4.2   Validation Results

Preliminary validation is performed using data from the MOD10A1 Version 005

f_{SCA} product (Hall et al., 2006) as input to the downscaling model and Landsat binary

snow cover to facilitate statistical analyses. We perform validation over regions *b* and *c*

in the same Landsat scene (path/row 41/30) used for calibration (Figure 1). The

MOD10A1 and Landsat observations are acquired for 18 March 2010, a date not used in

model calibration. This date is selected because both Landsat and Terra satellites passed

over the region coincidentally during this date, obtaining a clear view of the domain. We

operate the validation in similar fashion to the calibration procedures. Every MODIS

pixel is downscaled to 30 m spacing, following the methods described in Section 2.3.4.

We use the mean of calibration w values, w_μ, to generate downscaled estimates. For all

MODIS pixels, we select for validation only those which satisfy ($0.1 \leq f_{SCA}^{Landsat} \leq 0.9$)

and ($0.1 \leq f_{SCA}^{MODIS} \leq 0.9$). These criteria are used for two reasons:

1) By default, the model performs quite well when f_{SCA} is near zero or one, so we

choose to disregard the performance at these ranges.

2) We are interested in examining the results when MOD10A1 and Landsat are in

relative agreement since we are not evaluating the performance of MOD10A1, but

rather that of the performance of the downscaling model when both products suggest the evidence of snow cover.

At windows compliant with the above criteria, the difference in f_{SCA} between the two products, Δf_{SCA}, is computed,

$$\Delta f_{SCA} = f_{SCA}^{Landsat} - f_{SCA}^{MODIS}. \tag{15}$$

Figure 12 illustrates the histogram of f_{SCA} disparity between MODIS and Landsat across each validation subset.
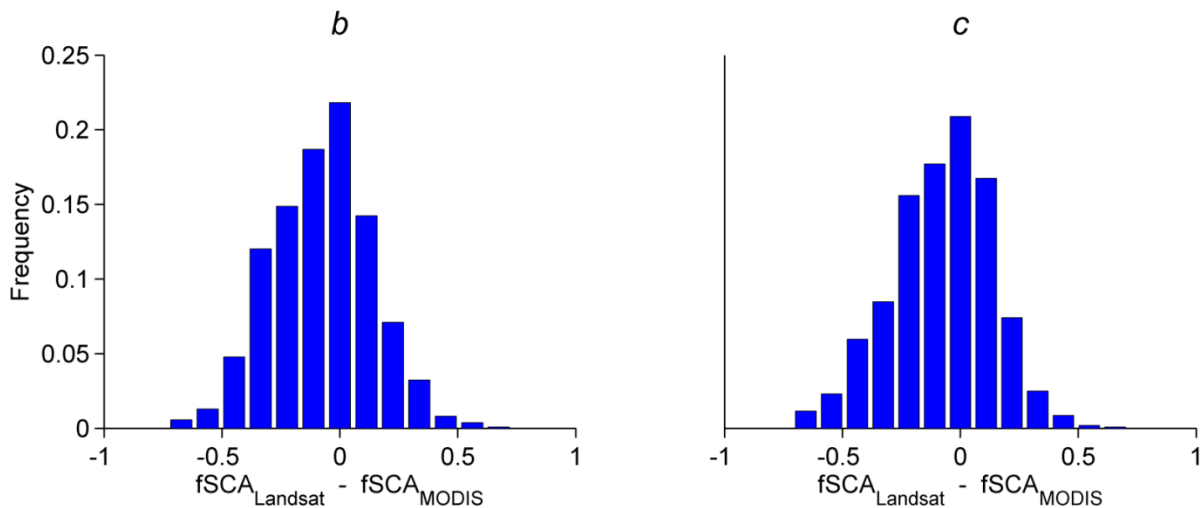
Figure 12.   Relative density histograms displaying the differences in snow cover fraction between Landsat and MODIS over the two validation subsets on 18 March 2010. Subsets b and c are shown at left and right, respectively. Note that these differences do not include occurrences where both satellites observe 0% or 100% snow cover.

We further restrict validation to those MODIS pixels satisfying ($|\Delta f_{SCA}| \leq 0.1$) to examine those observations where MODIS agrees with the observed Landsat snow fraction to within 10%. We choose this tolerance value to coincide with the choice of δ in Section 3.6. In subset regions b and c, 34.98% and 36.71% of windows fall, respectively,

within this tolerance. Note that these percentages exclude occurrences where MODIS and Landsat observed completely snow-free or snow-covered conditions. We then compare the F-measures calculated between downscaled MODIS and observed Landsat binary snow cover with the scores computed via random model generation from Section 3.6. If, for a given f_{SCA}, the corresponding F-measure within that MODIS pixel exceeds μF_{random}, we suggest that the model is performing agreeably relative to a random assignment of snow-covered locations. Figure 13 depicts the results of validation, displaying downscaling model F-measure for given values of f_{SCA}. Since we set constraints on Δf_{SCA} to be within 10%, we plot the measures against the snow fractions for both the downscaled MOD10A1 f_{SCA} and Landsat f_{SCA} computed over the MOD10A1 footprint.
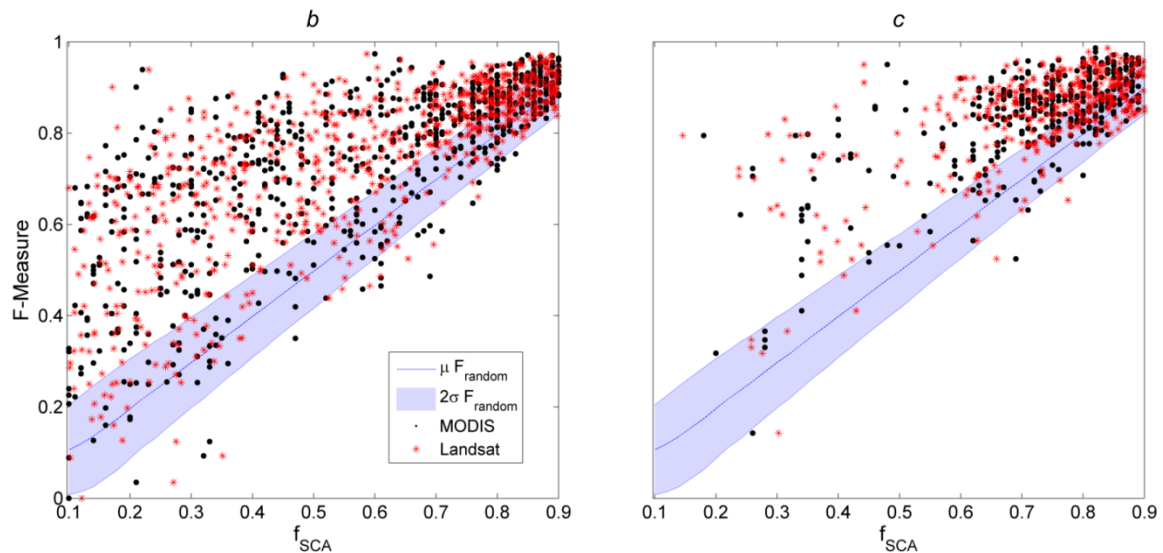
Figure 13. Modeled F-measure as a function of f_{SCA} (MODIS and Landsat) for windows where MODIS and Landsat f_{SCA} agree to within 10% ($|\Delta f_{SCA}| < 0.1$). Mean F-measure from random model ensembles ($\delta=0.1$) is also plotted against f_{SCA} with errorbars of $\pm 2\sigma$. Validation subset b and c are shown at left and right, respectively.

For a point plotting above $\mu F_{random} + \sigma F_{random}$, we are approximately 68% confident that the model is performing better than a random one. Similarly, for points plotting above $\mu F_{random} + 2 \cdot \sigma F_{random}$, we are 95% confident the model is outperforming a random one. Table 2 summarizes the fraction of downscaled scenes that satisfy these criteria. Provided in Figure 14 is an integrative schematic diagram for the overall downscaling routine, from pre-processing to validation.
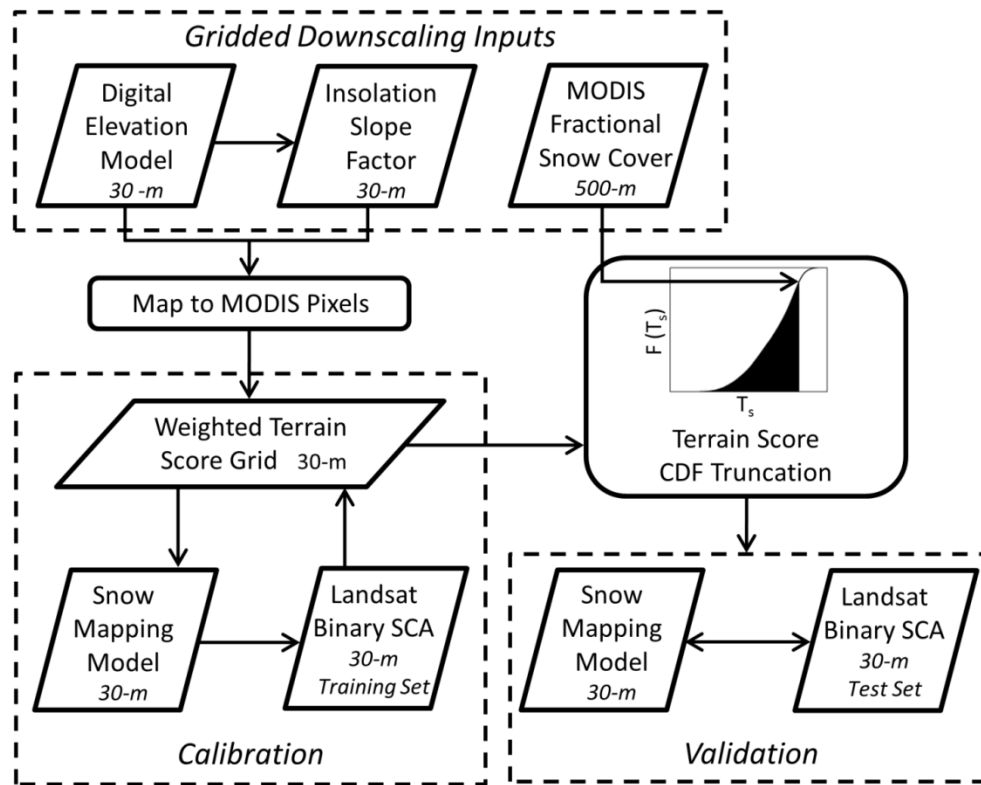
Figure 14. **Flow chart schematic outlining the fractional snow cover downscaling routine.**

Overall, the model more accurately downscales in subset validation region *b*. However, it is possible that this is a result of less agreement between Landsat and MODIS over region *c* (disregarding instances of 100% f_{SCA}) as is depicted by the sheer

fewer number of points in this region. Many occurrences of f_{SCA} between 0.8 and 0.9 are observed in both subset regions and, on the whole, most downscaling model F-measures

Table 2. **Fraction of downscaled windows ($|\Delta f_{SCA}| < 0.1$) in each subset region with F-measures exceeding the normal range of variability in those of random model ensembles (δ=0.1). Exceedance is shown for Landsat and MODIS.**

f_{SCA}	Variability	Exceedance Fraction	
Platform	Range	Subset b	Subset c
Landsat	$\mu F_{random} + \sigma F_{random}$	0.8122	0.8058
	$\mu F_{random} + 2 \cdot \sigma F_{random}$	0.7017	0.6325
MODIS	$\mu F_{random} + \sigma F_{random}$	0.7776	0.8320
	$\mu F_{random} + 2 \cdot \sigma F_{random}$	0.6823	0.6719

plot above the μF_{random} lines in Figure 13, indicating that the model is, at the very least, moving snow-covered pixels in the correct direction. However, there are points, especially at lower snow cover fractions, where the model performance exceeds randomness, yet still suffers a qualitatively low F-measure, meaning there are many type I and/or type II errors still occurring, albeit less than if the model were not tuned to terrain indices. Overall, the mean F-measure is higher over region c than for region b. However, in region c f_{SCA} varies mostly between 0.65 and 0.90, where F-measures must be correspondingly high to outperform a random assignment of snow cover.

2.4.3   Ideal Simulation Results

We also execute a validation simulation under circumstances of "ideal" fractional snow cover observations. That is, MODIS observations of f_{SCA} are substituted for the corresponding f_{SCA} values derived from Landsat over the MODIS footprint. In this fashion, the model is given maximum opportunity to downscale f_{SCA} windows containing

the observed "true" amount of snow-covered area since $\Delta f_{SCA} = 0$ everywhere in the domain. We examine the results of the downscaling model using the same methods outlined in Section 2.4.2. An updated ensemble of random models is generated with $\delta = 0$ to represent perfect snow cover observations. From this, we produce a new distribution of F-measures that is narrower than one resulting from a non-zero choice for δ. Figure 15 shows the F-measure as a function of fSCA and Table 3 provides the fraction of windows satisfying the criteria for outperforming random binary assignment outlined in the previous section. In these ideal circumstances, the downscaling model appears to perform better over subset region c than b.
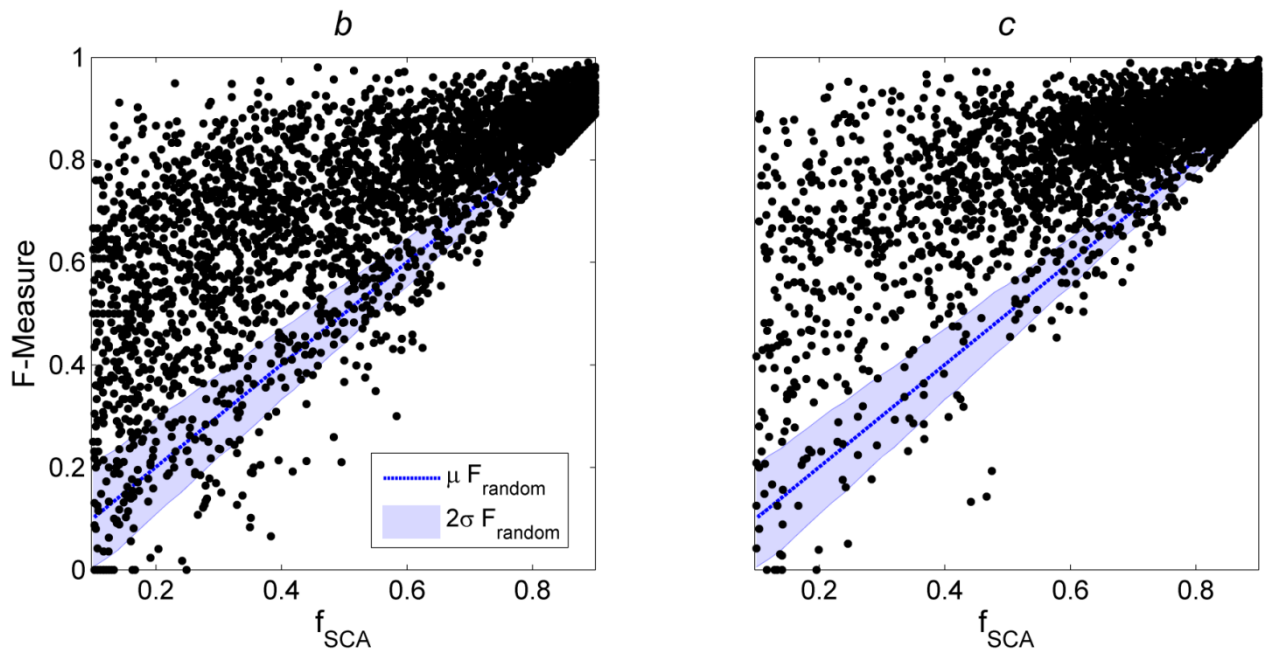
Figure 15. Modeled F-measure as a function of "ideal" f_{SCA} for synthetic windows where MODIS is adjusted to equal Landsat. Mean F-measure from random model ensembles ($\delta=0.0$) is also plotted against f_{SCA} with errorbars of $^{+}_{-}2\sigma$. Validation subset b and c are shown at left and right, respectively.

It should be noted that region c contains many windows with Landsat-observed f_{SCA} between 0.9 and 1.0 ($n = 10,115$) in comparison to region b ($n = 5,111$). Thus, these would be excluded from the evaluation leading to less windows for validation in region c ($n = 2,992$) than in region b ($n = 3,333$). Of the windows in the evaluation range, region c has a higher mean F-measure across its domain than b. The mean F values for MODIS and ideal (Landsat) snow cover fraction evaluation are given in Table 4.

An additional simulation is performed across subset a for the purpose of visualization. Figure 16 demonstrates the downscaling process from both Landsat and MODIS-derived f_{SCA}, along with the Landsat observation grid and an absolute difference grid to illustrate the disparity in snow cover fraction between the two platforms.

Table 3. **Fraction of downscaled windows with ideal snow fraction ($\Delta f_{SCA} = 0$) in each subset region with F-measures exceeding the normal range of variability in those of random model ensembles ($\delta=0.0$).**

Standard	Exceedance Fraction	
Deviations	Subset b	Subset c
$1\,\sigma$	0.8491	0.9011
$2\,\sigma$	0.8101	0.8723

Table 4. **Mean F-measures across regions b and c when downscaling MODIS and ideal (Landsat aggregate) f_{SCA} grids.**

f_{SCA}	Mean F-measure (F_μ)	
Platform	Subset b	Subset c
MODIS	0.7313	0.8372
Ideal	0.7232	0.8182
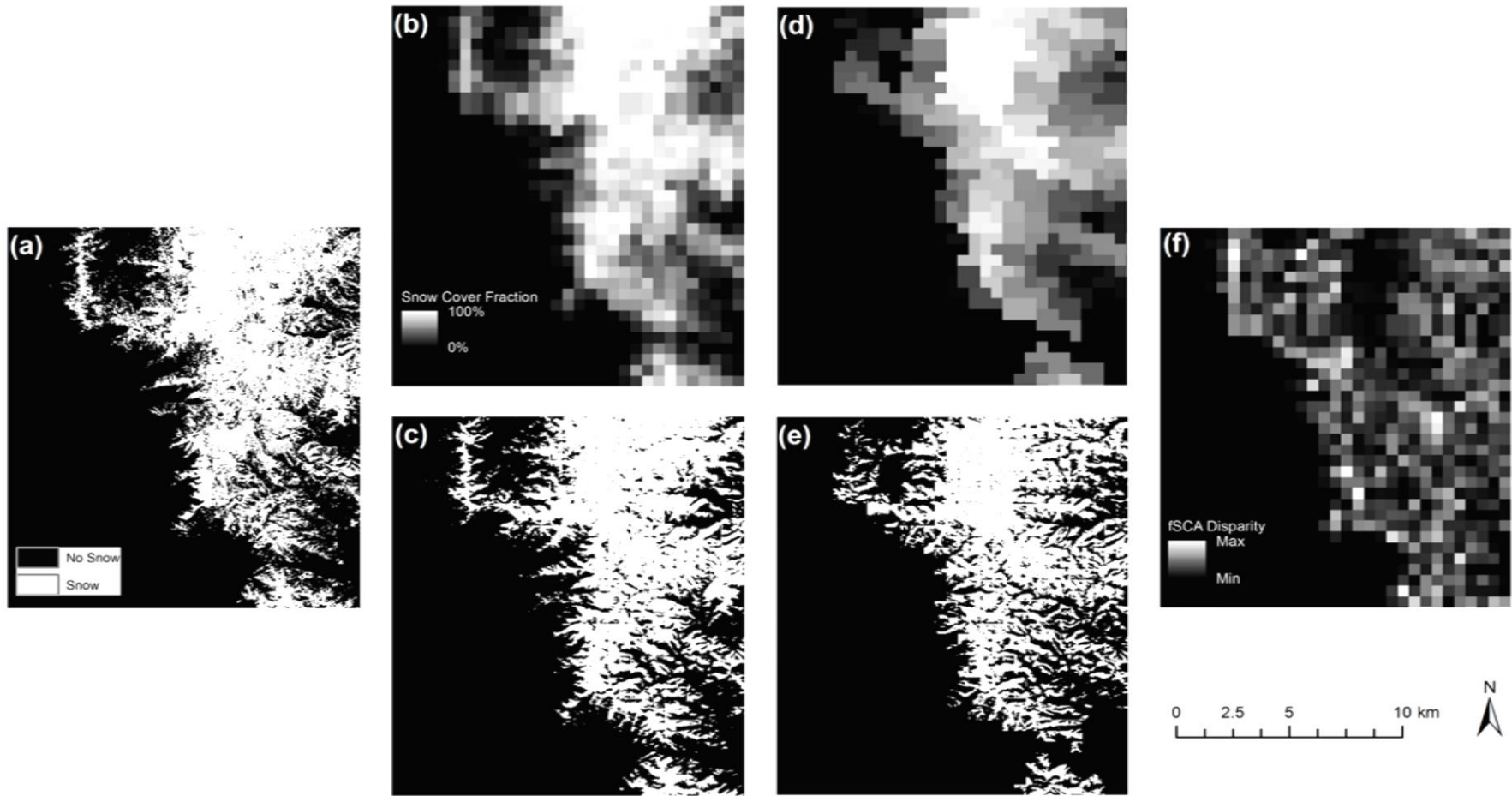
Figure 16. Downscaling visualization over region *a* displaying (a) Landsat observed binary snow cover, (b) "ideal" f_{SCA} as 500 m aggregate from landsat, (c) downscaled f_{SCA} from previous, (d) MOD10A1 500 m f_{SCA}, (e) downscaled f_{SCA} from previous, and (f) absolute difference grid between Landsat and MODIS, normalized to unity.
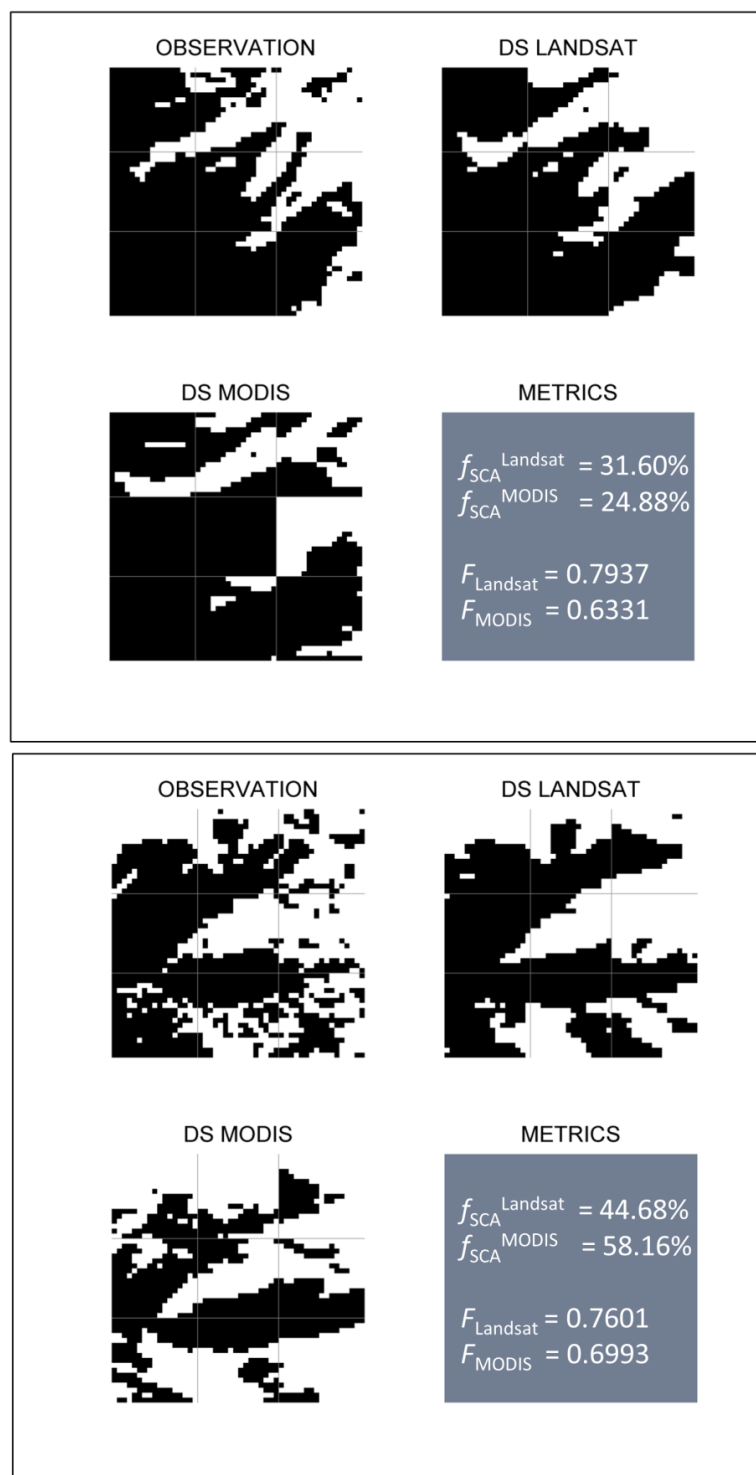
Figure 17. **Hillslope-scale downscaling visualization for two arbitrary subsets within region *a*. Each subset represents a 1500 m window (9 MODIS cells) and shows Landsat-derived observed snow cover, downscaled (DS) Landsat aggregate f_{SCA}, downscaled MODIS f_{SCA} and performance metrics for the 1500 m window.**

2.5   Discussion

The developed downscaling model performs with a certain level of skill for all subsets, requiring calibration of only one empirical parameter. However, locations exist where *F*-measure plots within, or below, a range of *F*-measures that can be achieved through purely random assignment of snow-covered locations. Even those downscaled 500 m pixels that exceed $\mu F_{random} + 2 \cdot \sigma F_{random}$ do not always reveal a dramatic improvement from random. The fraction of pixels with *F*-measures exceeding this range is, however, promising, especially across subset region *c*. This region also exhibited the highest mean *F*-measure, performing even better with input MOD10A1 f_{SCA} than with the ideal snow fraction. This is likely attributable to a general over-prediction of snow cover by MODIS in comparison to Landsat during the validation date and a distribution of f_{SCA} skewed toward higher values, which, by default, results in higher values of *F*-measure.

Ancillary information we are not currently including in the downscaling model may provide a source of improvement to the downscaling approach. Further analysis is necessary in order to gain insight into physiographic characteristics of terrain within MODIS windows where the model is failing (or succeeding) consistently. For instance, since we do not account for a forest canopy, we may be assigning snow-free states to areas where a forest canopy impedes a great deal of insolation and obscures existing snow cover. Forest canopy is also a potential reason for the f_{SCA} offset between MODIS and Landsat. For example, Raleigh et al. (2013) found that f_{SCA} derived from the MODSCAG model consistently under-predicted the observed snow fraction (quantified via temperature sensor networks) in a study plot with high canopy fraction (i.e., 79%), even when the remotely-sensed f_{SCA} value was statically corrected for the canopy cover.

Another parameter worthy of consideration is wind redistribution. In some regions, differential ablation patterns are affected directly by redistribution from wind during initial accumulation rather than by spatially varying energy inputs (Anderton et al., 2004). With knowledge of time-series wind vectors or seasonal tendencies, terrain-based indices can be generated in order to predict areas prone to drifting and general redistribution during the accumulation and settling of snow fall. Winstral et al. (2002) showed that a snow depth regression tree model based on elevation, solar radiation, and slope was substantially improved by the addition of a computationally-efficient wind redistribution predictor variable. Using this parameter with a physically-based, distributed snow model, improvements were made to the simulated distribution of snow cover, snow drifts, and melt within RCEW (Winstral and Marks, 2002). RCEW is located within validation subset region *b*, which will facilitate future efforts to include such information into the downscaling model.

Given the above considerations, it is important to stress the applicability of the algorithm in the region across which it is calibrated. The model will likely not perform as well in regions where variables other than insolation and elevation are known to dominate snow cover distribution. Furthermore, the algorithm as implemented requires a degree of balance between forces that act to drive and resist SCA spatial distribution throughout the season. Thus, it is important to note that employment of this model, or a similar one, in areas outside the given study region will require, at the very least, unique calibration to the chosen indices and potentially increased model complexity.

Future work may also employ spectral mixture analysis snow cover products (Rosenthal and Dozier, 1996; Painter et al., 2009) in order to perform similar experiments

using products that have been suggested to have a higher accuracy (particularly during the ablation phase with which we are most concerned) in reproducing the snow cover distribution. In applying the model developed here to satellite retrievals using spectral mixing models, care must be taken to ensure that the 30 m resolution binary snow cover map is produced using techniques similar to those used to estimate the 500 m resolution fSCA (i.e., Painter et al., 2003).

The linear method used here to combine the physiographic index variables (insolation and elevation) is relatively straightforward. The method makes a speculative assumption that the variables' relative contributions to snow cover are dependent on a single-parameter, linear equation model. It is worth noting that more complex approaches exist for multivariate data characterization. A method to be explored in future work is the use of copulas for blending multiple variable indices. Copulas are efficient probabilistic tools used to describe the dependence structure of joint multivariate random variable distributions through examination of the underlying univariate marginal distributions (Schwarzlander, 2011). This method is frequently applied in financial risk analysis and has been used increasingly in the field of hydrology in the past several years (Schölzel and Friederichs, 2008). Such an approach may offer additional insight into the relationship between physiographic parameters and snow cover.

Another point of discussion is that of the disparity in f_{SCA} between Landsat and MODIS. Although the difference histograms in Figure 12 are approximately normally distributed, the tails of the distributions retain many cases of disagreement between the two snow cover remote sensing platforms. Some of these disparities may be, in part, due to physiographic differences between the study area and the regions in which the

MOD10A1 product was calibrated (i.e., Alaska, Siberia and Canada; Salomonson and Appel, 2004). A future approach might be wise to consider using raw 500 m MODIS reflectance data (MOD09GA) to compute NDSI and calibrate this signal to the Landsat observations for the area of interest. This would produce the presumed result of narrower difference histograms between the platforms, thus improving validation results and overall reliability of the model.

The described downscaling routine could potentially be used in conjunction with current snow water equivalent reconstruction techniques that account for full energy balance (e.g., Cline et al., 1998; Durand et al., 2008; Molotch, 2009). To date, these models typically simulate energy fluxes and basin physiography at the scale of the remote sensing observation. Under this framework, given proper computational resources, full energy balance could be computed at the scale of a DEM. Then, with a MODIS fractional snow cover observation, these fluxes could be normalized and snow could be assigned to those pixels receiving the least flux on daily or cumulative scales. It is also hypothesized that snow cover could be estimated as a fraction within each high-resolution DEM pixel by assigning a probability distribution across a MODIS pixel rather than explicit sub-grid binary states that sum to an observed f_{SCA} value. SWE reconstruction at this scale might provide more insight into the true distribution of this hydrologic state as it varies across topographically complex terrain under a retrospective framework subject to intensive validation. This information could prove useful as a way forward in predicting real-time and forecasted runoff response and water availability.

2.6   Conclusion

We describe here a computationally efficient model to downscale fractional snow-covered area (f_{SCA}) data from MODIS to a higher-resolution, spatially explicit binary grid based on physiographic indices. Parameterizations for elevation and insolation are combined to yield a terrain score that is used to assign binary snow cover on a 30 m grid with information about fractional snow cover on a 500 m grid. Using Landsat binary snow cover maps derived using an NDSI threshold, the model is calibrated to 13 Landsat binary snow cover scenes for one domain subset and validated against a Landsat scene and in two domain subsets not used in calibration. Calibration results depict a general stability in weight parameters over varying times of the snow season and degrees of snow cover. Results from validation show that model performance, as assessed via the *F*-measure, tends to outperform ensembles of randomly generated snow cover maps over a relatively large range of f_{SCA}. The developed model could assist hydrologic modeling in restricted areas by providing daily, high resolution, if imperfect, constraints on the distribution of snow in mountainous areas.

CHAPTER THREE: TOWARDS DOWNSCALING COARSELY-MODELED

SNOWMELT IN COMPLEX TERRAIN

3.1   Introduction

Snow and ice constitute substantial components of the world's hydrologic cycle.

Melt from glaciers and seasonally snow-covered regions is of critical importance,

delivering water to more than one-sixth of the world's population (Barnett et al., 2005).

In the western United States, melt water from mountain snowpack delivers an estimated

75% of annual runoff to major streams and rivers in the region (Palmer, 1988), yielding

hydrologic implications in matters ranging from hydroelectric power to municipal water

supply systems. Melting snow is also intrinsically linked to soil moisture, the knowledge

of which is vital to the prediction of catchment response and coupling of the land-

atmosphere system (Chen et al., 2001; Bales et al., 2011). Furthermore, the forest

ecosystem carbon cycle demonstrates dependence on snow distribution throughout the

mountain environment, due to both water availability and the effect of snow depth on soil

temperature (Schimel et al., 2002).

Shifts in the Earth's climate due to anthropogenic forcing have prompted many

hydrologic impacts assessment studies. A warming trend throughout the western United

States has resulted in an earlier average onset of snowmelt and stream runoff (Gleick,

1987; Aguado et al., 1992; Cayan et al., 2001). This observed trend presents major

challenges to water managers and montane ecosystems (Stewart et al., 2004). As a result

of these emerging trends, hydrologic forecasting skill (e.g., streamflow) is likely to deteriorate as historical empirical relationships become decreasingly representative of present conditions in a warming climate (Milly et al., 2008; Dozier, 2011). These factors have prompted increased interest in understanding the processes of snow accumulation and melt. For accurate prediction of hydrologic variables like snow water equivalent (SWE), snowmelt, and stream runoff under current or future conditions, further research is necessary to improve the ability to realize this objective.

Snow process are known to occur variably over small scales, the significance of which is acutely appreciated by snow hydrologists (e.g., Kirnbauer and Blöschl, 1994; Luce et al., 1998; Blöschl, 1999). While *in situ* point measurements of snow depth and SWE can provide essential information about snowpack hydrology, these estimates do not necessarily characterize the overall spatial mean conditions (Molotch and Bales, 2005; Li et al., 2012). Simulation models are employed as a way to estimate snow processes, often used in conjunction with observational data. Some studies have made use of regression tree models to produce gridded estimates of SWE from field survey data and predictor variables like wind, elevation, and solar radiation (Elder et al., 1998; Winstral et al., 2002). Others have used temperature-index models to predict SWE and melt, assuming empirical "degree-day" relationships between maximum daily air temperatures and the rates of snowmelt (Hock, 2003; references therein). Others have used models based completely on physical parameters and processes, computing energy balance equations and estimating snowmelt as a residual term (e.g., Tarboton and Luce, 1996; Marks et al., 1999; Lehning et al., 2006). Some studies have made use of models in conjunction with satellite remote sensing snow-covered area (SCA) data in order to back-

calculate SWE at the basin scale, offering robust estimates of the amount of water stored as a snow around the time of maximum accumulation. Martinec and Rango (1981) first demonstrated this technique using the temperature-index, degree-day approach to reconstruct SWE in the Dinwoody Basin of Wyoming. Others have applied the reconstruction technique using physically-based, energy balance models, demonstrating favorable results in comparison with intensive field campaigns (Cline et al., 1998; Durand et al., 2008; Molotch, 2009). Such analyses can provide great information about the distribution of snow, but work remains in learning to aptly employ this knowledge in real-time or forward modeling.

This chapter describes a study that uses snowmelt output from an existing, relatively coarse-scale mass and energy balance snow model that operates at near real-time. The goal in this work lies in estimating the spatiotemporal variability within this model's grid cells. This variability is estimated through a semi-empirical approach, utilizing satellite remote sensing fractional snow-covered area (f_{SCA}) data, solar radiation indices, vegetation canopy attenuation adjustments, and snow surface albedo parameters. By downscaling the modeled melt to a higher resolution, it is proposed that other basin states and fluxes (e.g., soil moisture and streamflow) could be estimated with increased predictive skill.

The method is employed across a modeling domain containing an experimental catchment, described in Section 2. The datasets employed are introduced in Section 3 along with a brief discussion of relevant theory and pre-processing procedures. Then, an outline of the overall downscaling routine is presented in Section 4. Results of

downscaling are compared with available field data in Section 5 and a discussion and way forward are presented in Section 6.

3.2   Study Area

This study takes place over Dry Creek Experimental Watershed (DCEW), a 27 km^2 catchment in the semi-arid foothills of the Boise Front in southwestern Idaho (Stieglitz et al., 2003; McNamara et al., 2005; Tyler et al., 2008; Kelleners et al., 2010; Smith et al., 2011). The terrain is moderately complex, characterized by multiple ridges and hillslopes draining ephemeral tributary streams into Dry Creek. Another major stream, Shingle Creek, drains the southeastern portion of DCEW and makes confluence with the main stem of Dry Creek in the southwestern quadrant of the watershed. Elevations in the watershed range from approximately 900 to 2100 m above sea level (Figure 18). Vegetation ranges from sage brush on the lower slopes to chaparral, spruce, fir, and pine in the upper reaches (McNamara et al., 2005). The watershed exhibits pronounced orographic effects on temperature and precipitation with the local climate characterized by hot, dry summers and cold, wet winters (Smith et al., 2011). DCEW is instrumented with seven stream gauging stations and five meteorological stations. The latter stations serve to capture the variability of hydrologic properties across spatial, landscape, and elevation gradients throughout in the watershed. A National Resources Conservation Service Snowpack Telemetry (SNOTEL) site is also located just north of the watershed boundary near Bogus Basin. Information about these stations is contained in Table 5. Soils are typically less than 2 m thick and composed of gravelly loams and sands, with bedrock of late Cretaceous granodiorite of the Idaho Batholith Atlanta Lobe (McNamara et al., 2005; Gribb et al., 2009; Smith et al., 2011).
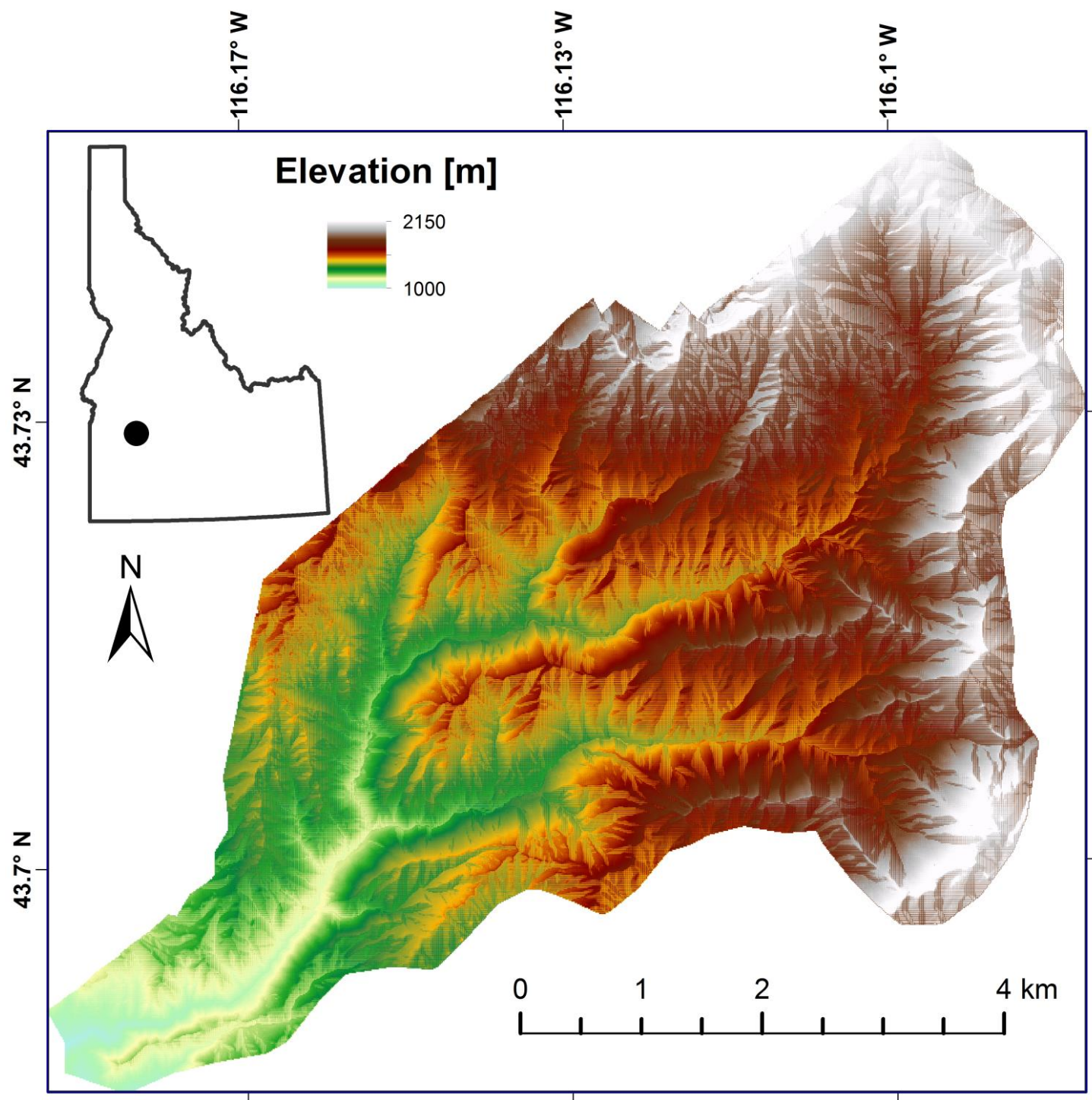
Figure 18. **Digital elevation model for Dry Creek Experimental Watershed with southwestern Idaho location inset. This 10 m product was resampled from a 1 m LiDAR terrain model. The grid serves as the modeling domain and higher-resolution mesh onto which snowmelt is downscaled.**

Table 5.   **DCEW meteorological station information.**

Site Name	Abbreviation	Data Begin Date	Elevation (m)
Lower Weather	LW	1999	1151
Treeline Weather	TLW	1999	1610
Shingle Creek Ridge	SCR	2010	1720
Lower Deer Point	LDP	2007	1850
Bogus SNOTEL	BS	1999	1932
Bogus Ridge	BRW	2011	2114

3.3   Datasets

The goal in this study is to approximate the spatiotemporal variability within coarse-resolution modeled snowmelt grid cells. This variability is estimated through a semi-empirical approach utilizing solar radiation indices, vegetation canopy attenuation adjustments, snow surface albedo parameters, and satellite remote sensing fractional snow-covered area (f_{SCA}) data. This section provides brief descriptions of the existing modeled snowmelt product and the ancillary datasets and relevant background theory used to predict the downscaling parameters.

3.3.1   SNOw Data Assimilation System

The SNOw Data Assimilation System (SNODAS) is a snow simulation modeling and data assimilation framework developed by the NOAA National Weather Service's (NWS) National Operational Hydrologic Remote Sensing Center (NOHRSC) to provide optimal estimates of widespread snow cover and other variables to aid in hydrologic modeling (Barrett, 2003). Integrated daily data output from this product is archived by the National Snow and Ice Data Center (NSIDC) at the University of Colorado, Boulder. These data include SWE, snow depth, basal snowmelt runoff, sublimation from the

snowpack and from blowing snow, snow density, solid precipitation, and liquid precipitation. SNODAS covers the conterminous United Sates, providing estimates of snow process variables at 30 arc-second resolution. Numerical weather prediction (NWP) model output is downscaled and used as input to a physically-based, mass and energy balance snow model, dubbed the NOHRSC Snow Model (NSM). From its inception, SNODAS was forced with Rapid Update Cycle (RUC) 2 NWP output. This model was replaced by the Rapid Refresh (RAP) NWP beginning in May of 2012. This new NWP model, based on the Weather Research and Forecasting model (Michalakes et al., 1998), applies its own assimilation routines before downscaled output is produced for SNODAS ingestion (NOHRSC, 2012).

SNODAS builds upon the concept that available observational ground-based snow data are not dense enough to produce runoff forecasts in (near) real-time, nor is a stand-alone model always accurate at this spatial extent and resolution. Hence, SNODAS incorporates all available data, utilizing assimilation procedures to integrate ground and airborne observations into the framework (Carroll et al., 2001). Observed data include Snowpack Telemetry (SNOTEL) network stations maintained by the National Resources Conservation Service (NRCS) of the US Department of Agriculture. Every day, analysts at NOHRSC decide whether or not it is necessary and useful to assimilate observations into the model. Snow water is often removed from or added to the snowpack in certain regions in order to nudge the modeled states toward observed SWE (Barrett, 2003). An overview of current assimilation updates are often presented at the NOHRSC website (NOHRSC, 2012).

For this study, we obtain daily SNODAS snowmelt runoff (Figure 19) and SWE (Figure 20) data for the study area for the time period from 1 January 2010 to 30 June 2010. Data are obtained in Network Common Data Form (NetCDF), a self-describing, machine-independent data creation, access, and sharing format that stores scientific datasets in array form (Rew et al., 2011).
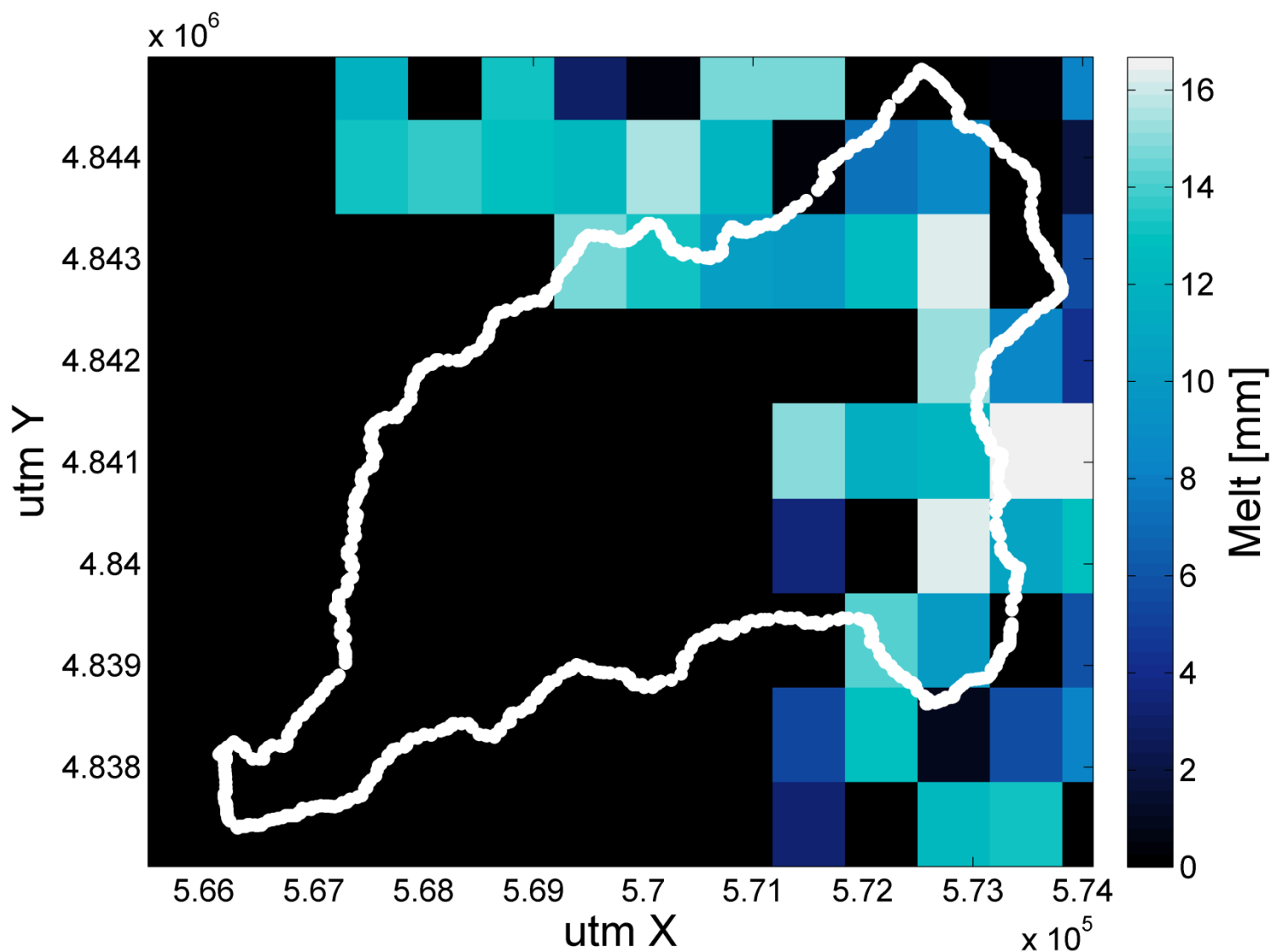
Figure 19. **Snowmelt estimated by SNODAS on 18 March 2010. DCEW delineation boundary shown in white.**
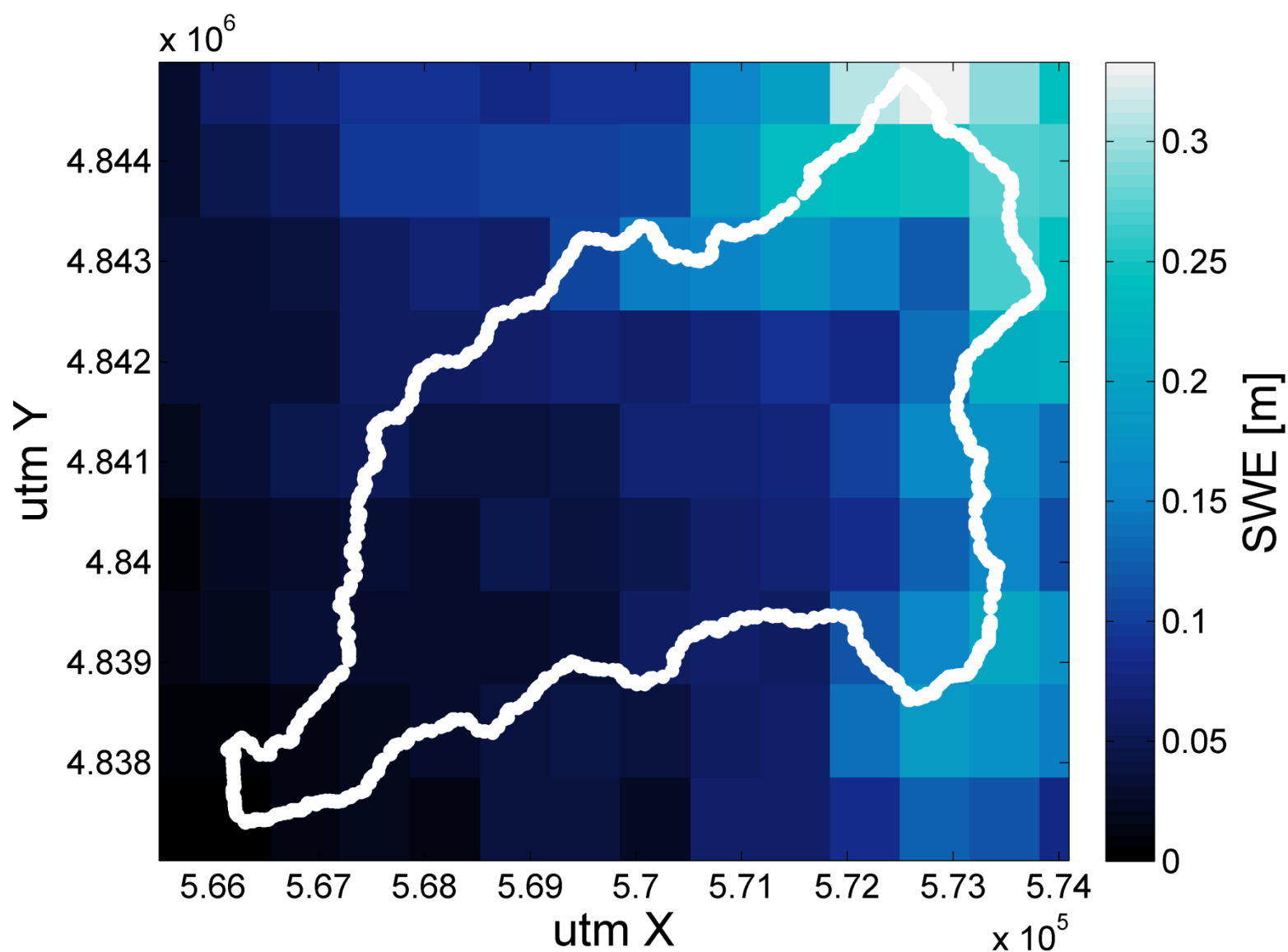
Figure 20. **Snow water equivalent estimated by SNODAS on 9 February 2010. DCEW delineation boundary shown in white.**

3.3.2   Remotely Sensed Snow Cover Data

Remotely sensed f_{SCA} data are obtained from the Moderate Resolution Imaging Spectroradiometer (MODIS) instrument. We use MOD10A1 Level 3 Version 5 data (Hall et al., 2006), obtained in hierarchical data format (HDF) as described in Chapter 2 of this document. Further details on this product's formulation are described in Section 2.2.1.

MODIS f_{SCA} images are obtained daily over a region slightly larger than our study domain such that they can be cropped accordingly. Though the product has daily retrieval, some of the images are obscured by clouds or poor viewing geometry. Thus, we employ a temporal interpolation scheme by which we estimate snow cover during the times when MODIS did not detect a quality image. The details of this temporal smoothing are outlined in the methods section of this chapter. It should be noted that the MOD10A1 fractional snow cover product has recently been shown to under-perform in some regions, especially during the melting season (Rittger et al., 2012). A more recent f_{SCA} product, the MODIS Snow-Covered Area and Grain size (MODSCAG) model, utilizes robust spectral mixture analysis with MODIS reflectance data to estimate snow cover fraction and has demonstrated promising results in validation (Painter et al., 2009; Rittger et al., 2012). Future work might explore the utility of other snow remote sensing products in conjunction with the downscaling routine.

3.3.3   Digital Elevation Data

This study employs a LiDAR digital elevation model (DEM) over the study area (referenced in Section 3.2, Figure 18) with a native resolution of 1 m, aggregated to 10 m. The data were acquired over DCEW during a 2009 overflight, obtaining a mean relative accuracy of 0.069 m with a standard deviation of 0.075 m per flight line (Watershed Sciences, 2009). Processed data can be accessed at:

http://cloud.insideidaho.org/ArcGIS/rest/services/elevation/2007_dryCreekWatershed/MapServer

including features such as roughness, slope, aspect, hillshades, et cetera. Slope and aspect data from this source are also used in this particular study in order to provide independent variable information to a solar radiation algorithm.

The 1 m bare earth DEM product is coarsened to 10 m to aid in parsimony during the downscaling and solar radiation calculations. The aggregate product is formed through resampling, moving a 10 m window across the entire 1 m grid and assigning each coarse pixel the mean of the high-resolution pixels contained therein. Slope and aspect grids are coarsened to 10 m resolution in the same fashion.

3.3.4   Solar Radiation Data

Short-wave (solar) radiation, or insolation, is a very important part of the energy fluxes acting on a melting snowpack. This radiation generally falls in a band of the electromagnetic spectrum from 0.2 to 2.2 µm with a maximum intensity at 0.47 µm (Gray and Male, 1981). Direct short-wave energy input to the earth's surface is highly variable in space, especially in the complex terrain of mountainous areas where slopes, aspects, and elevations exhibit substantial variability. Cloud cover and vegetation also provide controls over short-wave radiation. This study makes adjustments to the incoming solar radiation due to forest canopy. However, no corrections are assumed for cloud cover. Since the SNODAS modeled melt has already been computed as the result of energy balance calculations, only the relative variation in direct insolation (due to hillslopes and forest canopy) need be computed. This postulation requires the assumption that cloud cover is homogenous across each SNODAS grid pixel.

Solar radiation data are computed using the algorithm presented by Swift (1976) with minor modifications. As noted above, the actual magnitude of solar radiation need not be computed in the downscaling routine. Rather, a ratio is computed of potential insolation on a sloping pixel surface to that of a horizontal one. That is

$$f_{sl} = \frac{R_{slope}}{R_{horiz}} \qquad (1)$$

where R_{slope} and R_{horiz} are pixel-scale potential insolation on the local slope and

horizontal plane, respectively, and f_{sl} is the normalized term referred to as the slope

factor. The slope factor is calculated at every pixel in the digital elevation model used as

the downscaling mesh. A 10 m slope factor grid is produced for every day of the year.

Figure 21 illustrates the slope factor across DCEW for 18 March. Slope factor pixels with

higher (lower) values produce higher (lower) snowmelt estimates after the downscaling

routine is implemented. For more details of the solar radiation slope factor calculations

for potential insolation, refer to Appendix A.1.

3.3.5 Vegetation Land Cover Data

The presence of a forest canopy above a snowpack introduces significant

complications in model estimation of snow processes beneath this medium (Ellis and

Pomeroy, 2007; Storck et al., 2002). In this study, forest canopy density information is

used to attenuate incoming solar radiation and, thus, the resulting snowmelt downscaled

estimate. There is no correction assumed for canopy interception or long-wave radiation

emission. An attenuation model can be approximated by decreasing transmitted radiation

exponentially with increasing forest canopy density. This approach uses an equation

similar to Beer's Law to model the effect of an overlying canopy (Mahat and Tarboton,

2012). The transmittance through forest canopy is modeled as

$$\tau = \exp(-\frac{G}{\cos\theta_z} \cdot L \cdot FC) \qquad (2)$$
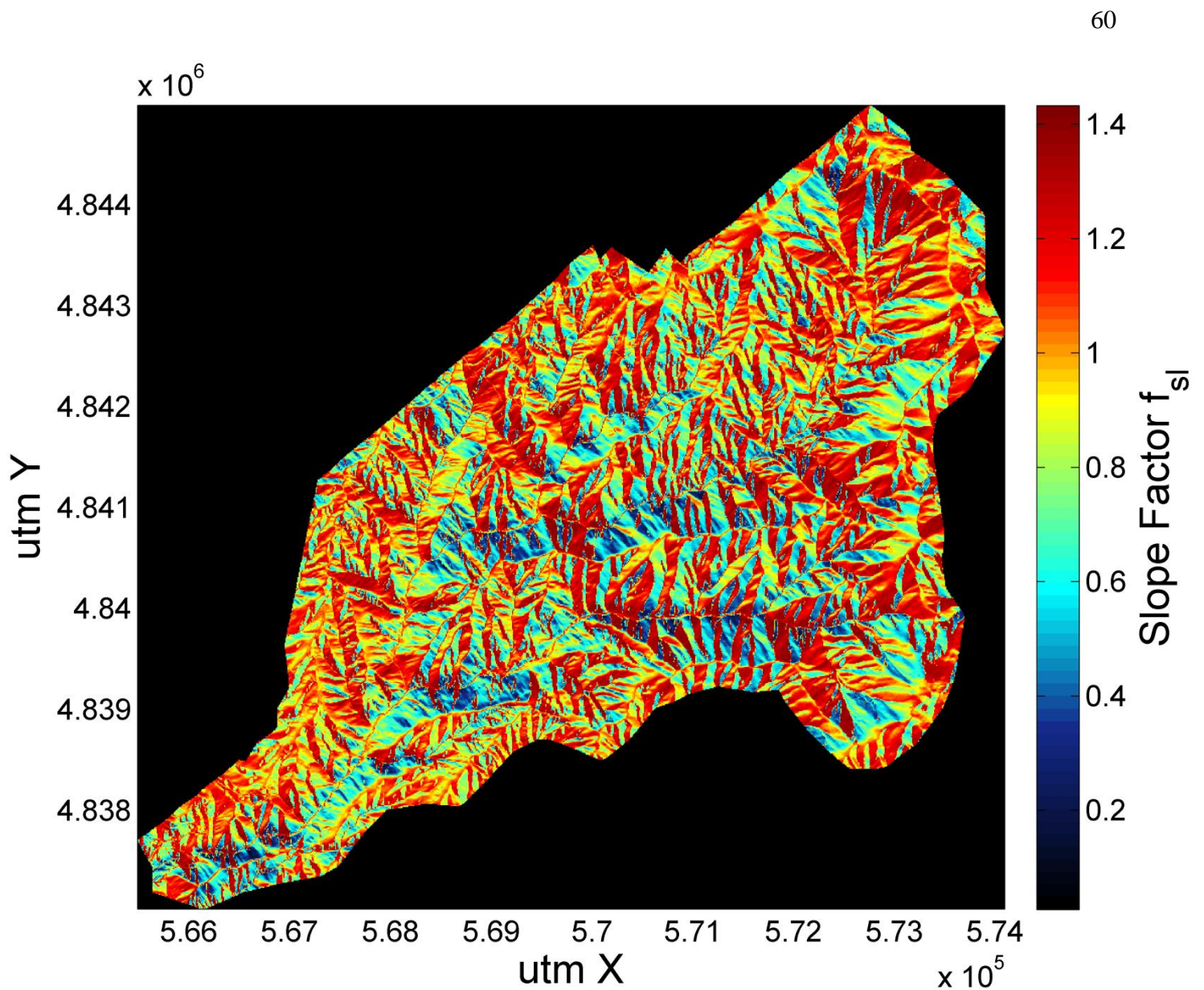
Figure 21. **Daily potential insolation slope factor (f_{sl}) computed across DCEW for 18 March.**

where G is leaf orientation factor, θ_z is solar zenith angle, L is leaf area index (LAI), FC is the forest canopy fraction [0,1], and τ is the resultant canopy transmittance. We assume $G = 0.5$ for isotropic leaf (needle) orientation and fix LAI at 6.0, a value suggested for coniferous forest cover (Dingman, 2002). Forest canopy fraction data are obtained from the Multi-Resolution Land Characteristics Consortium (MRLC) National Land Cover

Database (NLCD). This data is available for the conterminous United States at 30 m
spatial resolution, including the tree canopy percentage product. These canopy fraction
data were generated via regression trees based on 1 m training data (Homer et al., 2007).
A grid covering the DCEW (Figure 22) extent is acquired and resampled to 10 m
resolution via nearest-neighbor interpolation, essentially creating identical 3-by-3 10 m
cells within each 30 m window. This grid is then cropped to the extent of the DEM
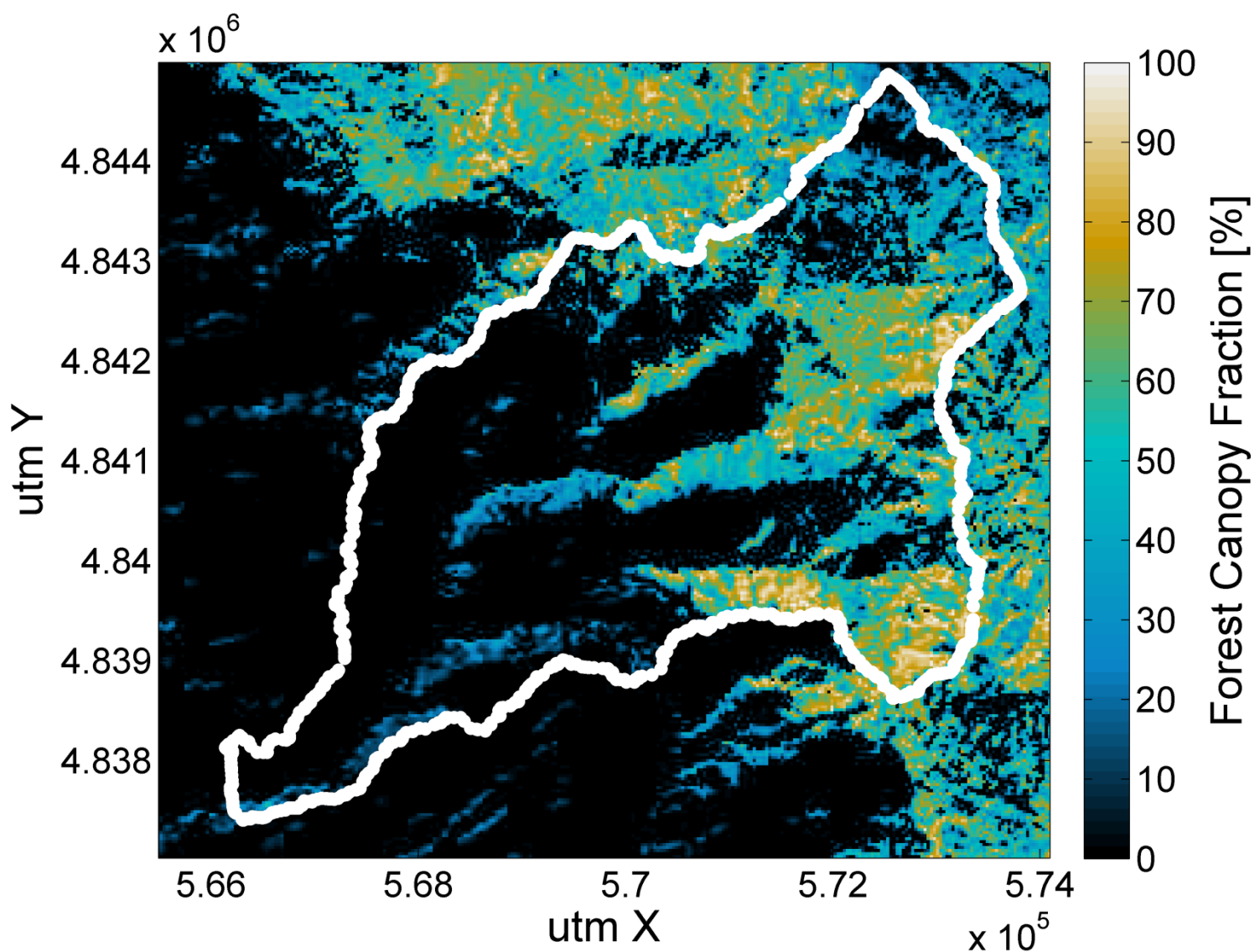
Figure 22. **NLCD forest canopy fraction over DCEW.**

previously described. For high canopy density areas in the downscaling domain, solar radiation transmittance is attenuated, decreasing the adjusted melt estimate. At a given point in the grid, the attenuation decreases as the season progresses and the sun moves more directly overhead (i.e., smaller solar zenith angle). This transmittance is illustrated by Figure 23.
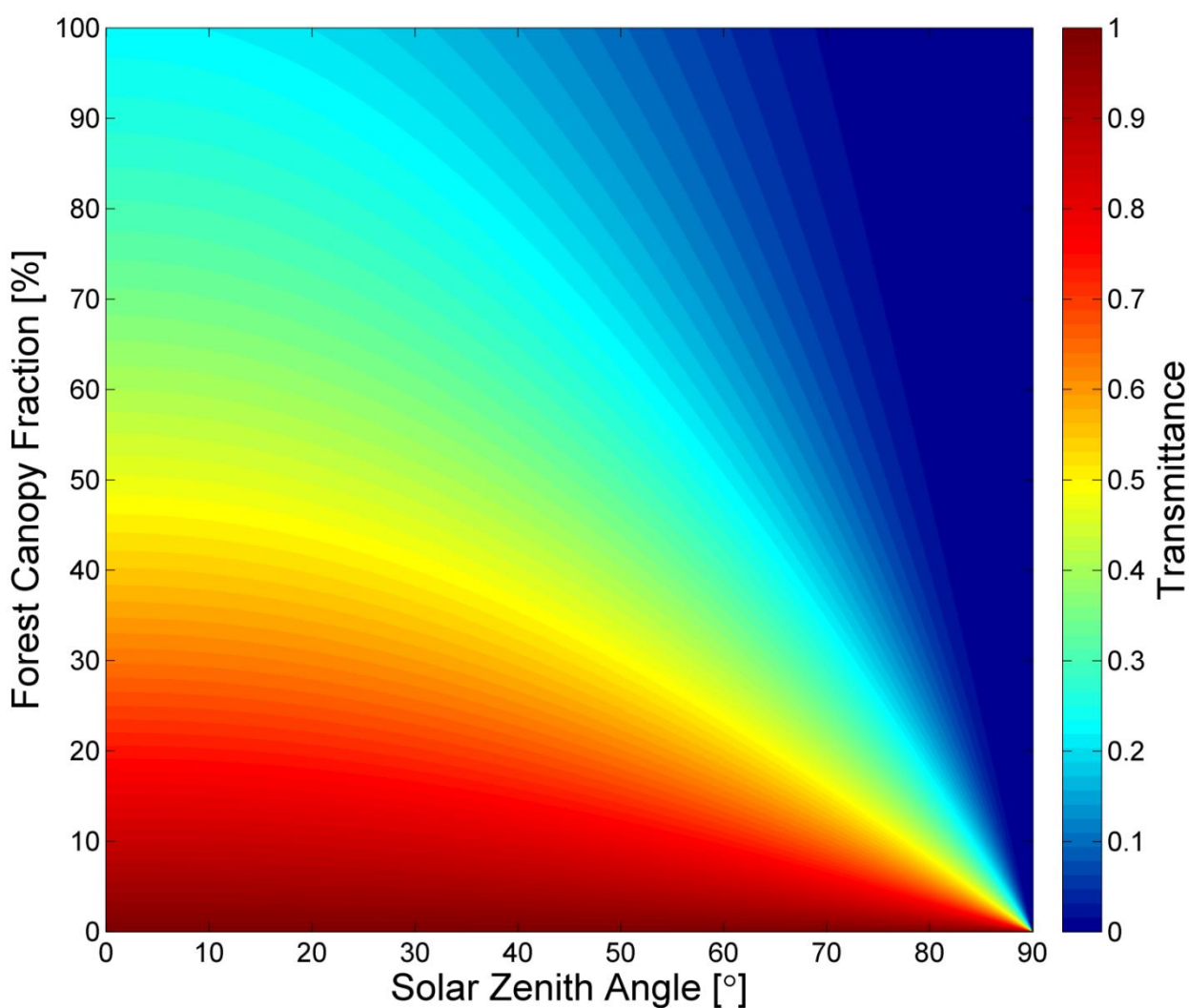
Figure 23.   Direct-beam solar radiation transmittance as a function of forest canopy fraction and solar zenith angle.

3.3.6   Snow Surface Albedo

The albedo of the snow surface is a critical component in the overall energy balance, exerting control on the rate of melt due to the reflective effect on incoming radiation (Wiscombe and Warren, 1981). Surface albedo is calculated as the ratio of outgoing to incoming irradiance. It terms of short-wave energy, it has the form

$$\alpha_A = \frac{S_o}{S_i} \tag{3}$$

where S_i and S_o are incoming and outgoing short-wave radiation, respectively, and α_A is the snow surface albedo term. We compute the net short-wave energy input as the sum

$$S_n = S_i - S_o. \tag{4}$$

Rearranging Eqn. 3 to $S_o = \alpha_A \cdot S_i$, we can re-write Eqn. 4 as a function that does not require an outgoing short-wave radiation estimate:

$$S_n = S_i - \alpha_A \cdot S_i \tag{5}$$

which rearranges to the simpler form

$$S_n = (1 - \alpha_A) \cdot S_i \tag{6}$$

where S_n is the net short-wave term.

Snow albedo can be estimated as a function of several variables, including snow grain size, solar zenith angle, snow depth, dust radiative forcing, and snow age. Debele et al. (2009) approximated albedo by a simple snow age decay function:

$$\alpha_A = 0.43 \cdot (1 + e^{-K_e \cdot t}) \tag{7}$$

where K_e is a decay parameter set to approximately 0.2 day^{-1} and t is days since new snow accumulation. In this study, we use SWE information from SNODAS to

approximate t to estimate the snow albedo. However, this only provides albedo values at

the spatial resolution of SNODAS. From a downscaling perspective, it is beneficial to

have albedo information at a higher resolution than the product we are attempting to

disaggregate. Therefore, remotely sensed snow albedo is also ingested into the model.

Similar to the areal snow cover data, we implement snow albedo observations from the

MODIS MOD10A1 albedo product. MOD10A1 snow surface albedo is available daily at

500 m spatial resolution. This product was validated over the Greenland Ice Sheet against

in situ ground-based observations and found to have an RMS error of 0.067 (Stroeve et

al., 2006). We merge the observed snow surface albedo from MODIS with the decay

estimates through a standard assimilation approach. More details of this assimilation can

be found in the methods section of this chapter.

3.3.7   Field Lysimeter Snowmelt Data

2010 field data from four lysimeters collecting snowmelt are used in this study for

comparison with downscaled model results. These lysimeters are installed at two

different meteorological station sites in DCEW, Treeline (TL) and Lower Deer Point

(LDP). At each of the two sites, two lysimeters are installed on opposing hillslopes facing

roughly north or south and denoted accordingly N or S. These instruments are part of a

larger study to improve understanding of lateral water flow through a snowpack. More

information on that phenomenon and details of the lysimeter construction are outlined in

Eiriksson (2012) and Eiriksson et al. (2013). General location data for the lysimeters is

presented in Table 6. It should be noted that the lysimeters at TL lie within one SNODAS

grid cell. The same is true for the LDP lysimeters. The information from these

instruments provides first-order confirmation data for the snowmelt downscaling routine.

Table 6.   **Snowmelt lysimeter location information.**

Lysimeter Site	Easting	Northing	Elevation (m)
TL South	569271	4842311	1608
TL North	569267	4842284	1611
LDP South	570663	4842968	1832
LDP North	570932	4843430	1830

3.4   Methods

The downscaling methodology presented in this chapter relies on the

aforementioned datasets. A point-by-point operation is performed at each pixel in the

modeling domain. This section describes the overall downscaling routine, with separate

treatment of the spatial and temporal facets. To begin, the pre-processing steps of snow

cover interpolation and surface albedo assimilation are described in detail.

3.4.1   MODIS Snow Cover Pre-Processing and Time-Interpolation

MOD10A1 f_{SCA} (and albedo) data are acquired over the study region and

reprojected from the native Sinusoidal grid into a UTM coordinate system using the

MODIS Reprojection Tool (MRT) from the NASA Land Processes Distributed Active

Archive Center (LP-DAAC). This tool can be downloaded from:

https://lpdaac.usgs.gov/tools/modis_reprojection_tool

The MRT is invoked via a series of system calls from a looping MATLAB script acting

to reproject (UTM 11N WGS-84) and crop all of the MODIS files over the date range of

interest. Appendix A.2 provides this script and the MRT parameter file used to specify

the settings for this process.

As described previously, many of the MODIS images are corrupted by cloud cover and thus do not offer reliable information about the snow cover fraction. During the time period of interest (1 January 2010 to 30 June 2010), an average of 69.22% of the pixels in the study domain were obscured by cloud cover. It is thus necessary to interpolate between the reliable observations to estimate the snow cover during the times when observations are not available. The process used here closely follows that of Dozier and Frew (2009) with some simplifications. Images are first filtered, assigning *not-a-number* (NaN) values to those pixels with values falling outside the reasonable range of f_{SCA} percentage values from 0 to 100%. Next, a smoothing spline is employed to approximate the f_{SCA} values over erroneous data points in the temporal dimension. The smoothing spline utilized is the MATLAB `csaps` function. This function minimizes the following equation (de Boor, 2007):

$$q \sum_{j=1}^{N} w_j \left[\hat{S}(t_j) - S(t_j) \right]^2 + (1-q) \int_{t_{min}}^{t_{max}} \zeta(t) \left(\frac{d^2 S}{dt^2} \right)^2 \tag{8}$$

where $\hat{S}(t)$ and $S(t)$ represent the estimated and true fractional snow-cover values, respectively. Values t_{max} and t_{min} are last and first dates of interest, respectively, and q is a smoothing parameter. $\zeta(t)$ is a piecewise constant weight function over t and w_j are scalar weights dictating the degree of penalty for modeled estimates' disagreement with observation. In this case, the smoothing parameter q is set to a constant of 0.6 and weights are set to 1. A more complex treatment is to vary q based on times between observations. Also, weights can be allowed to vary based on the satellite sensor viewing angle, assigning more confidence to those observations with lowest sensor zenith angles (Dozier and Frew, 2009). However, MOD10A1 data do not include viewing geometry

data and thus these considerations are ignored in this study. Figure 24 depicts the raw and smoothed data for six locations in the MODIS grid extent.

Once the snow cover data are smoothed in the temporal dimension, a conservative two-dimensional Gaussian low-pass filter is applied to each image in the data cube using the MATLAB `fspecial` function. The filter used is square (3-by-3), and rotationally
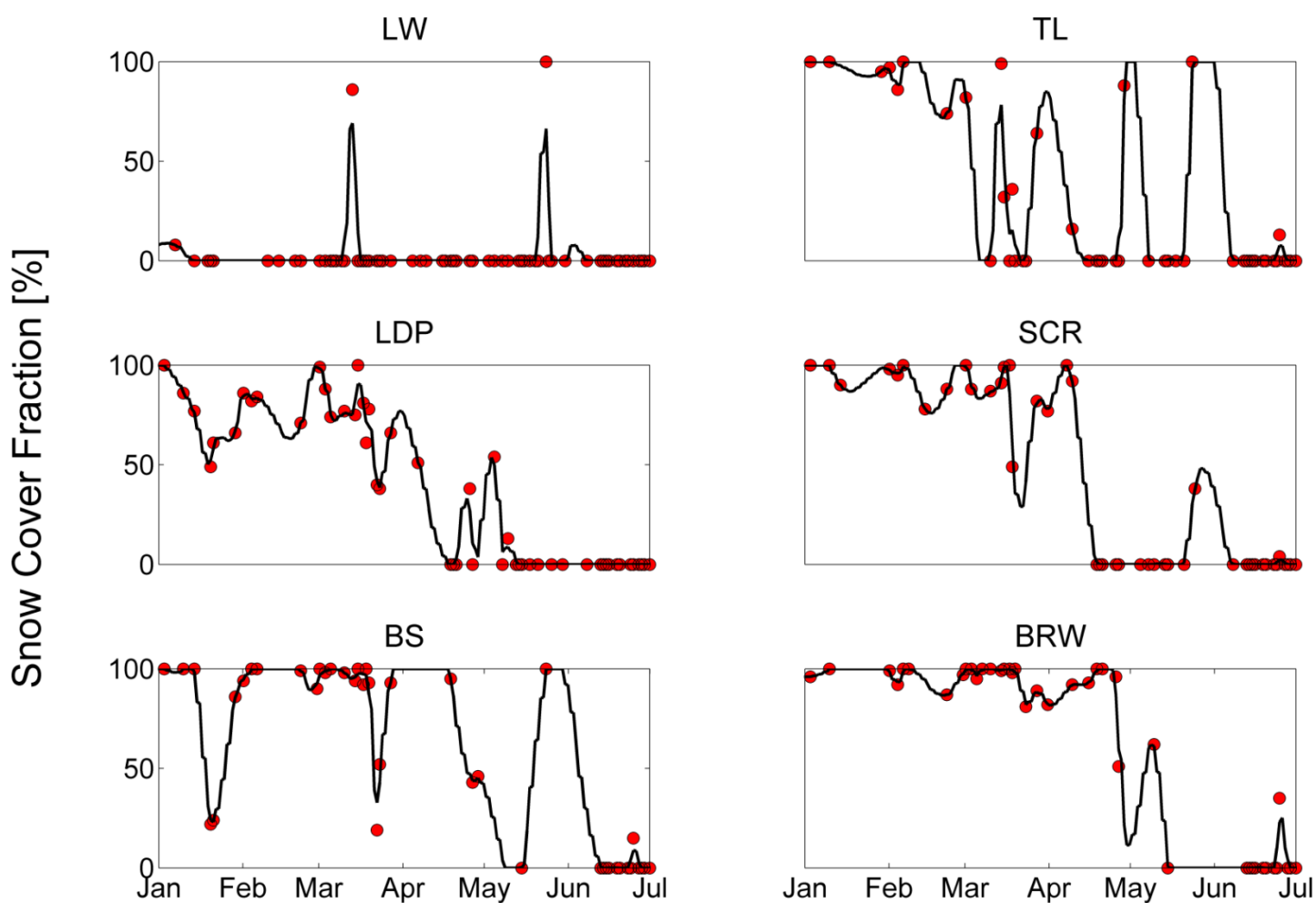
Figure 24. Observed fractional snow cover (red circles) and splines interpolation (black lines) for MOD10A1 pixels encompassing the meteorological stations in or near DCEW from 1 January 2010 to 30 June 2010.

symmetric. A standard deviation of 0.5 is used. This step serves to slightly sharpen the image, causing less contrast between pixel edges such that an increase or decrease in f_{SCA} occurs more gradually in space.

The smoothed data cube is then interpolated to a higher resolution using a nearest-neighbor approach identical to that described in Section 3.3.5. Cells are interpolated to the 10 m resolution of the DEM grid used as the overall downscaling mesh. After interpolation, the cube is cropped to the extent of the DEM. During the downscaling routine, the f_{SCA} data are subject to the algorithm described in Chapter 2.

3.4.2   Snow Albedo Assimilation

Data assimilation is the combination of complementary information from models and measurements into an optimized approximation to the true value of interest. Here, snow surface albedo is estimated through a simple assimilation approach, following the principles outlined by Reichle (2008). The decay parameter K_e from Eqn. 7 is varied within a range of values to produce random ensembles of possible albedo values at any time-step. After a new snowfall event, the range of these ensembles narrows. Conversely, after several days of no snow increase, the range increases, representing a growing uncertainty in the modeled albedo estimate. Since SNODAS only archives daily depth and SWE data, it is somewhat uncertain when a new snow event begins during a given 24-hour period. Thus, a small amount of random noise is added to the time-since-snow parameter t from Eqn. 7 to account for this uncertainty. The overall mean albedo model value is denoted m with uncertainty σ_m^2. MOD10A1 snow albedo estimates are treated as the observation to which the model is constrained and are denoted o with uncertainty σ_o^2.

A least-squares approximation between the model and observation is sought by way of an objective function J:

$$J = \frac{(x-m)^2}{\sigma_m^2} + \frac{(x-o)^2}{\sigma_o^2} \tag{9}$$

where x is the true state. We minimize the derivative of J with respect to x, yielding

$$\hat{x} = \frac{m \cdot \sigma_o^2 + o \cdot \sigma_m^2}{\sigma_o^2 + \sigma_m^2} \tag{10}$$

where $\hat{x}$ is the analysis estimate (Reichle, 2008). In this case, the analysis is an estimate of snow surface albedo at each time-step.

Difficulty exists in assigning an uncertainty to the MODIS albedo observations. Stroeve et al. (2006) found an overall RMSE for the Terra MOD10A1 product of 0.067. For simplicity, this study rounds this value up to 0.07 and assigns it to σ_o^2. The uncertainty range in the ensemble of albedo models is normalized such that its maximum value is equal to that of the MODIS observation (σ_o^2), allocating more trust in the model nearer to snowfall events and vice versa.

For each high-resolution downscaling pixel falling in a MODIS grid window, the analysis albedo estimate vector is assigned based on the time-series of MODIS observations and the decay function albedo derived from the overlapping SNODAS SWE pixel. As for snow-covered area observations, albedo estimates are similarly sporadic due to cloud-cover obstruction. Linear interpolation is executed between available observations, with uncertainties assigned to interpolants with magnitudes dependent upon their distance from the center of mass of the model ensemble range. The analysis will thus draw near to the observations and its interpolants, though less directly when the

observation-ensemble distance increases. Figure 25 illustrates this process for a singular

point in the grid.
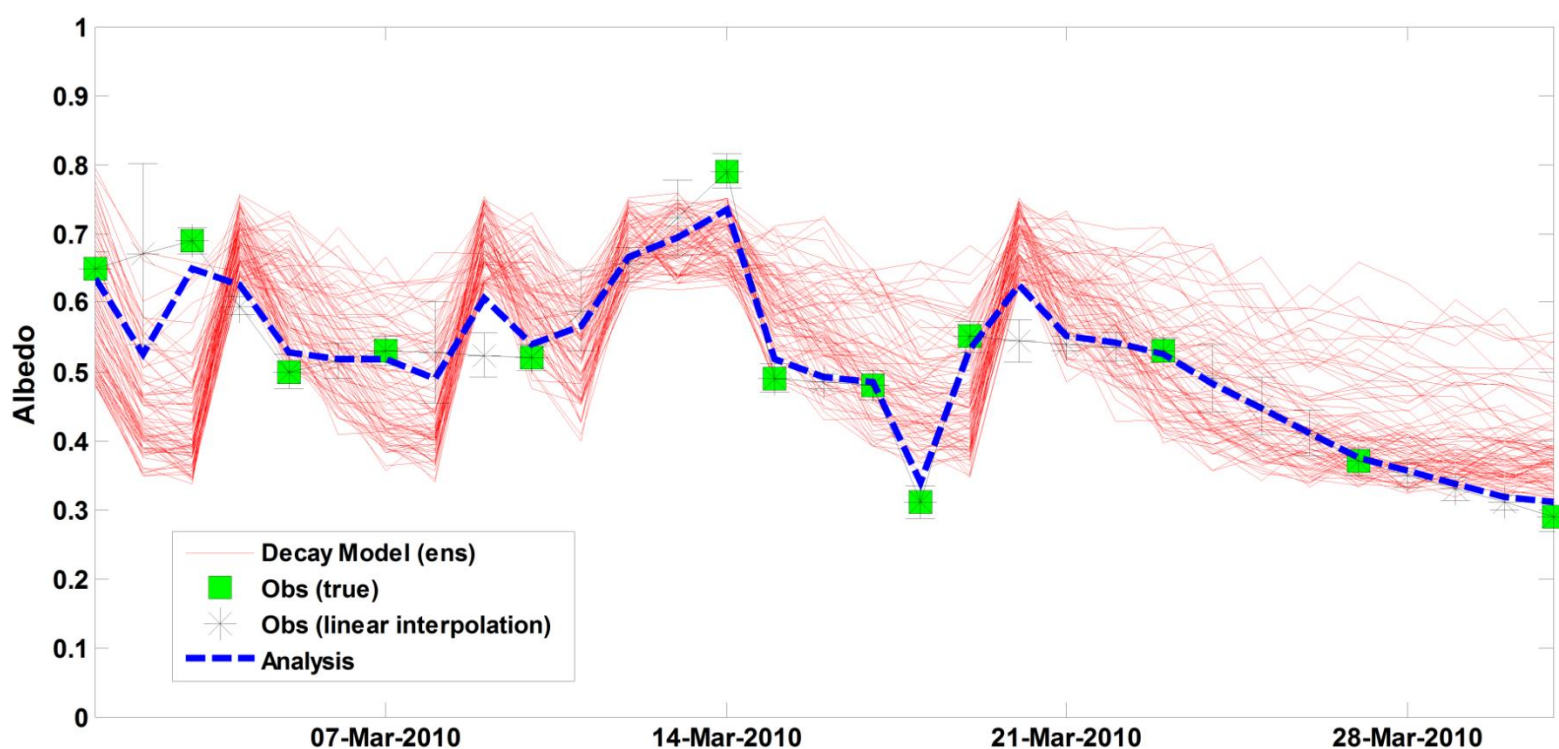
Figure 25. **Snow albedo time-series at an arbitrary point in the modeling domain. Decay models (red lines) are generated with SNODAS SWE information and a randomly-varying decay parameter. These are constrained to MOD10A1 albedo observations (green squares), generating analysis estimates (blue, dashed line) at each time-step.**

3.4.3   Spatial Downscaling Methodology

Spatial downscaling is executed on a pixel-by-pixel basis using the previously

described indices for solar radiation, vegetation, and snow surface albedo to disaggregate

the SNODAS predicted melt values to higher resolution. Without having to estimate

energy balances at the resolution of the downscaling grid, a melt factor coefficient can be approximated. This factor, which typically relates daily snowmelt to positive temperature (Celsius) values in a temperature-index approach, varies with physiographic and land cover properties (Anderson, 1973; Dingman, 2002). Without site-specific temperature observations, the melt factor, denoted M_F can be approximated by a unifying equation of the form (Eggleston et al., 1971):

$$M_F = k_m(1 - \alpha_A) \cdot k_v \cdot f_{sl} \tag{11}$$

in which k_m is a proportionality constant, α_A is snow surface albedo (Section 3.3.6), k_v is a vegetation transmission coefficient, and f_{sl} is insolation slope factor (Section 3.3.4). In this study, we substitute τ from Eqn. 2 (Section 3.3.5) for k_v to produce a temporally-varying degree of solar attenuation. The vegetation equation described by Eggleston et al. (1971) does not include the effect of solar zenith angle.

The constant k_m essentially becomes a tuning parameter, though Dingman (2002) published a value of 4.0. Adding ambiguity, other studies cite k_m equal to approximately 0.4 (Eggleston et al., 1971; Gray and Male, 1981). For the downscaling run performed in this study, a value of 4.0 is applied for k_m. However, this value can be adjusted after the downscaling run since, as a constant, it can be isolated from the general downscaling model equation (Eqn. 11). As such, within the window of each SNODAS melt estimate, coefficients $M_{F,i,j}$ are computed at the 10 m resolution of the DEM. These coefficients are computed via Eqn. 11 and multiplied by their nearest-neighbor, 30 arc-second SNODAS estimate to produce a downscaled estimate of snowmelt.

Fractional snow cover data are also used to update the downscaling process. The time-interpolated cube described in Section 3.4.1 is loaded during the routine and this product itself is downscaled before being applied. The MODIS f_{SCA} data are downscaled to binary estimates of snow cover at the 10 m mesh resolution. The process used here is identical to that described in Chapter 2. The binary snow cover information is used as a mask to effectively switch melt 'on' or 'off' based on the fractional observation and the expectation of the explicit locations of the binary snow-covered pixel occurrences. Care is taken to adjust the melt water quantity from SNODAS due to the restrictions imposed by snow cover updating. For instance, if the SNODAS-estimated melt within a 500 m MODIS grid window is X and the f_{SCA} value is Y, then the resulting melt within that window, Z, must be set to $Z = \frac{X}{Y}$ to conserve the mass in the original SNODAS estimate. This is because we are only assigning snow cover, and thus snowmelt, to f_{SCA}% of the pixels within each MODIS window.

3.4.4   Temporal Downscaling Methodology

In an effort to produce a temporally downscaled snowmelt estimate (i.e., from days to hours), a sinusoidal model for radiation is assumed. The solar radiation algorithm utilized (Swift, 1976) includes modifications (Ryan, 1977) to calculate times of sunrise (T_{sr}) and sunset (T_{ss}), in hour angles, for pixel surface based on local slope, aspect, latitude, and the solar declination angle (see Appendix A.1). From these, we assume a sinusoidal model to approximate hourly radiation given a daily integrated value. We assign a period component to a sine function in which

$$B = \frac{180}{T_{ss} - T_{sr}} \tag{12}$$

where B is the half-period of the function, generating positive values during the hour

angles from sunrise to sunset. Additionally, a phase shift is included as

$$C = -15 \cdot T_{sr} \cdot B \tag{13}$$

where C represents the shift in the sine function, forcing it to begin increasing at the

sunrise hour angle. We can then formulate a general model to obtain radiation as

$$R = A_R \cdot \int_{T_1}^{T_2} \sin(B \cdot t + C) dt \tag{14}$$

where T_1 and T_2 represent endpoints of an arbitrary time interval, A_R is the amplitude of

the function, and R is daily integrated solar radiation. Since the value of R is known prior

to the model formulation, we can normalize A_R to produce the proper sum of integration

for the entire daylight period. Substituting sunrise and sunset times as integration limits,

we arrive at

$$A_R = \frac{R}{\int_{T_{sr}}^{T_{ss}} \sin(B \cdot t + C) dt} \tag{15}$$

by which we find the amplitude that drives the modeled sum to equal the daily integrated

radiation value predicted by the solar algorithm.

The same approach is used in temporal melt downscaling. Since the downscaling

model predicts a daily melt depth and the insolation algorithm computes sunrise hour

angle and sunset hour angle for every pixel, we can formulate a model for hourly-

resolution snowmelt estimates:

$$M_h = A_M \cdot \int_{T_1}^{T_2} \sin(B \cdot t + C) dt \tag{16}$$

in which M_h represents the melt during the time between integration limits and A_M is normalized in the same fashion as described for Eqn. 15. This function assumes that maximum melt rate coincides with maximum insolation. Although there is likely a lag time associated, this study neglects this issue for simplicity.

3.5   Results

As described, the downscaling model is employed with 2010 daily snowmelt runoff data from SNODAS. Applying Eqns. 11 and 16 with a value of 4.0 for k_m, the model produces 10 m output with a 24-hour, sinusoidally-varying estimate at each pixel for each day. Results from the model are selected at the four specific pixel locations containing the field lysimeter sites (Table 6). To reiterate a point from Section 3.3.7, the lysimeters from TL lie within a single SNODAS pixel, as do the lysimeters at LDP. This fact has the benefit of displaying the spatial disaggregation of a single melt estimate (SNODAS) into distinct, sub-grid approximations (downscaling model). For example, without downscaling, both of the model pixels containing the TL S and TL N lysimeters locations would receive the same SNODAS melt value. The same is true for the LDP locations. This allows for simple comparison between the downscaled and observed data and does not complicate the parameterization of the constant k_m.

As depicted by Figure 26, the TL S lysimeter began to observe marked snowmelt on 3 February 2010. Conflictingly, the model (SNODAS and thus downscaled) does not begin to melt snow until 22 February 2010. It is confirmed that this temporal inconsistency is not due to any artifact of the downscaling algorithm. The snow albedo estimates are within a reasonable range of values, generally between 0.50 and 0.75, forest canopy is zero (no attenuation) and the snow cover remains relatively high ($f_{SCA} > 0.75$)

throughout this time period. Rather, the disagreement is due to the SNODAS model estimate itself. LDP observations and downscaling model estimates display similar discrepancies, though not as extreme. The downscaling model, as is, does not provide a means for allocating melt outside of the 24-hour period during which SNODAS limits it. That is, the downscaling estimates are temporally at the mercy of the SNODAS estimates.
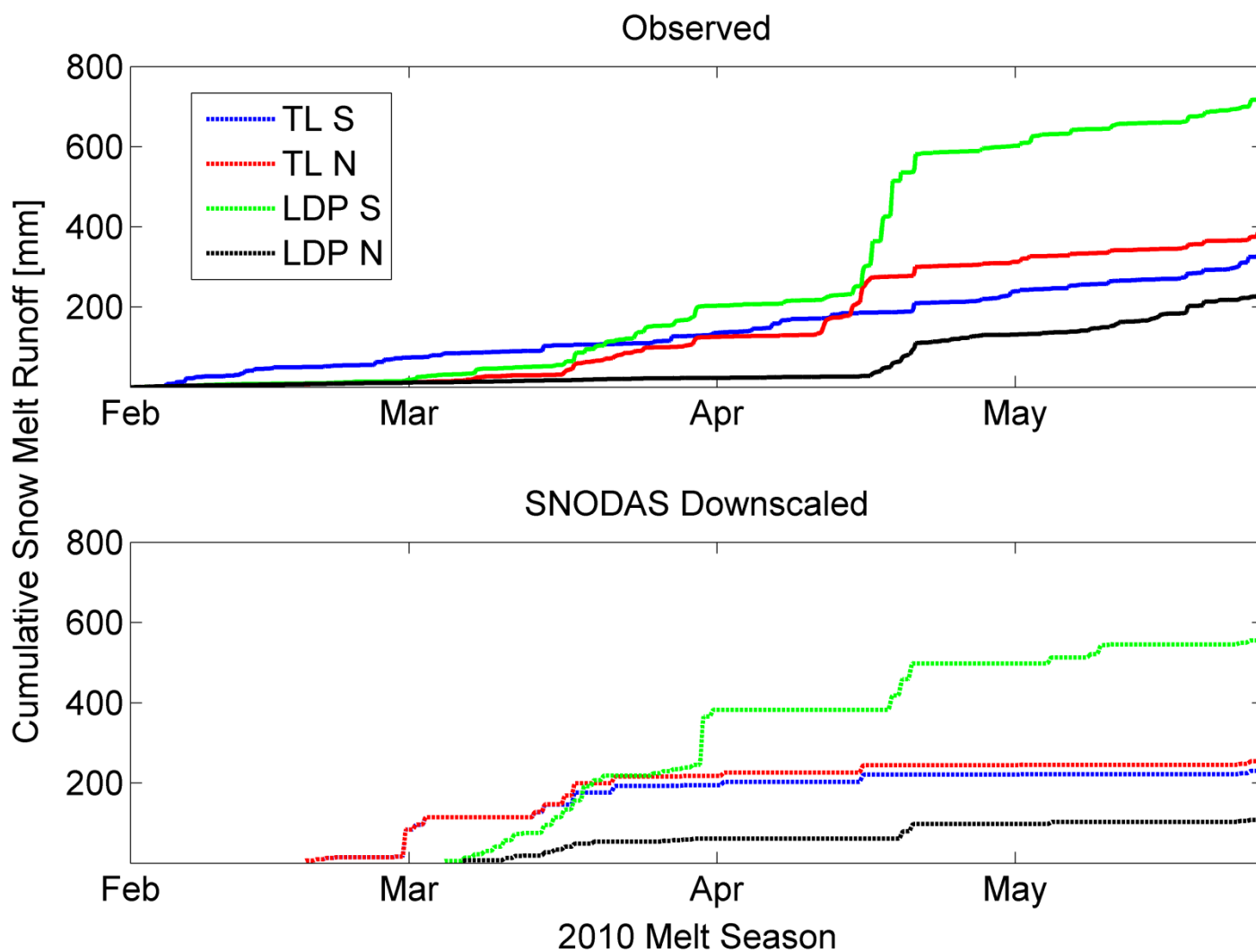
Figure 26. **Cumulative snowmelt measured at field lysimeters (top) and estimated by downscaling SNODAS melt (bottom) for 4 locations in DCEW.**

While temporal divergences exist, seasonal cumulative values display a more agreeable pattern. Not only does the downscaling model disaggregate the SNODAS melt estimates in the same direction as the observations, but the relative differences between the lysimeter pair locations are of similar magnitudes. Table 7 shows a consistent under-prediction of melt, the magnitude of under-prediction is relatively stable across the sites. This suggests that these data may allow for calibration of the downscaling parameter k_m. The bar graphs in Figure 27 depict moderate agreement between the model and observations when k_m is adjusted to a value of 6.49. This value is computed simply as the product of the initial k_m value (0.4) and the mean of the relative under-prediction values for the 4 lysimeter sites (row 3 in Table 7).
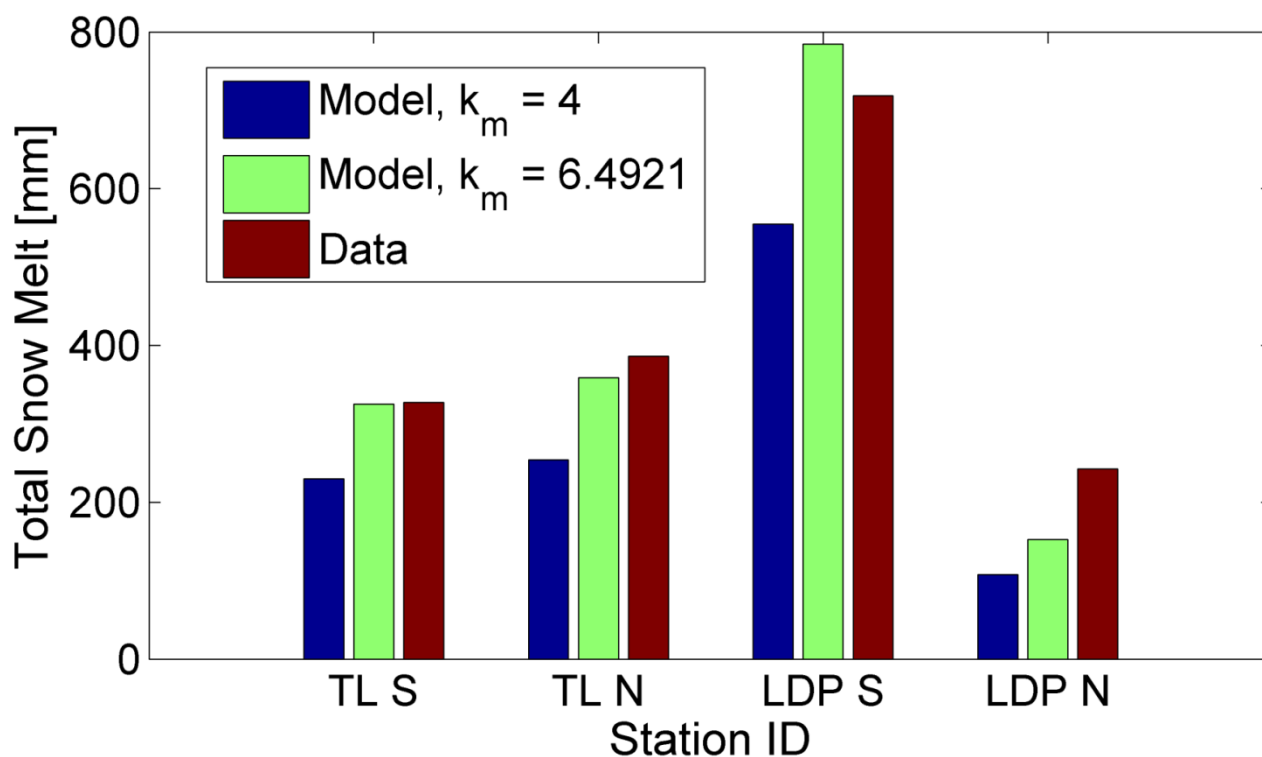
Figure 27. **2010 total observed snowmelt (red bars) compared to total melt predicted by the SNODAS downscaling model with parameter k_m equal to the standard 4.0 (blue bars) and the 'calibrated' 6.4921 (green bars).**

Table 7. **Total snowmelt (mm) measured at four field lysimeter locations with downscaled (D/S) model results. Obs/Mod fraction depict the overall magnitude offsets. Treeline (TL S & TL N) and Lower Deer Point (LDP S & LDP N) locations each fall within the boundary of a single, respective SNODAS grid cell.**

Total Melt (mm)	TL S	TL N	LDP S	LDP N
Observed	327.29	386.41	718.58	242.58
Model (D/S)	229.91	253.87	555.07	107.72
Obs / Mod	1.42	1.52	1.29	2.25

3.6   Discussion and Conclusion

Described above is a study using SNODAS snowmelt output and attempting to estimate the spatiotemporal variability within the model's grid cells. This variability is estimated through a semi-empirical approach, utilizing satellite remote sensing fractional snow-covered area (f_{SCA}) data, solar radiation indices, vegetation canopy attenuation adjustments, and snow surface albedo parameters.

The described method is applied to the DCEW domain, allowing for direct comparison with existing field lysimeter stations. Results depict temporal discrepancies and an under-prediction of total melt water output in comparison with observed data. The latter result is consistent with studies finding that SNODAS tends to underestimate SWE. For instance, this outcome was found in DCEW (Anderson, 2011) when SWE was compared to field snow-course data. Similarly, in the Sierra Nevada, SNODAS underestimated SWE when compared to a presumably more accurate energy balance reconstruction model (Dozier, 2011). Moreover, the downscaling routine is not capable of resolving temporal disaggregation outside of the described constraints, limiting the use of such a tool with a coarse-scale snowmelt model. As such, SNODAS may not be appropriate for estimating snowmelt at the resolution sought in this study. However, since

SNODAS data in this study are from 2010, they are downscaled from the RUC 2 NWP model. Given that SNODAS is now using RAP NWP model predictions, future comparisons between SNODAS estimates (raw or downscaled) and field observations may provide, at the least, some insight into the effect of this recent change to the model structure.

CHAPTER FOUR: PROJECT CONCLUSIONS

Described in this work are downscaling algorithms used to predict spatial variability within existing snow data systems. Downscaled data containing information about this variability may prove useful in hydrologic modeling applications. For instance, streamflow timing can be greatly affected by spatially heterogeneous distributions of snow (Lundquist and Dettinger, 2005). Furthermore, accounting for sub-grid physiographic variables (e.g., insolation as in this study) may have vast implications for modeling under the effects of climate change on snowmelt and subsequent runoff (Lundquist and Flint, 2006). These algorithms are designed to operate with high computational efficiency and require little parameterization. The datasets used are readily-available, operational ones available to all users, with the implication that similar work could be repeated following the details of this document.

In Chapter 2, a method is outlined for downscaling 500 m fractional SCA from MODIS. An algorithm is used by which the MODIS snow fraction informs a computationally efficient linear model to generate binary snow cover estimates of increased spatial resolution. The model is calibrated to 30 m Landsat observations for a semi-arid, mid-latitude region in southwestern Idaho using indices that are presumed to strongly influence the spatial distribution of snow cover. The model is tested against data not used in calibration and shown to perform favorably in some areas while failing in others. Difficulties exist in identifying specific reasons for failure, though it is suspected

that, in many areas, wind re-distribution and forest canopy play a crucial role in snow cover. Since they are not included, it is suggested that the addition of canopy and wind parameters would possibly be a way forward.

In Chapter 3, variability within SNODAS melt pixels is estimated through a semi-empirical approach, utilizing satellite remote sensing fractional snow-covered area (f_{SCA}) data with the algorithm from Chapter 2, solar radiation indices, vegetation canopy attenuation adjustments, and snow surface albedo parameters. By downscaling the modeled melt to a higher resolution, other basin states and fluxes could potentially be estimated with increased predictive skill. Here SNODAS is observed to differ widely in its timing in comparison with observation. This study suggests that a more complex downscaling routine would be required to accurately model snowmelt processes at the hillslope scale. Understanding the response of a catchment to spatially variable snowmelt is an important concept.

REFERENCES

Aguado, E., Cayan, D., Riddle, L., & Roos, M. (1992). Climatic Fluctuations and the Timing of West Coast Streamflow. *Journal of Climate*, *5*(12), 1468–1483.

Anderson, B. T. (2011). *Spatial Distribution and Evolution of a Seasonal Snowpack in Complex Terrain: An Evaluation of the SNODAS Modeling Product* (Master's thesis). Boise State University, Boise, ID.

Anderson, E. A. (1973). *National weather service river forecast system/snow accumulation and ablation model*. NOAA Technical Memorandum NWS HYDRO-17, US Department of Commerce, Silver Spring, MD.

Anderton, S. P., White, S. M., & Alvera, B. (2004). Evaluation of spatial variability in snow water equivalent for a high mountain catchment. *Hydrological Processes*, *18*(3), 435–453. doi:10.1002/hyp.1319.

Armstrong, R. L., & Brun, E. (Eds.). (2008). *Snow and Climate: Physical Processes, Surface Energy Exchange and Modeling*. New York: Cambridge University Press.

Bales, R. C., Molotch, N. P., Painter, T. H., Dettinger, M. D., Rice, R., & Dozier, J. (2006). Mountain hydrology of the western United States. *Water Resources Research*, *42*(8), W03537. doi:10.1029/2005WR004387.

Bales, R. C., Hopmans, J. W., O'Geen, A. T., Meadows, M., Hartsough, P. C., Kirchner, P., Hunsaker, C. T., et al. (2011). Soil Moisture Response to Snowmelt and Rainfall in a Sierra Nevada Mixed-Conifer Forest. *Vadose Zone Journal*, *10*, 786–799. doi:10.2136/vzj2011.0001.

Barnett, T. P., Adam, J. C., & Lettenmaier, D. P. (2005). Potential impacts of a warming climate on water availability in snow-dominated regions. *Nature*, *438*, 303–309. doi:10.1038/nature04141.

Barnett, T. P., Pierce, D. W., Hidalgo, H. G., Bonfils, C., Santer, B. D., Das, T., Bala, G., et al. (2008). Human-induced changes in the hydrology of the western United States. *Science*, *319*(5866), 1080–1083. doi:10.1126/science.1152538.

Barrett, A. (2003). *National Operation Hydrologic Remote Sensing Center SNOw Data Assimilation System (SNODAS) Products at NSIDC*. NSIDC Special Report 11. Boulder, CO, USA: National Snow and Ice Data Center. Digital Media.

Bertsekas, D. P., Nedić, A., & Ozdaglar, A. E. (2003). *Convex Analysis and Optimization*. Belmont, MA: Athena Scientific.

Blöschl, G. (1999). Scaling issues in snow hydrology. *Hydrological Processes, 13*, 2149–2175.

Carroll, T., Cline, D., Fall, G., Nilsson, A., Li, L., & Rost, A. (2001). NOHRSC Operations and the Simulation of Snow Cover Properties for the Conterminous U.S. Proceedings of the *69th Annual Meeting of the Western Snow Conference*, 1–14.

Cayan, D. R., Kammerdiener, S. A., Dettinger, M. D., Caprio, J. M., & Peterson, D. H. (2001). Changes in the Onset of Spring in the Western United States. *Bulletin of the American Meteorological Society*, *82*(3), 399–415.

Chen, F., Warner, T. T., & Manning, K. (2001). Sensitivity of Orographic Moist Convection to Landscape Variability: A Study of the Buffalo Creek, Colorado, Flash Flood Case of 1996. *Journal of the Atmospheric Sciences*, *58*, 3204–3223.

Clark, M. P., Slater, A. G., Barrett, A. P., Hay, L. E., McCabe, G. J., Rajagopalan, B., & Leavesley, G. H. (2005). Assimilation of snow covered area information into hydrologic and land-surface models. *Advances in Water Resources*, *29*(8), 1209–1221. doi:10.1016/j.advwatres.2005.10.001.

Clark, M. P., Hendrikx, J., Slater, A. G., Kavetski, D., Anderson, B., Cullen, N. J., Kerr, T., et al. (2011). Representing spatial variability of snow water equivalent in hydrologic and land-surface models: A review. *Water Resources Research*, *47*(7). doi:10.1029/2011WR010745.

Cline, D., Bales, R., & Dozier, J. (1998). Estimating the spatial distribution of snow in mountain basins using remote sensing and energy balance modeling. *Water Resources Research*, *34*(5), 1275–1285.

Debele, B., Srinivasan, R., & Gosain, a. K. (2009). Comparison of Process-Based and Temperature-Index Snowmelt Modeling in SWAT. *Water Resources Management*, *24*(6), 1065–1088. doi:10.1007/s11269-009-9486-2.

de Boor, C. (2007). *Spline Toolbox 3: user's guide*. Natick, MA: The MathWorks.

Dingman, S. L. (2002). *Physical Hydrology*. Upper Saddle River, NJ: Prentice Hall.

Dozier, J., & Marks, D. (1987). Snow Mapping and Classification from Landsat Thematic Mapper Data. *Annals of Glaciology, 9*, 97–103.

Dozier, J. (1989). Spectral Signature of Alpine Snow Cover from the Landsat Thematic Mapper. *Remote Sensing of Environment*, *28*, 9–22.

Dozier, J., & Frew, J. (2009). Computational provenance in hydrologic science : a snow mapping example Computational provenance in hydrologic science : a snow mapping example. *Philosophical Transactions of the Royal Society A*, *367*, 1021–1033. doi:10.1098/rsta.2008.0187.

Dozier, J. (2011). Mountain hydrology, snow color, and the fourth paradigm. *Eos, Transactions, American Geophysical Union*, *92*(43), 373. doi:10.1029/2011EO430001.

Durand, M., Molotch, N. P., & Margulis, S. A. (2008). Merging complementary remote sensing datasets in the context of snow water equivalent reconstruction. *Remote Sensing of Environment*, *112*(3), 1212–1225. doi:10.1016/j.rse.2007.08.010.

Eggleston, K. O., Israelsen, E. K., & Riley, J. P. (1971). *Hybrid computer simulation of the accumulation and melt processes in a snowpack*. Technical Report PRWG65-1. Utah State University, Logan, UT.

Eiriksson, D. P. (2012). *The Hydrologic Significance of Lateral Water Flow Through Snow* (Master's thesis). Boise State University, Boise, ID.

Eiriksson, D., Whitson, M., Luce, C. H., Marshall, H. P., Bradford, J., Black, T., Hetrick, H., & McNamara, J. P. (2013). An evaluation of the hydrologic relevance of lateral flow in snow at hillslope and catchment scales. *Hydrological Processes*. doi:10.1002/hyp.9666.

Elder, K., Dozier, J., & Michaelsen, J. (1991). Snow Accumulation and Distribution in an Alpine Watershed. *Water Resources Research*, *27*(7), 1541–1552. doi:10.1029/91WR00506.

Elder, K., Rosenthal, W., & Davis, R. E. (1998). Estimating the spatial distribution of snow water equivalence in a montane watershed. *Hydrological Processes*, *12*(10-11), 1793–1808.

Ellis, C. R., & Pomeroy, J. W. (2007). Estimating sub-canopy shortwave irradiance to melting snow on forested slopes, *Hydrological* Processes, *21*(19), 2581–2593. doi:10.1002/hyp.6794.

Flerchinger, G. N., Marks, D., Reba, M. L., Yu, Q., & Seyfried, M. S. (2010). Surface fluxes and water balance of spatially varying vegetation within a small mountainous headwater catchment. *Hydrology and Earth System Sciences*, *14*(6), 965–978. doi:10.5194/hess-14-965-2010.

Gleick, P. H. (1987). The development and testing of a water balance model for climate impact assessment: Modeling the Sacramento Basin. *Water Resources Research*, *23*(6), 1049–1061. doi:10.1029/WR023i006p01049.

Graham, C. B., Barnard, H. R., Kavanagh, K. L., & Mcnamara, J. P. (2012). Catchment scale controls the temporal connection of transpiration and diel fluctuations in streamflow. *Hydrological Processes*. doi:10.1002/hyp.9334.

Gray, D. M. & Male, D. H. (1981). *Handbook of Snow*. Elmsford, NY: Pergamon Press.

Gribb, M. M., Forkutsa, I., Hansen, A. Chandler, D. G., & McNamara, J. P. (2009). The Effect of Various Soil Hydraulic Property Estimates on Soil Moisture Simulations. *Vadose Zone Journal, 8*(2), 321–331.

Hall, D. K., Riggs, G. A., & Salomonson, V. V. (1995). Development of Methods for Mapping Global Snow Cover Using Moderate Resolution Imaging Spectroradiometer Data. *Remote Sensing of Environment*, *54*, 127–140.

Hall, D.K., Riggs, G.A., & Salomonson, V.V. (2006). *MODIS/Terra Snow Cover Daily L3 Global 500m Grid, Version 5*. 2006-2011. Boulder, Colorado USA: National Snow and Ice Data Center.

Hock, R. (2003). Temperature index melt modelling in mountain areas. *Journal of Hydrology*, *282*, 104–115. doi:10.1016/S0022-1694(03)00257-9.

Homan, J. W., Luce, C. H., McNamara, J. P., & Glenn, N. F. (2011). Improvement of distributed snowmelt energy balance modeling with MODIS-based NDSI-derived fractional snow-covered area data. *Hydrological Processes*, *25*(4), 650–660. doi:10.1002/hyp.7857.

Homer, C., Dewitz, J., Fry, J., Coan, M., Hossain, N., Larson, C., Herold, N., McKerrow, A., VanDriel, J.N., & Wickham, J. (2007). Completion of the 2001 National Land Cover Database for the Conterminous United States. *Photogrammetric Engineering and Remote Sensing*, *73*(4), 337–341.

Johnson, G. L., & Hanson, C. L. (1995). Topographic and Atmospheric Influences on Precipitation Variability over a Mountainous Watershed. *Journal of Applied Meteorology*, *34*(1), 68–87.

Justice, C. O., Vermote, E., Townshend, J. R. G., Defries, R., Roy, D. P., Hall, D. K., Salomonson, V. V., Privette, J. L., Riggs, G., Strahler, A., Lucht, W., Myneni, R. B., Knyazikhin, Y., Running, S. W., Nemani, R. R., Wan, Z. M., Huete, A. R., van Leeuwen, W., Wolfe, R. E., Giglio, L., Muller, J. P., Lewis, P., & Barnsley, M. J. (1998). The Moderate Resolution Imaging Spectroradiometer (MODIS): Land remote sensing for global change research. *IEEE Transactions on Geoscience and Remote Sensing*, *36*(4), 1228–1249. doi:10.1109/36.701075.

Kirnbauer, R., Blöschl, G., & Gutknecht, D. (1994). Entering the Era of Distributed Snow Models. *Nordic Hydrology*, *25*(1-2), 1–24.

Kelleners, T. J., Chandler, D. G., McNamara, J. P., Gribb, M. M., & Seyfried, M. S. (2010). Modeling Runoff Generation in a Small Snow-Dominated Mountainous Catchment. *Vadose Zone Journal*, *9*(3), 517–527. doi:10.2136/vzj2009.0033.

Kunkel, M. L., Flores, A. N., Smith, T. J., McNamara, J. P., & Benner, S. G. (2011). A simplified approach for estimating soil carbon and nitrogen stocks in semi-arid complex terrain. *Geoderma*, *165*(1), 1–11. doi:10.1016/j.geoderma.2011.06.011.

Lee, R. (1962). Theory of the "Equivalent Slope". *Monthly Weather Review*, *90*, 165–166.

Lehning, M., Ingo, V., Gustafsson, D., Nguyen, T. A., St, M., & Zappa, M. (2006). ALPINE3D : a detailed model of mountain surface processes and its application to snow hydrology. *Hydrological Processes*, *20*(10), 2111–2128. doi:10.1002/hyp.6204.

Luce, C. H., Tarboton, D. G., & Cooley, K. R. (1998). The influence of the spatial distribution of snow on basin-averaged snowmelt. *Hydrological Processes*, *12*(10-11), 1671–1683.

Luce, C. H., Tarboton, D. G., & Cooley, K. R. (1999). Subgrid parameterization of snow distribution for an energy and mass balance snow cover model. *Hydrological Processes, 13*(12-13), 1921–1933.

Li, D., Durand, M., & Margulis, S. A. (2012). Potential for hydrologic characterization of deep mountain snowpack via passive microwave remote sensing in the Kern River basin, Sierra Nevada, USA. *Remote Sensing of Environment*, *125*, 34–48. doi:10.1016/j.rse.2012.06.027.

Lundquist, J. D., & Dettinger, M. D. (2005). How snowpack heterogeneity affects diurnal streamflow timing. *Water Resources Research*, *41*(5), W05007. doi:10.1029/2004WR003649.

Lundquist, J. D., & Flint, A. L. (2006). Onset of Snowmelt and Streamflow in 2004 in the Western United States: How Shading May Affect Spring Streamflow Timing in a Warmer World. *Journal of Hydrometeorology*, *7*, 1199–1217.

Mahat, V., & Tarboton, D. G. (2012). Canopy radiation transmission for an energy balance snowmelt model. *Water Resources Research*, *48*(1), W01534. doi:10.1029/2011WR010438.

Marks, D., Domingo, J., Susong, D., Link, T., & Garen, D. (1999). A spatially distributed energy balance snowmelt model for application in mountain basins. *Hydrological Processes*, *13*(12-13), 1935–1959.

Marks, D., Link, T., Winstral, A., & Garen, D. (2001). Simulating snowmelt processes during rain-on-snow over a semi-arid mountain basin. *Annals of Glaciology*, *32*, 195–202.

Martinec, J. & Rango, A. (1981). Areal Distribution of Snow Water Equivalent Evaluated by Snow Cover Monitoring. *Water Resources Research*, *17*(5), 1480-1488. doi:10.1002/hyp.7206.

McNamara, J. P., Chandler, D., Seyfried, M., & Achet, S. (2005). Soil moisture states, lateral flow, and streamflow generation in a semi-arid, snowmelt-driven catchment. *Hydrological Processes*, *19*(20), 4023–4038. doi:10.1002/hyp.5869.

Michalakes, J., Dudhia, J., Gill, D., Klemp, J., & Skamarock, W. (1998). Design of a next-generation regional weather research and forecast model. In Zwieflhofer, W. & Kreitz, N. (Eds.), *Towards Teracomputing* (117–124). World Scientific: River Edge, NJ.

Milly, P. C. D., Betancourt, J., Falkenmark, M., Hirsch, R. M., Zbigniew, W., Lettenmaier, D. P., & Stouffer, R. J. (2008). Stationarity Is Dead : Whither Water Management? *Science*, *319*, 573–574. Doi:10.1126/science.1151915.

Molotch, N. P., & Bales, R. C. (2005). Scaling snow observations from the point to the grid element: Implications for observation network design. *Water Resources Research*, *41*, W11421, doi:10.1029/2005WR004229.

Molotch, N. P. (2009). Reconstructing snow water equivalent in the Rio Grande headwaters using remotely sensed snow cover data and a spatially distributed snowmelt model. *Hydrological Processes*, *23*(7), 1076– 1089. doi:10.1002/hyp.7206.

National Operational Hydrologic Remote Sensing Center (NORHSC). (2012). NOAA's Source for Snow Information. Retrieved from http:// http://www.nohrsc.nws.gov.

Nolin, A. W., Dozier, J., & Mertes, L. A. K. (1993). Mapping alpine snow using a spectral mixture modeling technique. *Annals of Glaciology*, *17*, 121–124.

Painter, T. H., Dozier, J., Roberts, D. a., Davis, R. E., & Green, R. O. (2003). Retrieval of subpixel snow-covered area and grain size from imaging spectrometer data. *Remote Sensing of Environment*, *85*(1), 64–77. doi:10.1016/S0034-4257(02)00187-6.

Painter, T. H., Rittger, K., McKenzie, C., Slaughter, P., Davis, R. E., & Dozier, J. (2009). Retrieval of subpixel snow covered area, grain size, and albedo from MODIS. *Remote Sensing of Environment*, *113*(4), 868–879. doi:10.1016/j.rse.2009.01.001.

Palmer, P. L. (1988). The SCS Snow Survey Water Supply Forecasting Program: Current Operations and Future Directions. *Western Snow Conference*, Kalispell, MT, 19-21 April, 1988.

Pavelsky, T. M., Sobolowski, S., Kapnick, S. B., & Barnes, J. B. (2012). Changes in orographic precipitation patterns caused by a shift from snow to rain. *Geophysical Research Letters*, *39*(18), L18706. doi:10.1029/2012GL052741.

Powers, D. M. W. (2011). Evaluation: From Precision, Recall and F-Measure to ROC, Informedness, Markedness & Correlation. *Journal of Machine Learning Technologies*, *2*(1), 37–63.

Raleigh, M. S., Rittger, K., Moore, C. E., Henn, B., Lutz, J. A., & Lundquist, J. D. (2013). Ground-based testing of MODIS fractional snow cover in subalpine meadows and forests of the Sierra Nevada. *Remote Sensing of Environment*, *128*, 44–57. doi:10.1016/j.rse.2012.09.016.

Reba, M. L., Marks, D., Seyfried, M., Winstral, A., Kumar, M., & Flerchinger, G. (2011). A long-term data set for hydrologic modeling in a snow-dominated mountain catchment. *Water Resources Research*, *47*(7), W07702. doi:10.1029/2010WR010030.

Reichle, R. H. (2008). Data assimilation methods in the Earth sciences. *Advances in Water Resources*, *31*(11), 1411–1418. doi:10.1016/j.advwatres.2008.01.001.

Rew, R., Davis, G., Emmerson, S., Davies, H., Hartnett, E., & Heimbigner, D. (2011). *The NetCDF Users Guide: Data Model, Programming Interfaces, and Format for Self-Describing, Portable Data*. Unidata Program Center, University Corporation for Atmospheric Research.

Rittger, K., Painter, T. H., & Dozier, J. (2012). Assessment of methods for mapping snow cover from MODIS. *Advances in Water Resources, 51*, 367-380. doi:10.1016/j.advwatres.2012.03.002.

Rodell, M., & Houser, P. R. (2004). Updating a land surface model with MODIS-derived snow cover. *Journal of Hydrometeorology*, *5*(6), 1064–1075.

Rosenthal, W., & Dozier, J. (1996). Automated mapping of montane snow cover at subpixel resolution from the Landsat Thematic Mapper. *Water Resources Research*, *32*(1), 115–130.

Ryan, B. C. (1977). *Computation of times of sunrise, sunset, and twilight in or near mountainous terrain*. Research Note PSW-RN-322. Berkeley, CA: U.S.Department of Agriculture, Forest Service, Pacific Southwest Forest and Range Experiment Station.

Salomonson, V. V., & Appel, I. (2004). Estimating fractional snow cover from MODIS using the normalized difference snow index. *Remote Sensing of Environment*, *89*, 351–360. doi:10.1016/j.rse.2003.10.016.

Salomonson, V. V., & Appel, I. (2006). Development of the Aqua MODIS NDSI fractional snow cover algorithm and validation results. *IEEE Transactions on Geoscience and Remote Sensing*, *44*(7), 1747–1756. doi:10.1109/TGRS.2006.876029.

Schimel, D., Kittel, T. G. F., Running, S., Monson, R., Turnipseed, A., & Anderson, D. (2002). Carbon sequestration studied in western U.S. mountains. *Eos, Transactions, American Geophysical Union*, *83*(40), 445–449. doi:10.1029/2002EO000314.

Schölzel, C., & Friederichs, P. (2008). Nonlinear Processes in Geophysics Multivariate non-normally distributed random variables in climate research − introduction to the copula approach. *Nonlinear Processes in Geophysics*, *15*, 761–772.

Schwarzlander, H. (2011). *Probability Concepts and Theory for Engineers*. Chichester, West Sussex, UK: John Wiley & Sons, Ltd.

Smith, T. J., McNamara, J. P., Flores, a. N., Gribb, M. M., Aishlin, P. S., & Benner, S. G. (2011). Small soil storage capacity limits benefit of winter snowpack to upland vegetation. *Hydrological Processes*, *25*(25), 3858–3865. doi:10.1002/hyp.8340.

Stewart, I. T., Cayan, D. R., & Dettinger, M. D. (2004). Changes in Snowmelt Runoff Timing in Western North America Under a 'Business as Usual' Climate Change Scenario. *Climatic Change*, *62*, 217–232.

Stieglitz, M., Shaman, J., Mcnamara, J., Engel, V., Shanley, J., & Kling, G. W. (2003). An approach to understanding hydrologic connectivity on the hillslope and the implications for nutrient transport. *Global Biogeochemical Cycles*, *17*(4), 1105. doi:10.1029/2003GB002041.

Storck, P., Lettenmaier, D. P., & Bolton, S. M. (2002). Measurement of snow interception and canopy effects on snow accumulation and melt in a mountainous maritime climate, Oregon, United States. *Water Resources Research*, *38*(11), 1223. doi:10.1029/2002WR001281.

Stroeve, J. C., Box, J. E., & Haran, T. (2006). Evaluation of the MODIS (MOD10A1) daily snow albedo product over the Greenland ice sheet. *Remote Sensing of Environment*, *105*(2), 155–171. doi:10.1016/j.rse.2006.06.009.

Sturm, M., & Wagner, A. M. (2010). Using repeated patterns in snow distribution modeling: An Arctic example. *Water Resources Research*, *46*(12), W12549. doi:10.1029/2010WR009434.

Swift, L. (1976). Algorithm for Solar Radiation on Mountain Slopes. *Water Resources Research*, *12*(1), 108–112.

Tarboton, D. G., & Luce, C. H. (1996). *Utah Energy Balance Snow Accumulation and Melt Model (UEB) Computer model technical description and users guide*. Utah Water Research Laboratory and USDA Forest Service Intermountain Research Station.

Thirel, G., Salamon, P., Burek, P., & Kalas, M. (2011). Assimilation of MODIS snow cover area data in a distributed hydrological model. *Hydrology and Earth System Sciences Discussions*, *8*(1), 1329–1364. doi:10.5194/hessd-8-1329-2011.

Tucker, C.J. (1979). Red and photographic infrared linear combinations for monitoring vegetation. *Remote Sensing of Environment, 8*, 721–726.

Tyler, S. W., Burak, S. A., McNamara, J. P., Lamontagne, A., Selker, J. S., & Dozier, J. (2008). Spatially distributed temperatures at the base of two mountain snowpacks measured with fiber-optic sensors. *Journal of Glaciology*, *54*(187), 673–679.

Watershed Sciences, Inc. (2009). *LiDAR Remote Sensing Data Collection: Reynolds Creek & Dry Creek, Idaho.* Submitted 27 April, 2009. Portland, OR: Watershed Sciences.

Winstral, A., Elder, K., & Davis, R. E. (2002). Spatial Snow Modeling of Wind-Redistributed Snow Using Terrain-Based Parameters. *Journal of Hydrometeorology*, *3*, 524–538.

Winstral, A., & Marks, D. (2002). Simulating wind fields and snow redistribution using terrain-based parameters to model snow accumulation and melt over a semi-arid mountain catchment. *Hydrological Processes, 16*(18), 3585–3603. doi:10.1002/hyp.1238.

Wiscombe, W. J., & Warren, S. G. (1981). A Model for the Spectral Albedo of Snow. I: Pure Snow. *Journal of the Atmospheric Sciences*, *37*(12), 2712–2733.

Wolfe, R. E., Nishihama, M., Fleig, A. J., Kuyper, J. A., Roy, D. P., Storey, J. C., & Patt, F. S. (2002). Achieving sub-pixel geolocation accuracy in support of MODIS land science. *Remote Sensing of Environment*, *83*(1-2), 31–49. doi:10.1016/S0034-4257(02)00085-8.

APPENDICES

A.1   Solar Radiation Computations

In calculating insolation at the pixel scale, it is first necessary to solve for the independent variables in Eqn. 1 of this section. Some of these variables are calculated using empirical parameterizations while others are based on trigonometric identities. A sloping (or horizontal) pixel's insolation, R_{slope}, is computed as an adjustment to the solar constant:

$$R_{slope} = R_1 \cdot \left\{ \begin{array}{l} \sin(D_s) \cdot \sin(L_1) \cdot \frac{T_{ss} - T_{sr}}{15} + \cos(D_s) \cdot \\ \cos(L_1) \cdot \left[\sin(T_{ss} + \Delta T) - \sin(T_{sr} + \Delta T) \cdot \frac{12}{\pi} \right] \end{array} \right\} \tag{1}$$

where the independent variables are as follows: R_1 is the extraterrestrial solar constant aggregated over the course of an hour and adjusted for E, the eccentricity of the Earth-Sun radius vector (Eqn. 3), D_s is solar declination angle, L_1 is latitude of equivalent slope (Lee, 1962), T_{ss} and T_{sr} are hour angle of sunset and sunrise on the local slope, respectively, and ΔT is the hour angle time offset between the local slope and L_1.

The solar constant, denoted R_0, is approximately between 1.95 and 2.0 cal/cm^2/min (Langley/min) and its one-hour aggregate value, R_1, is found as

$$R_1 = \frac{R_0}{E^2} \cdot 60 \tag{2}$$

where E is the earth-sun radius vector in astronomical units, calculated as a function of Julian date:

$$E = 1.0 - 0.0167 \cdot \cos[(J - 3) \cdot 0.0172] \tag{3}$$

where the Julian expression $J = 1$ corresponds to January 1st of a given year. The Langley (cal/cm^2) is easily converted to a more typical flux unit (W/m^2) by multiplying by 11.622, leaving a time unit (hours) in the numerator. Since the given solar constant is multiplied by 60 minutes, the hour term cancels, leaving W/m^2 as the energy flux term. This conversion is not actually made in the solar algorithm since the desired slope factor ratio output is unitless, rendering the insolation units superfluous.

The latitude of equivalent slope theory (Lee, 1962) stems from the concept that every sloping plane on a sphere is parallel to some horizontal surface elsewhere on the body. It is computed as:

$$L_1 = \sin^{-1}(\cos(k) \cdot \sin(\theta) + \sin(k) \cdot \cos(\theta) \cdot \cos(\alpha)) \tag{4}$$

where α is aspect, k is slope inclination and θ is latitude. All variables are respective to the pixel in question and the units are in degrees. The time offset between actual and equivalent slopes is calculated as:

$$\Delta T = \tan^{-1}\left(\frac{\sin(\alpha) \cdot \sin(k)}{\cos(k) \cdot \cos(\theta) - \sin(k) \cdot \sin(\theta) \cdot \cos(\alpha)}\right) \tag{5}$$

where variables and units are as described for Eqn. 4 and the offset is measured as a degree hour angle. Sunrise (sunset) hour angles are computed according to:

$$T = \cos^{-1}[-\tan(\theta) \cdot \tan(D_s)]. \tag{6}$$

Solar declination angle D_s is found via a simple empirical function of Julian day:

$$D_s = \frac{180}{\pi} \sin^{-1}\left\{0.39785 \cdot \sin\left[\begin{array}{c}278.9709 + 0.9856 \cdot J + 1.9163 \cdot \\ \sin(356.6153 + 0.9856 \cdot J)\end{array}\right]\right\}. \tag{7}$$

Finally, R_{horiz} is computed per Eqn. 2 substituting $k = 0°$ to find insolation at a horizontal plane. The slope factor is then computed as the ratio of potential insolation on a sloping pixel surface to that of a horizontal one. That is

$$f_{sl} = \frac{R_{slope}}{R_{horiz}}. \tag{8}$$

A.2   MODIS Reprojection Script

In order to reproject a sinusoidal MOD10A1 file into a user-friendly projection, the MODIS Reprojection Tool (MRT) is useful. The MRT is a freely available tool from the LP-DAAC. In this case, it is invoked from the system command line using the call to the function 'resample' and an ancillary call to a parameter file that controls the output projection coordinate system any spectral or spatial subsetting. Here, MATLAB's command line makes iterative calls to the MRT, outputting new, reprojected and cropped files. The input files are arranged and named with the format 'JX.hdf' where 'X' represents the day of year. The batch-processed output files are re-named 'JX_R.hdf' to identify unique, reprojected MOD10A1 HDF files. Shown below is the MATLAB script used along with the parameter file containing the subsetting and output projection information. Flags are used in the resample function to alter the input and output file names that are called. These flags appear intuitively as $-i$ and $-o$ in the script.

MATLAB Batch Reprojection Script

```
num_files = 181;              % number of files in the directory
for i = 1:num_files
    system_str = ['resample -p 10a1.prm -i...
    H:\MODIS\10a1\J',int2str(i),'.hdf -o...
    H:\MODIS\10a1\reproj\J',int2str(i),'_R.hdf'];
    system(system_str);
end
```

MRT Parameter File (10a1.prm)

```
INPUT_FILENAME = H:\MODIS\10a1\J1.hdf

SPECTRAL_SUBSET = ( 1 1 1 )

SPATIAL_SUBSET_TYPE = OUTPUT_PROJ_COORDS

SPATIAL_SUBSET_UL_CORNER = ( 564000.0 4848000.0 )
SPATIAL_SUBSET_LR_CORNER = ( 580000.0 4830000.0 )

OUTPUT_FILENAME = H:\MODIS\10a1\reproj\J1r.hdf

RESAMPLING_TYPE = NEAREST_NEIGHBOR

OUTPUT_PROJECTION_TYPE = UTM

OUTPUT_PROJECTION_PARAMETERS = (
 0.0 0.0 0.0
 0.0 0.0 0.0
 0.0 0.0 0.0
 0.0 0.0 0.0
 0.0 0.0 0.0 )

DATUM = WGS84

UTM_ZONE = 11

OUTPUT_PIXEL_SIZE = 500
```